Formation and Surface Chemistry of Bi$_2$Se$_3$ Nanoplatelets

T.C. Wigmans

Master Thesis

Debye Institute for Nanomaterials Science, Utrecht University

March 20, 2022

Universiteit Utrecht

Abstract

Topological Insulators (TIs) are a broad family of crystalline materials that have gained increased attention in recent years due to their unique electronic properties: Coherent electron states emerge at the surfaces or edges of the crystal due to spin-orbit driven band inversion. These coherent spin-momentum locked states carry charge and spin without dissipation and are thus of direct interest for energy-efficient conventional and quantum computing. Bi_2Se_3 & Bi_2Te_3 serve as a model system for strong TIs in two or three dimensions due to their relatively simple band structure and helical Dirac states in a broad inverted gap. Their surface/edge states would be interesting to study with STM in a constrained 2D environment. We therefore colloidally obtained Bi_2Se_3 & Bi_2Te_3 nanoplatelets (NPLs) of varying dimensions (lateral: 50-1000 nm, vertical: 4-20 nm) using a modified polyol hot injection synthesis. Their atomic structure was determined by HRHAADF-STEM, EDX, ED, AFM, XRD and UV-VIS showing (nearly) flat stoichiometric hexagonal crystals with a well-defined number of quintuple layers. NPLs were then treated with a ligand exchange/removal procedure to reduce the organic capping layer inherently present on the surface which led to an improved STM characterizability that allows us to observe their topological features in future research.

Keywords: Topological insulators, 2D nanomaterials, nanoplatelets, colloidal synthesis, bismuth chalcogenides

Contents

Glossary

NP = Nanoparticle

NPL = Nanoplatelet

QC = Quantum Confinement

TSS = Topological Surface State

QL = Quintuple Layer

VdW = Van der Waals

LT = Ligand Treatment

EDX = Energy-dispersive X-ray Diffraction

ED = Electron Diffraction

TEM = Transmission Electron Microscopy

STEM = Scanning Transmission Electron Microscopy

HAADF = High Angle Annular Dark Field

XRD = X-ray Diffraction

FTIR = Fourier-transform Infrared Spectroscopy

NMR = Nuclear Magnetic Resonance

AFM = Atomic Force Microscopy

STM = Scanning Tunneling Microscopy

Chapter 1.

Introduction

A problem that our society faces today is the ever-increasing demand for faster computing power, as the size of metal-oxide-semiconductor field-effect transistors (MOSFETs) that determine computational power are reaching fundamental limits, where quantum effects start to play a significant role. Therefore, the industry is searching for alternative ways to increase the processing capacities of computers. On such effort is the development of so-called quantum computing, which uses the inherent quantum characteristics of materials to do its calculations [21]. A big contender in this progressive field of research are topological insulators.
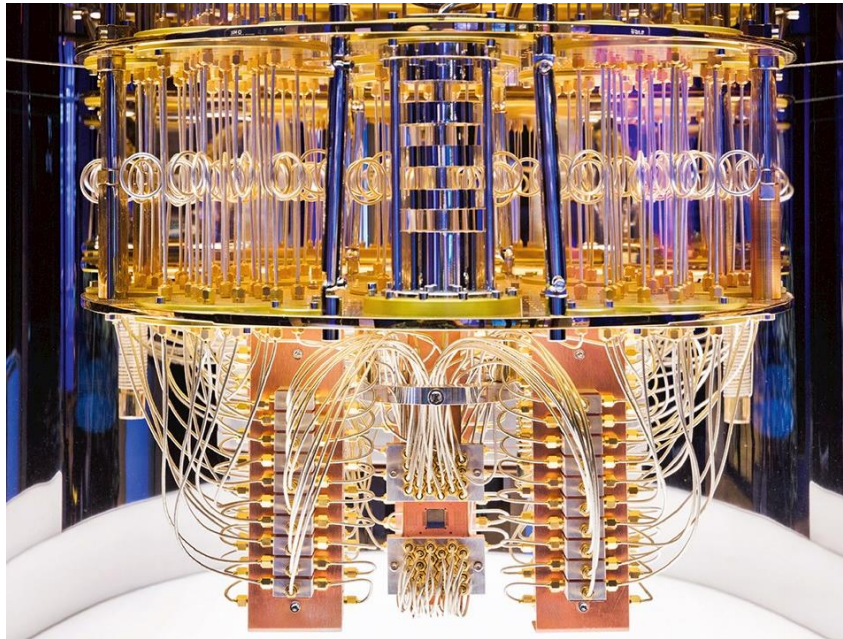
Figure 1.1: Image of the IBM quantum computer. [89]

Topological Insulators (TIs) are a broad family of crystalline materials that have gained increased attention in recent years due to their unique electronic properties, as they exhibit conductive electron states at the surface or edge of the material. These states have been shown to efficiently carry charge and spin without scattering and are thus very interesting for and quantum computing and spintronic applications [90]. Within the class of TIs, Bismuth chalcogenide materials are one of the first discovered and extensively studied TI systems [92]. Therefore, they act as a model system for many new developments in the field and have already been synthesized in a wide variety of nanoscale morphologies including Quantum Dots [91], Nanowires [92], Nanoplatelets (NPLs) [55]. Scanning Tunnelling Microscopy (STM) is a popular method to investigate the special conductive properties of TIs as it can probe the local conductivity of surfaces, although it is usually limited to materials manufactured by surface deposition techniques which limits the morphologies that can be obtained.

Figure 1.2*: Preliminary results of a Bi$_2$Se$_3$ NPL image measured by STM [93]*

Recently, Bhunia *et al.* (2017) have demonstrated that it is possible to effectively measure the topological features of colloidally synthesized Bi$_2$Se$_3$ NPLs using ST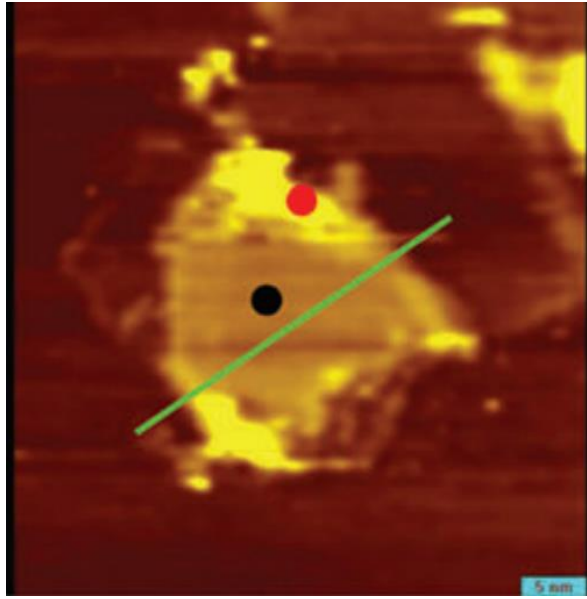M [93], which allows for the simultaneous study of both topological surface and edge states. However, some of the NPLs display severe morphological inhomogeneities as well as instabilities in the STM tip (see Figure 1.2) which limits the topographic and conductive resolution that can be obtained and the conclusions that can be derived from the measurements. Therefore, a more detailed investigation of these surface and edge states using STM is valuable. This work aims to improve the characterizability of Bi$_2$Se$_3$ NPLs in STM based studies and paving the way for similar materials such as Bi$_2$Te$_3$ to be investigated as well. This is achieved by systematically varying reaction parameters of the synthesis to obtain NPLs more suitable for STM characterization with a focus on decreasing the overall level of aggregation and increasing the quantity of free NPLs, as this necessary for proper SPM measurement. In addition the organic contamination on the NPLs in the form of surfactants is extensive investigated, as it is a likely culprit for the unsatisfactory tip stability.

The structure of this thesis is as follows. Chapter 2 will provide the theoretical background required to understand the remainder of this work. The experimental methods used to synthesize and characterize the NPLs will be presented in Chapter 3. Chapter 4 will outline and discuss the results of the performed syntheses and measurements mentioned in Chapter 3. Finally, Chapter 5 will summarize the major discoveries made in this thesis.

Chapter 2.

Theory

This chapter will discuss the concepts necessary to interpret the results presented later in this thesis. The first section will introduce the concept of nanomaterials, topological insulators and their relevant material properties. The second section will then dive into the conditions needed to induce nanomaterial growth and how the surface chemistry affects these conditions as well as the properties of the obtained nanostructures. Finally, the third section will outline the known (topological)properties, synthesis procedures and characterization methods of Bi_2Se_3 and Bi_2Te_3 NPLs.

2.1 Nano-states of matter

Matter is usually classified in the form of gasses, liquids and solids. The latter can further be divided into metals, semiconductors and insulators, which are distinguished by their bandgaps (E_g) between the valence band (VB) and the conduction band (CB). Metals do not have an intrinsic band gap, representing a continual availability of energy states, while insulators and semiconductors do have a bandgap (<4 eV for semiconductors and > 4 eV for insulators). However, there are states of matter that cannot be fully categorized by this classification, as they appear to contain properties characteristic of more than one material. One such material is called a topological insulator (TI).
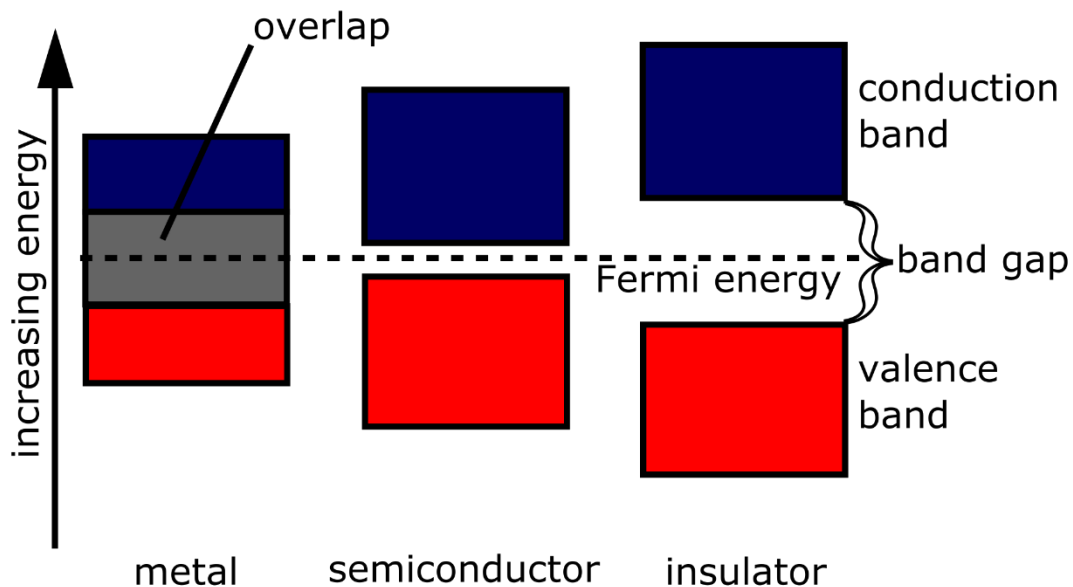
Figure 2.0: Schematic of the band structure of metals, semiconductors and insulators.[17]

2.1.1 Topological insulators

The study of topology is concerned with the classification of geometric objects by properties which are preserved under continuous deformation. These properties are called topological invariants. A classic example is the transition from a mug into a donut (shown in Figure 2.1), as these both only have 1 hole and are therefore topologically equivalent. In this example the number of holes is the topological invariant that is used to distinguish between objects, as they cannot be created or destroyed by smooth deformations such as stretching, twisting or bending.

Figure 2.1: Schematic representation of the smooth deformation from a mug to a donut (torus) [18]

This concept of topology can be a useful tool when investigating materials with an inverted band structure. Band inversion is a situation in which the usual ordering of the p and s character of the VB and CB is reversed and opens up a band gap as shown in Figure 2.2. This mechanism is usually driven by a strong spin-orbit coupling (SOC) although scalar relativistic effects and lattice distortions may also play a significant role [4]. While an inverted band structure does not directly prove the existence of a non-trivial TI state, all experimentally verified TIs thus far did exhibit an inverted orbital band.
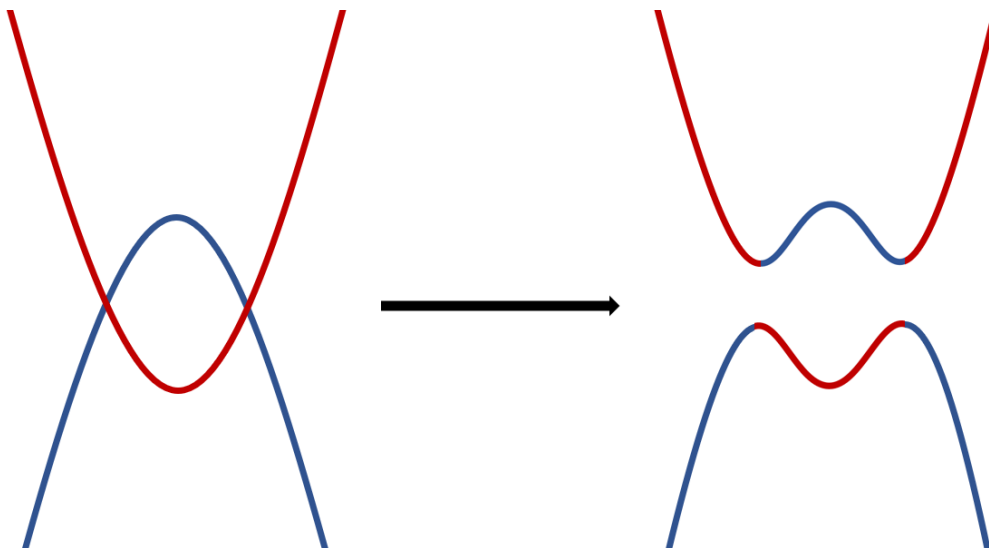
Figure 2.2: Schematical representation of spin-orbit coupled band inversion

The problem occurs when considering the surface of such a material which, under typical conditions, is at the interface with another insulator without inverted band structure such as air or a vacuum. At this interface the system needs to transition continuously between the 2 insulators as shown in Figure 2.3. However, due to the inverted nature of the bands this is only possible by closing the bandgap as shown in the image below. This characteristic of the band structure acts as a topological invariant comparable to the hole mentioned earlier and thus the insulators are seen as topologically distinct. As the bandgap disappears, localized conductive states at the TI surface are formed around the Fermi energy level. This means a TI possesses both an insulating bulk state as a metallic-like surface state, which is the main reason for its unique electronic properties.

Figure 2.3: *Schematic representation of the continuous transformation from a trivial to a topological insulator [20]*

The fact that these topological surface states (TSS) originate from a topological invariant (Z_2) makes them unusually robust as they are protected by time-reversal symmetry (TRS). Due to the large SOC, which also induced the inverted band structure, the spins on the surface are polarized in reciprocal space. However, the net spin moment still averages to zero, which can be realized by electrons with opposing spins traveling in opposite directions a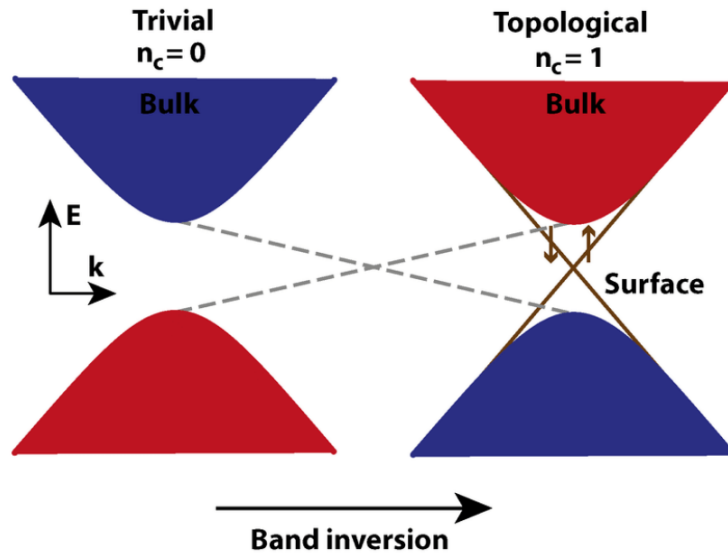t the surface. Therefore, to alter the movement vector of an electron a simultaneous flipping of its spin is required. The TSS are therefore insensitive to spin-independent scattering of the electrons and their conductivity is preserved even in high-disorder conditions [5]. An exception to this rule is the introduction of a magnetic field or magnetic impurity to the material as magnetic effects can successfully break the TRS of the TSS [6], however this does not necessarily mean the surface conduction is fully removed [81].

An important distinction within TIs is the difference between a 3D (Strong) and 2D (Weak) TI, which can be distinguished by the Z_2 topological invariant as a weak TI only contains a single Z_2 invariant, while a strong TI contains four [82]. A 3D TI has the TSS over its whole surface while a 2D TI (also called a Quantum Spin Hall (QSH) phase) only exhibits them along its edges. The exact nature of these states, as well as the conditions needed to transfer from 3D TI to a 2D TI in the 2D limit are currently still under investigation but hybridization between the opposing surface states seems to be an important factor [7].

2.1.2 Towards the nanoscale

Nanomaterials, as their name suggests, are a class of materials with one or more characteristic lengths within the nanoscale regime. The boundary of what constitutes as a nanomaterial can be somewhat vague but generally it contains two properties. It must have at least one length scale around 1-100 nm and one property must be significantly different in comparison to the bulk material [1].

This definition allows for a wide range of nanomaterial shapes, which are usually classified by their dimensionality (ranging from 0 to 3D). A schematic representation is shown in Figure 2.4. Zero-dimensionality (0D) nanomaterials only have length scales smaller than 100 nm. This is the category of a classic nanoparticle. 1D materials have one spatial direction which is significantly greater than

its other two and thus usually form wires or tube type geometries. As expected, 2D materials then contain two more sizable lateral dimensions in comparison to its smaller thickness and therefore take the shape of either thin films or NPLs. Finally, 3D materials contain no dimensions within the nanoscale regime and are therefore considered either bulk material or some form of nano-assembly consisting of various nanocrystals.
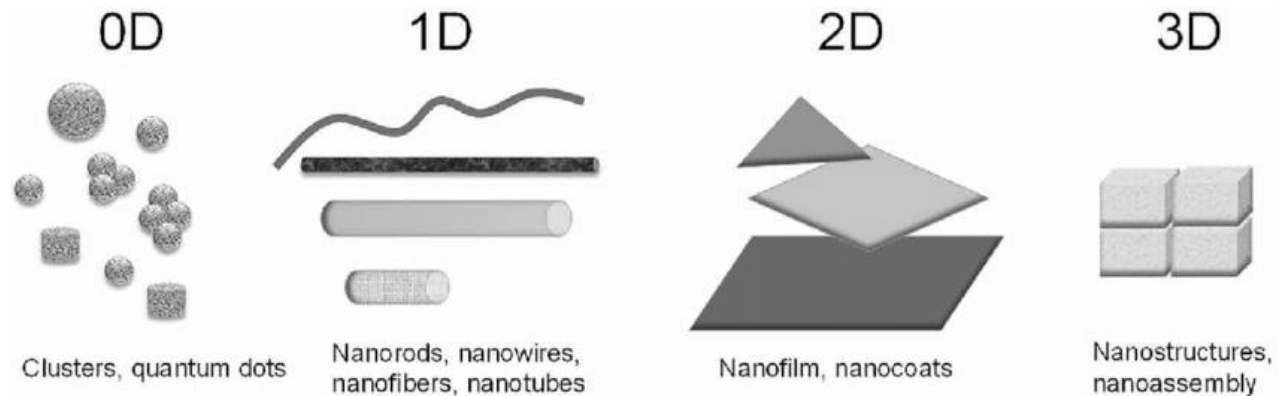

Figure 2.4: Schematic representation of the possible morphologies of nanostructures [22]

The aforementioned change in properties in contrast with the bulk is what makes nanomaterials such an appealing concept, as these physical and chemical attributes are size-dependent. This means that the properties be tuned by tailoring the size and shape of a material without altering the chemical composition which can lead to a multitude of new applications for known substances.

This size dependence originates from 2 principal effects when transitioning from bulk to nanoscale. Firstly, the ratio of surface area to volume increases exponentially which leads to surface atoms and the effects of surfactants playing a bigger role in the characteristics of the nanocrystals. Secondly, spatial confinement effects which originate from the quantum mechanical identity of matter start to take effect as the crystal-size reaches a critical length scale. The specific length scale varies with the material and property under consideration.

2.2 Nanomaterial Growth mechanisms

Several methods have already been investigated to obtain Bi_2Se_3 or Bi_2Te_3 nanostructures with atomically controlled thickness such as Molecular Beam Epitaxy (MBE) [58-60], Physical Vapor Deposition (PVD) [61] and Micromechanical exfoliation [62] shown in Figure 2.5. These techniques can control the thickness and environment of the deposited QLs on an atomic scale and are easily combined with high resolution surface microscopy techniques to obtain detailed structural and electronic properties [63]. However, these approaches all employ dry deposition or exfoliation methods and are therefore subject to several limitations including high costs, low yields and low scalability which make the eventual realization of large-scale production more challenging. These problems could be circumvented by switching to a solution synthesis approach which uses less costly equipment, is easily upscaled and allows for a high level of control over dimensionality, geometry and composition of the 2D nanostructures [64]. The colloidal nature of the synthesis would also open up the possibility for substrate-free characterization techniques while still allowing for surface microscopy by employing drop casting procedures.
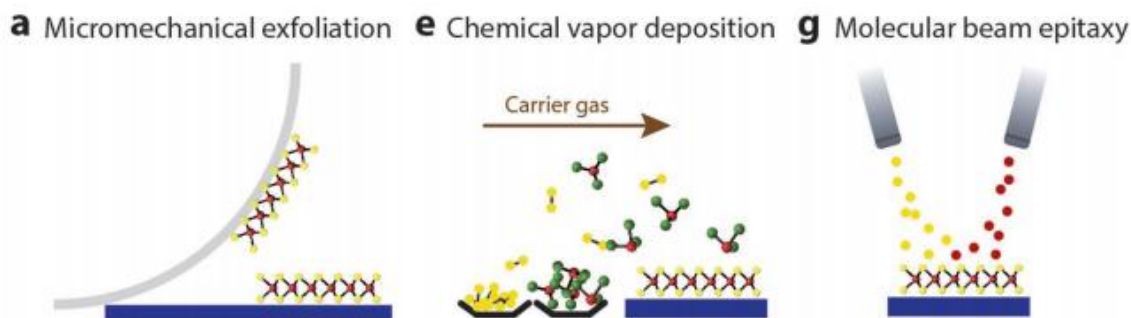
Figure 2.5: Overview of regularly used dry deposition and exfoliation methods [63].

2.2.1 Colloidal growth

The synthesis of colloidal NPs has seen considerable attention in the last few decades for its ability to produce high-quality nanostructures using straightforward synthesis procedures [1]. However, the underlying mechanisms that drive these reactions are still not fully understood and several models have been developed throughout the years which try to rationalize the process, but none seem to be generally applicable to all systems [65,66]. This is partly due to the broad range of tuneable parameters present in a typical reaction procedure including but not limited to: reaction/precursor temperature (over time), concentration, reactivity, stability and rate/method of addition of precursors and solvent/surfactant composition. The nucleation and growth kinetics have been shown to be strongly dependent on any of these variables and good control over them is therefore necessary for reproducible results [1]. This however, resembles a double-edged sword as the high amount of variation also allows for the wide range of obtainable nanostructures for which colloidal growth methods are known for.

Figure 2.6: Graphic illustration of the colloidal growth process [1]

Although the specifics around colloidal NP growth are a topic of discussion, four steps distributed over three main stages (shown in Figure 2.6) can still be recognized. The stages are called: 1. Induction. 2. Nucleation and 3. Growth. The first stage includes the transition of the building block element from a precursor complex to monomers in a sol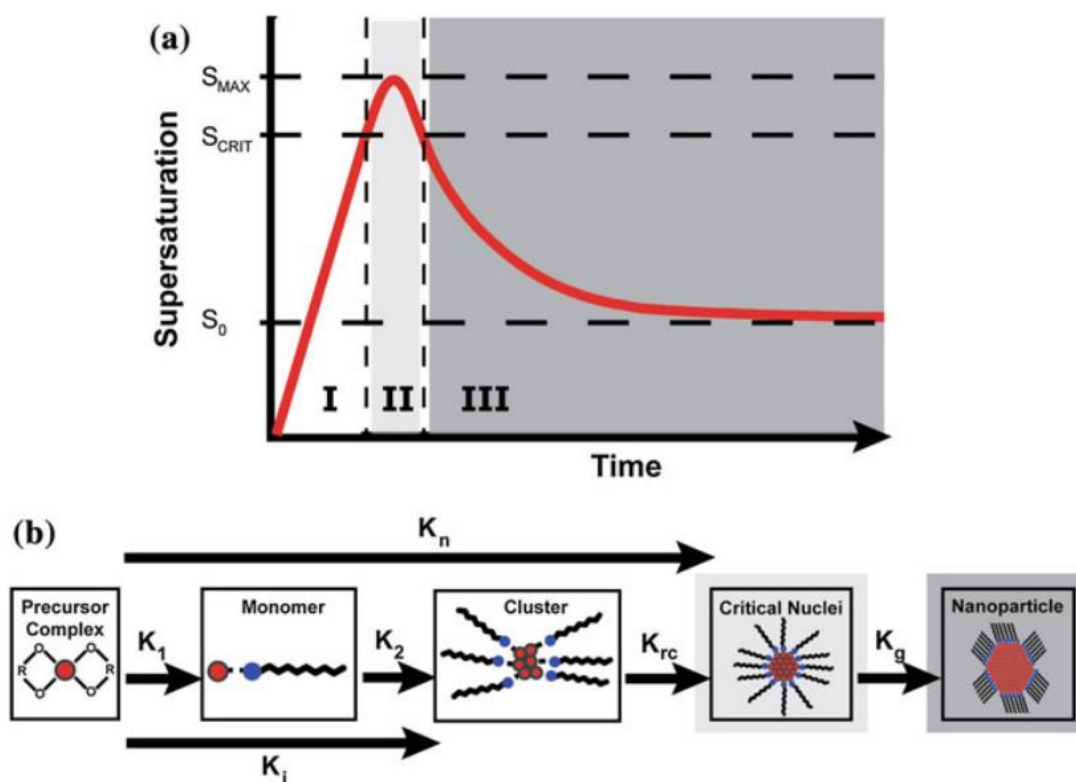ution that eventually come together as clusters. These monomers are stabilized by ligand molecules which will be discussed in a later chapter. The driving force behind this clustering is supersaturation, which describes the atoms as a metastable state where the concentration of a species exceeds its equilibrium solubility. This leads to a negative chemical potential difference which causes the atoms to spontaneously aggregate and form clusters. However, the addition of atoms on the surface also leads to an increase in the Gibbs energy due to the surface atoms having unsaturated bonds, which means the initially formed clusters are still unstable.

$$S = \frac{a}{a_{sat}} \geq 1$$

$$\Delta G_V = N\Delta\mu = -NkT\ln(S)$$

$$\Delta G_A = \gamma A = \gamma\beta N^{2/3}$$

Once the clusters reach a certain critical size the nucleation stage is reached, as shown in Figure 2.7. This is characterized by the ability of the clusters to exhibit irreversible growth, either by monomer addition or epitaxial coalescence of clusters. This critical size is dependent on the colloid system but can be defined as the point where the Gibbs free energy gained from the removal of atoms from a supersaturated solution outweighs the energy lost by the increase in total surface area of the colloid. A short nucleation window leads to a narrower size distribution as most nucleation events happen simultaneously and therefore have similar growth conditions. This can be realized by a sudden increase in monomer concentration or decrease in monomer solubility. However, it is important that monomers are still available in the later growth stage so a kinetic balance is between nucleation and growth is necessary.
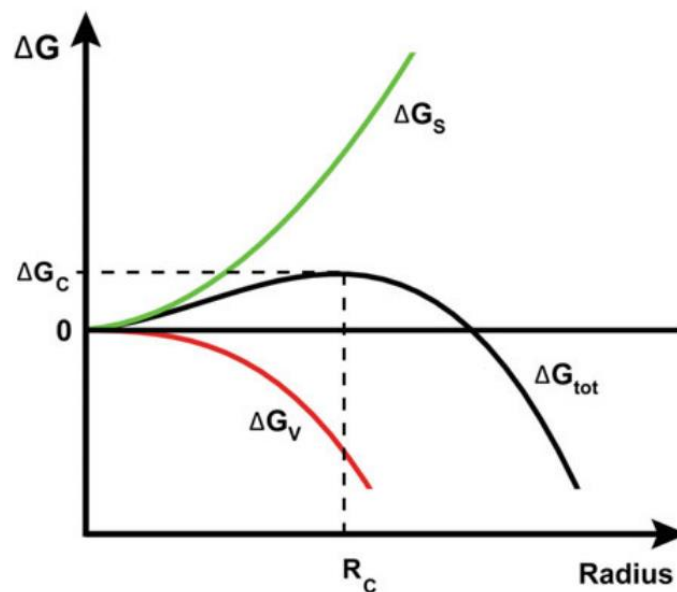
$$r_c = -\frac{2\gamma}{\rho kTln(S)}$$

Figure 2.7: *Graphic representation of the evolution of free energy at varying cluster radii.*

Once nucleation decreases the supersaturation below the threshold needed to form critically sized clusters, the growth stage is reached in which the previously formed nuclei grow into fully formed NPs until the monomer concentration reaches thermodynamic equilibrium. However, the growth stage is usually terminated by cooling the reaction solution before reaching equilibrium to limit the size and prevent a large size distribution of the NPs caused by processes such as Oswald ripening. To control the size and shape of the NPs several parameters such as nucleation rate and monomer concentration, reactivity and solubility need to be carefully considered. These can be tuned in several ways by varying the precursor complex and its concentration, reaction temperature, the reaction solvent composition and the type of surfactant.

This model does not provide the reason for the existence of anisotropic or complex nanoparticles such as NPLs, which on first sight seem inherently thermodynamically unstable. A popular mechanism to justify their existence is called oriented attachment which describes the connection of two or more smaller nanostructures at energetically favourable facet interfaces. Subsequent reorientation, fusion and possible recrystallization of the nanocrystals then leads to larger crystals with variable dimensions and crystalline structure. Dipole interactions between the smaller nanostructures originating from asymmetric distribution of facets and/or shape are thought to be the main driving force of this process [70] but surfactants can also considerably affect the mechanism by (de)stabilizing or exposing/obstructing certain facets [69].
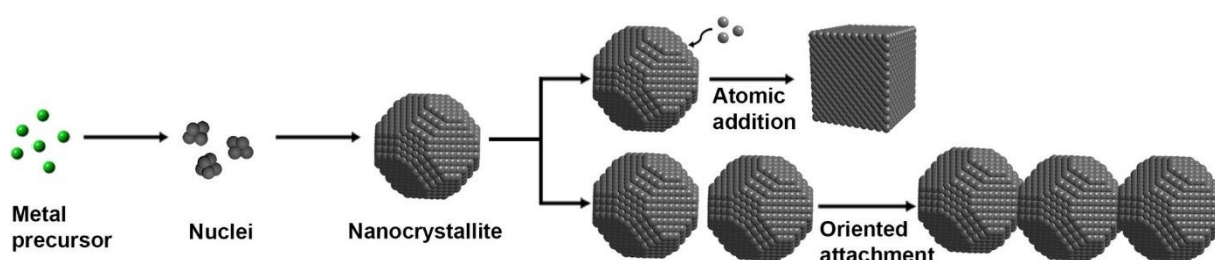
Figure 2.8: Graphic representation of different nanocrystal growth mechanisms [72]

To induce the supersaturated environment necessary for colloidal growth two main synthesis procedures can be recognized: heating up & hot injection [1] as shown in Figure 2.9. Both procedures try to achieve a short nucleation phase by rapidly increasing monomer concentration. The heating up method realizes this by quickly heating the precursor above its decomposition temperature leading to sudden thermal decomposition. The hot injection technique takes a different approach as it introduces the precursor(s) only after the reaction solution has been heated to high temperatures which then promptly dissociate into monomer complexes [71]. A variation of this method is to instead inject a chemical which catalyses the precursor dissolution [25].
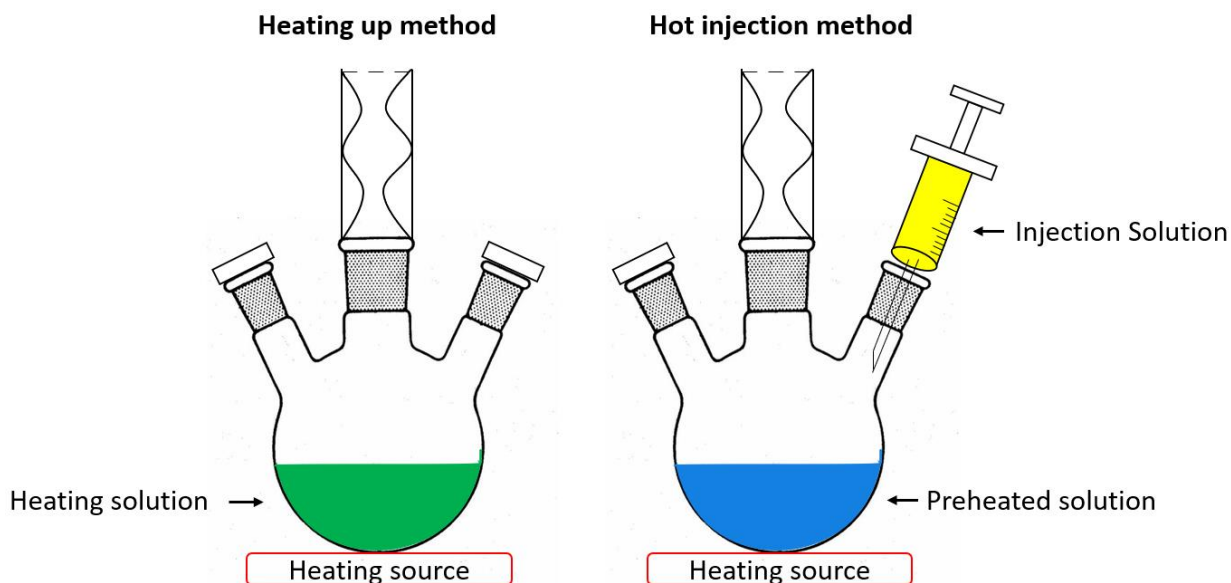
Figure 2.9: *Schematic representation of the two main colloidal synthesis procedures.*

All in all, it remains a difficult task to predict which specific conditions will induce successful colloidal synthesis due to the complexity of the system and thus the design of new protocols is still partly an empirical venture. However, knowledge on the fundamentals of colloidal nucleation and growth can be a useful tool to drive the process in the right direction.

2.2.2 Surfactants

One crucial aspect that has thus far been mostly absent from this discussion on NP growth mechanisms and their properties is the presence of surfactants which stabilize the monomer complexes and form a capping layer on the surface of any NP (Figure 2.10). These ligands generally consist of organic molecules which possess both a polar and non-polar segment. The polar group governs the interaction with the NP surface and the coordination with the construction atoms in solution while the apolar group dominates the relation with the reaction solution, which both have a significant influence on the diffusion rate of monomers and the growth mechanics of the NPs. It is also possible to employ ions as surfactants to stabilize the colloids using electrostatic forces [13].
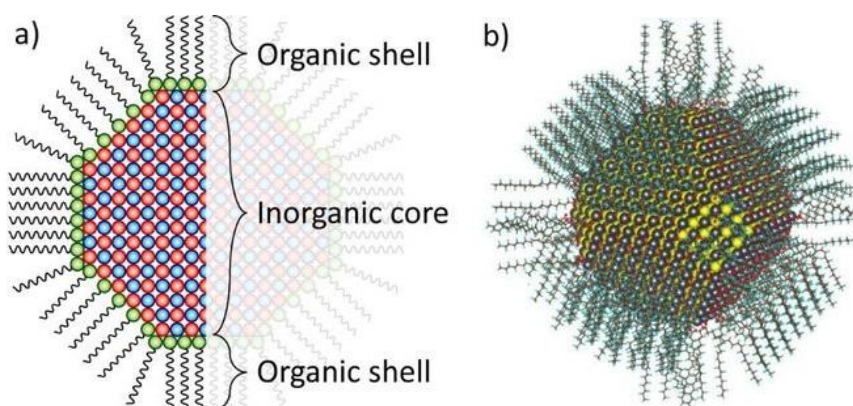
Figure 2.10: *Schematic representation of the organic shell and inorganic core of colloidal NPs [73]*

A wide selection of surfactant molecules are commonly available for colloidal synthesis. The head group (or binding group) usually includes functional groups consisting of electron donor atoms that can be feasibly incorporated in organic molecules such as nitrogen, oxygen, sulphur or phosphor. Regularly encountered functional groups include alkyl amines ($R-NH_2$), acids ($R-COOH$), alkyl thiols ($R-SH$) & alkyl phosphines ($R_3 P$). An important parameter to consider when evaluating the binding group is the ligand-atom binding strength. This needs to be strong enough to adequately stabilize the surface of the NP in solution and prevent uncontrolled growth but not too strong as it will inhibit NP growth by impeding the addition of monomers species to existing nuclei.

A quantitative model of the ligand-atom binding strength is not available thus far but the main ideas can be described by Lewis acid-base interactions [67]. These state that a smaller and/or higher charged ion (hard acid) will bind more strongly with species possessing large electronegativity and small polarizability (hard base) and vice versa. Other factors that can affect binding strength alkyl chain length (longer = stronger), number of donor atoms (more = stronger) and steric effects (bulky functional groups lead to lower binding affinity).

A powerful post-preparative method to influence the ligands present on the NC surface is called ligand exchange as shown in Figure 2.11. It can be used to transfer NCs to a different medium, attach them to surfaces or modify their properties such as shape. The exchange of weaker binding ligands with stronger binding ones is a feasible process, as only a low concentration of exchanging ligands is needed. The other way around is more time-intensive, as a larger quantity of exchanging ligands is needed and it might take a few days for the exchange reaction to reach equilibrium. It is also possible to reduce the concentration of ligands on the NC surface by adding ligand stripping agents or by performing vacuum treatment.
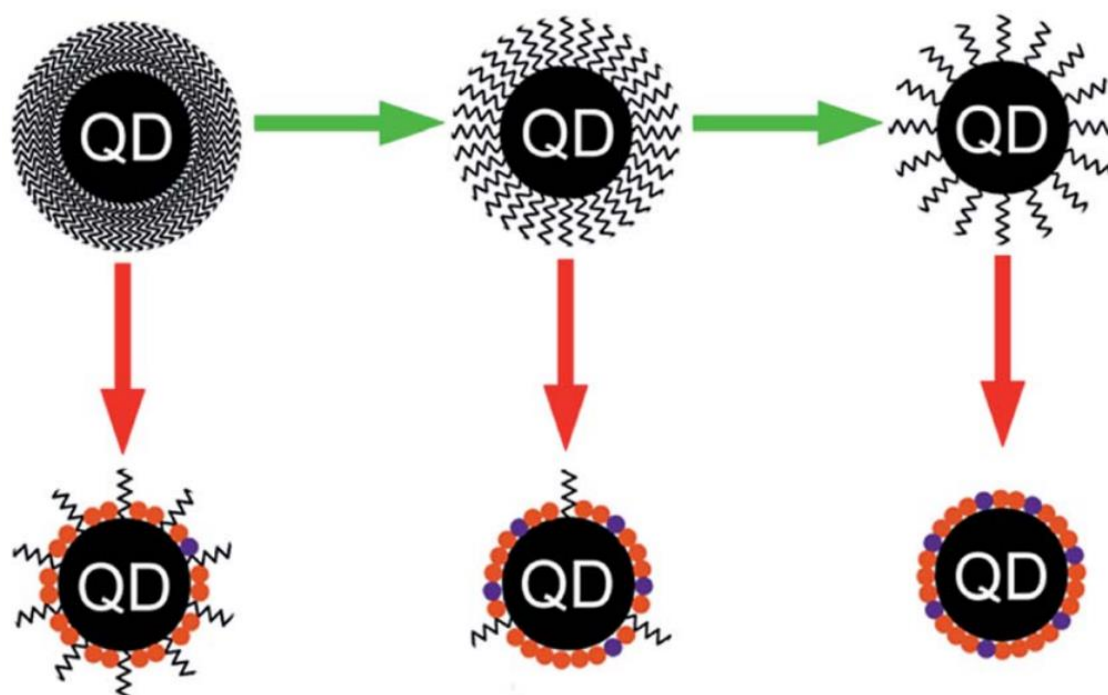

Figure 2.11: *Schematic representation of ligand exchange (red arrow) and stripping (green arrow) procedures [83]*

2.3 Bi₂Se₃ & Bi₂Te₃ NPLs

Of the theoretically predicted and experimentally verified TIs, Bi_2Se_3 and Bi_2Te_3 serve as a model system for a strong 3D TI due to its relatively simple band structure and single helical Dirac cone states combined with a relatively large bandgap (0.3 and 0.13 eV respectively) which allows for the observation of rare quantum phenomena induced by topological effects [8]. The materials have a matching rhombohedral crystal lattice structure (R$\overline{3}$m) which is constructed by stacking Quintuple Layer (QL) unit cells of approximately 1 nm height that lead to a well-defined hexagonal symmetry as depicted in Figure 2.12 [9]. These QLs are vertically bound by weak Van der Waals (VdW) forces while forming colloidal bonds within the lateral plane, allowing for strong anisotropic growth in the lateral directions and a uniform thickness within the range of 1 QL [10].
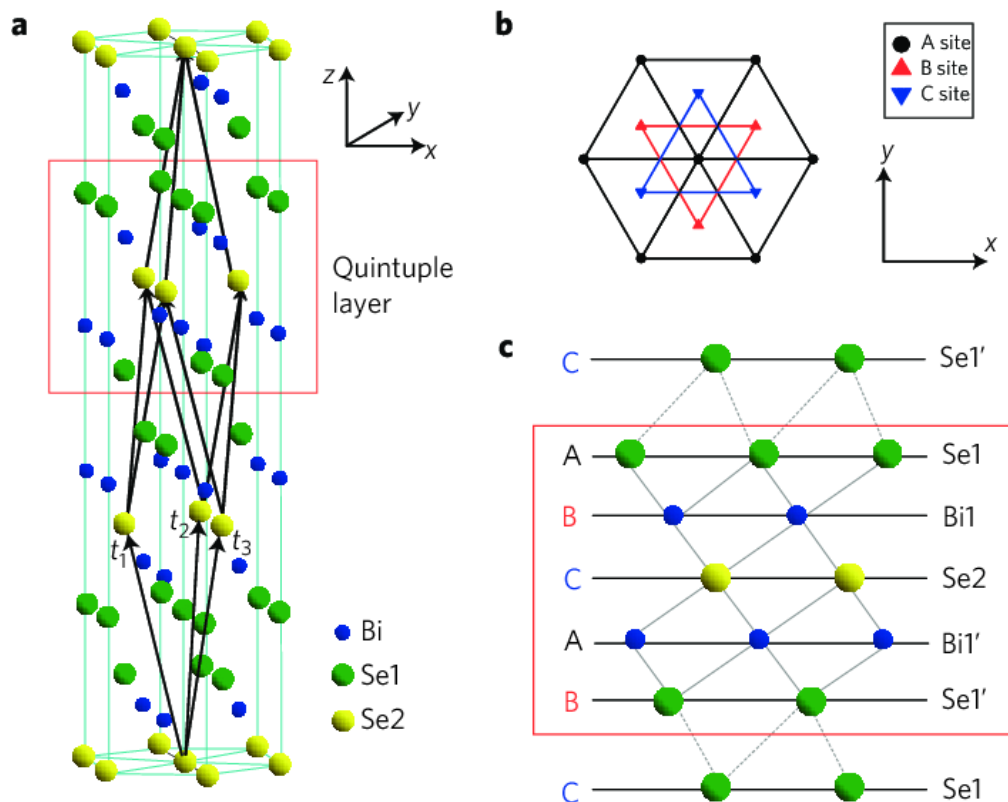
Figure 2.12: Crystal symmetry of Bi₂Se₃ [9]

Among the various realized geometries, 2D Nanoplatelets (NPLs) and sheets have received the most attention due to their varied possible procedures of synthesis and substantial surface to volume ratio which allows for the tuning and observation of diverse properties such as large-scale topological surface effects [47]. These NPLs have been shown to have applications in spintronics [53], optoelectronics [78], thermoelectric converters [3] [12] [24], integrated circuits [3], catalysis [28] [29] [48] [49], energy storage [38] [50], superconductors [44] [51] and even tumor treatment/imaging [52].

2.3.1 Known colloidal synthesis methods

Several colloidal synthesis procedures are known to induce 2D growth of Bi_2Se_3 & Bi_2Te_3 in the form on NPLs, including solvothermal [55], hot injection [14], microwave-assisted [27], liquid-phase exfoliation methods [29]. Figure 2.13 shows some representative results from previously reported syntheses. Here two frequently encountered and successful protocols will be discussed. The most

straightforward and therefore regularly used method is a polyol solution reflux protocol [54,55] (see Figure 2.13a) which employs ethylene glycol (EG) as a solvent and reducing agent [35] and Poly(vinylpyrrolidone) (PVP) as a surfactant. The NPLs acquired vary between hexagonal, truncated triangular or irregular polyhedral in shape, have a large lateral size distribution of tens of nm's to several µm's in diameter (see Figure 2.13b) but have a small distribution in thickness of only a few nms. The main advantage of this method is its simplicity as no additional actions except for heating and washing are needed to obtain high quality nanocrystals of uniform thickness.
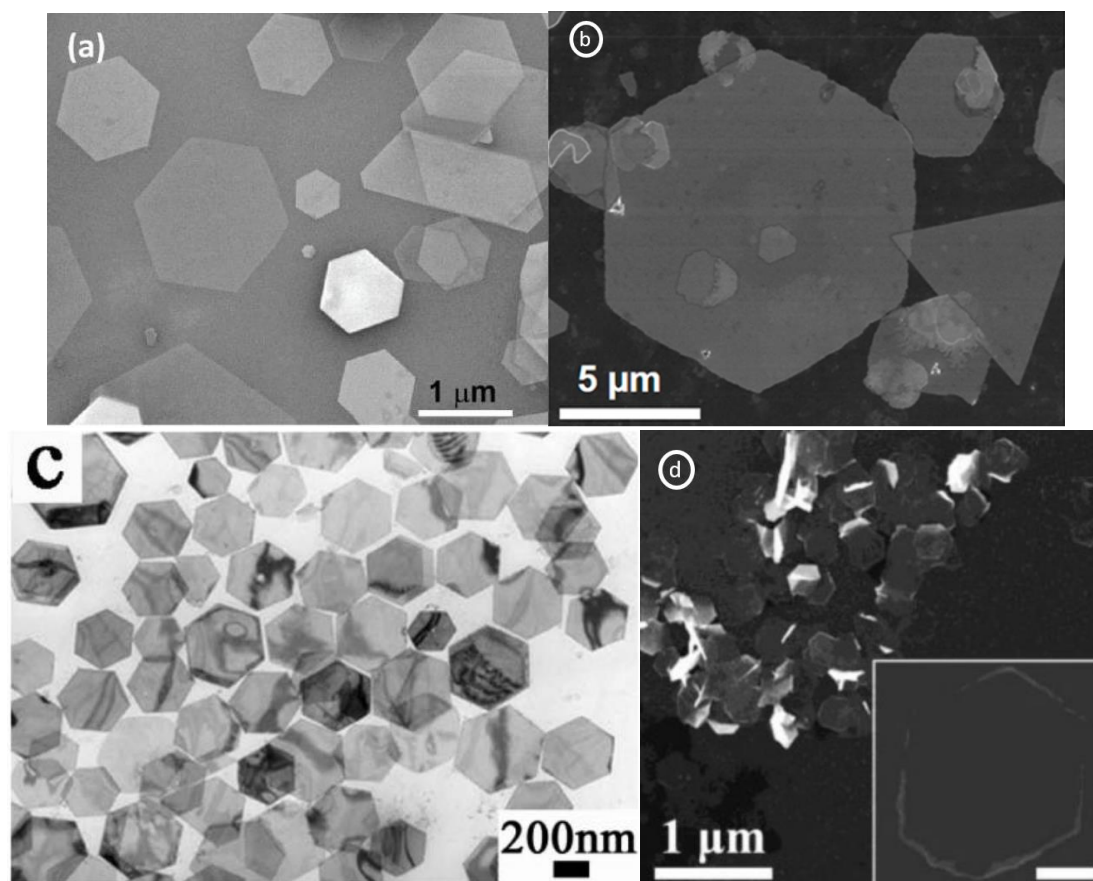
Figure 2.13: Representative TEM results of previously synthesized Bi₂Se₃ & Bi₂Te₃ NPLs by a) Polyol reflux [54], b) Polyol reflux with added sulfuric acid [12], c) Solvothermal synthesis [55] d) Hot injection synthesis [14]

Several variations of this method have been published that vary the existing parameters such as reaction time, surfactant concentration [24,35], addition of chemicals [15,35] and even sequential addition of a Te source to obtain layered $Bi_2Se_3@Bi_2Te_3$ heterostructures [25]. Some publications prefer a solvothermal method (see Figure 2.13c) where a sealed autoclave is utilized as a reaction chamber and heating source instead of more traditional glassware [55]. This allows more precise control over the reaction temperature and pressure during synthesis but limits the introduction of additional chemicals once the process has started.

Another popular method in nanomaterial synthesis is hot injection. In case of the bismuth chalcogenide NPL system however, hot injection is not often performed, probably due to the polyol method providing adequate results for the research needed. Few examples that employ hot injection procedures do exist (see Figure 2.13d) [14,77]. An interesting observation is that, for Bi_2Se_3 synthesis, a combination of 1-Octadecene (ODE), Oleic Acid (OA) and Oleyl amine (OLAM) are often

used as solvents and ligands instead of EG. Also, trioctylphosphine (TOP) which is regularly used to prepare metal chalcogenide nanomaterials via hot injection is too strong a reductor and has been shown to induce the quick formation of Bi and Bi_2O_3 nanoparticles instead of Bi_2Se_3 [28] [56]. This does not seem to be a problem for Bi_2Te_3 synthesis procedures [57]. Overall, it seems that the various hot injection procedures result in the formation of smaller NPLS when compared with the reflux and solvothermal methods, although its broad size and shape distribution could still be improved.

2.3.2 Possible Characterization Techniques

Lots of research has already been performed on the Bi_2Se_3 and Bi_2Te_3 system and its properties including but not limited to its: Morphologies, Heterostructures and Alloys, Surface ligands [11-13], Crystal structure [14-16], Elemental composition [23-25], Optical absorption/emission [26-29], Thermoelectric properties [30-34], Electrochemical characteristics [35-41], Quantum transport phenomena [42-45] and band structure [46].

As numerous types of syntheses to obtain Bi_2Se_3 and Bi_2Te_3 NPLs have been developed, various characterization techniques have also previously been employed to examine this system. In this section the most frequently employed and promising ones will be discussed, including what information they can and have provided thus far.

2.3.2.1 Electron Microscopy and Diffraction

It should not be a surprise when looking through the previous section that Transmission and Scanning Electron Microscopy (TEM & SEM) are the main methods by which bismuth chalcogenide nanoplatelets are imaged. The techniques measure the electrons of an electron beam that are transmitted through or reflected by a sample and enables the study of size, shape and surface morphologies as shown in Figure 4.14 [80].
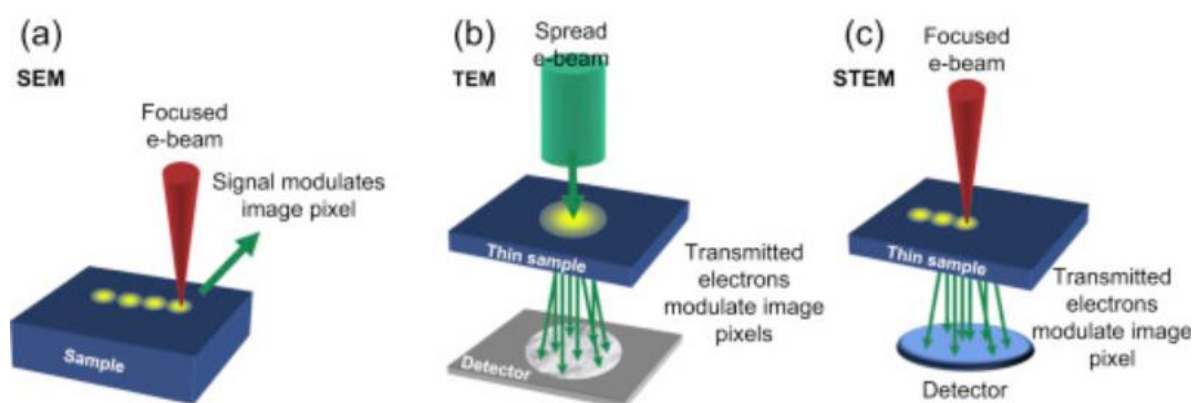
Figure 4.14: *Visual representation of different electron microscopy modes [80]*

The wavelength of these high energy electrons is significantly shorter in comparison to the photons used for conventional light microscopy, which means atomic resolution can be achieved. Furthermore, Bismuth is a heavy element (Z = 83) which provides plenty of contrast even in the few QL limit and therefore allows very thin NPLs to be identified. The combination of these two characteristics also allows for the identification of atomic lattice parameters and QLs using High Resolution TEM (HRTEM) in combination with Fast Fourier Transforms (FFT) and line scans of the image (see Figure 4.15c,e) [11,55].
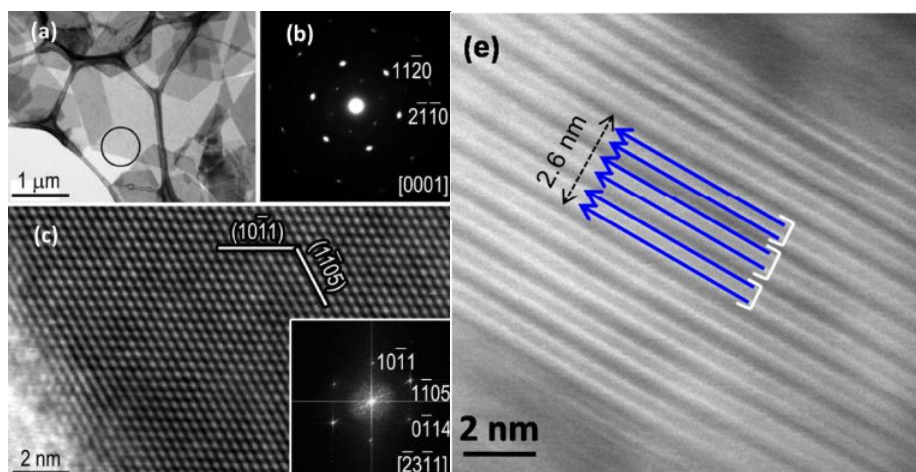
Figure 4.15: *EM analysis of a Bi₂Se₃ NPL: a) BF TEM b) ED of the encircled area in a. c) HRTEM of a horizontal NPL showing its atomic lattice + FFT analysis of the image [55] e) HRTEM of a vertical NPL showing resolved QLs [11]*

Some electron microscopes can additionally use their electron beam to perform Electron Diffraction (ED) to further investigate the material's crystal structure (see figure 4.16), which measures the periodically scattered electrons from the main electron beam. An example of ED can be seen in Figure 4.15b, which shows a sixfold [0001] lattice symmetry that is indicative of the Bi₂Se₃ NPL lateral crystal structure and can be used to judge its overall crystallinity and characterize possible defects by the location and shape of the spots in the diffractogram. It has been shown regularly that good quality nanocrystals can readily be obtained through colloidal synthesis [14,26,55].
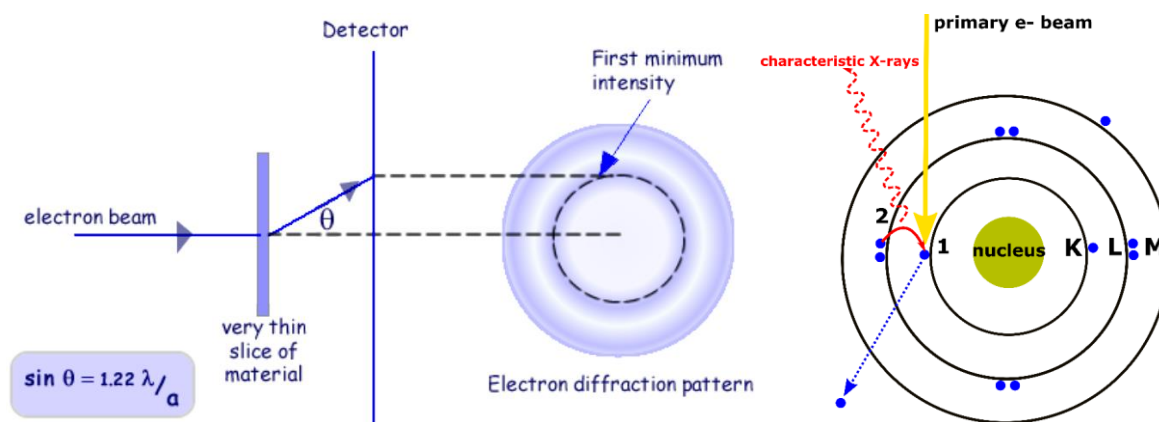
Figure 4.16: *Visual representations of the basic principles behind ED (left)[84] and EDX (right) [86].*

2.3.2.2 X-ray Diffraction and Energy Dispersive X-ray Spectroscopy

ED is not the only diffraction-based technique used to study the crystallinity of Bismuth Chalcogenide nanostructures. X-Ray Diffraction (XRD) is used frequently as well due to the instrument being widely available and its relatively fast and straightforward sample preparation and measurements [85]. It works on the same basis as ED in that it analyses the particles diffracted from the main beam by the material, however it uses x-rays instead of electrons as a beam source. This influences the conditions under which measurements can be performed (for example XRD can be performed in ambient atmosphere) and what type of information can be gained from the results as the x-rays differ in energy, wavelength, attenuation length, etc. For Bi₂X₃ NPLs XRD is mainly used to confirm its rhombohedral crystal structure [14] but can also make some judgements on its crystallite

size and preferred stacking orientation based on peak width and relative height [85]. An example of such a diffractogram and its comparison to simulated values is given in Figure 2.17, with peaks marked with their respective miller indices.
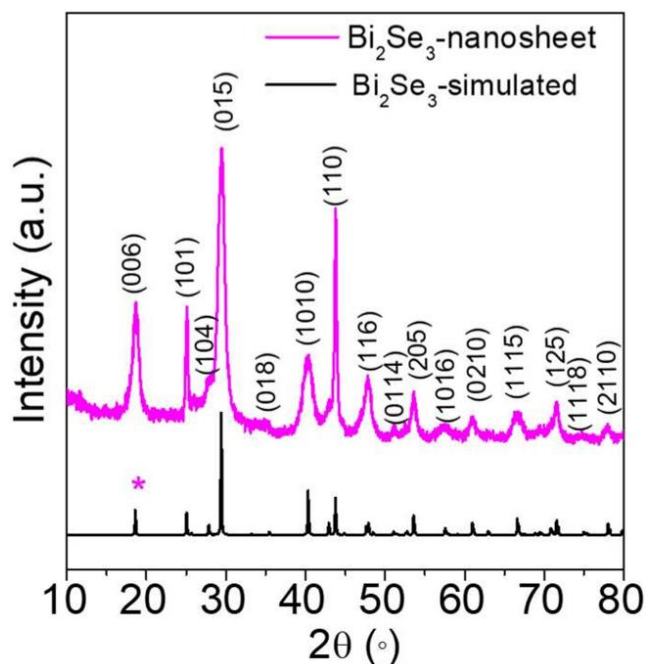
Figure 2.17: *XRD diffraction patterns of Bi$_2$Se$_3$ nanosheets vs simulated data [11].*

Another technique that employs X-rays is called Energy dispersive X-ray spectroscopy (EDX), which instead measures characteristic x-rays that are emitted by electrons that jump to a lower electron shell (See Figure 2.16). Figure 2.18 shows an example of EDX which is being used to map the distribution of elements (specifically Bi and Se) in the NPL as well as their overall presence to determine if stoichiometric Bi$_2$Se$_3$ has been achieved. The results show a homogeneous distribution of Bi and Se throughout the platelet. By varying the ratios of elements present during the synthesis it has been shown that compounds with different Bi and Se fractions can be obtained [11] and even subsequent layered growth of Bi$_2$Te$_3$ and Bi$_2$Se$_3$ can be achieved [25].
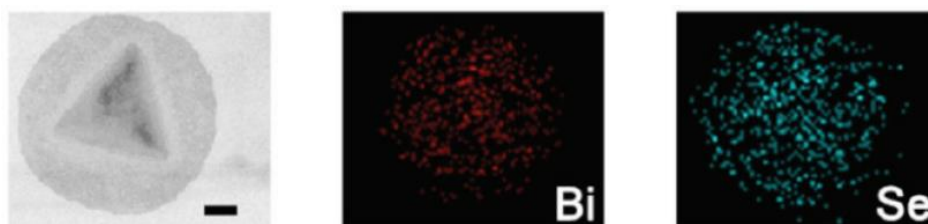
Figure 2.18: *Spatially resolved EDX measurement showing Bi and Se distributions within an NPL [15].*

2.3.2.3 Scanning Probe Microscopy

Scanning probe microscopy is a surface characterization technique that works by measuring the interactions between an (often atomically) sharp tip and the surface, which results in a topographic image as seen in Figure 2.19. The fundamental difference between Atomic Force Microscopy (AFM) and Scanning Tunnelling Microscopy (STM) in this regard is that AFM measures the direct force applied on the tip by the proximity to the surface, while STM measures the tunnelling current between the tip and the surface. Both of these techniques have their advantages and disadvantages;

however it is important to note that only STM is able to measure the local conductivity through its tunnelling current, which is essential in the characterization of topological surface states.
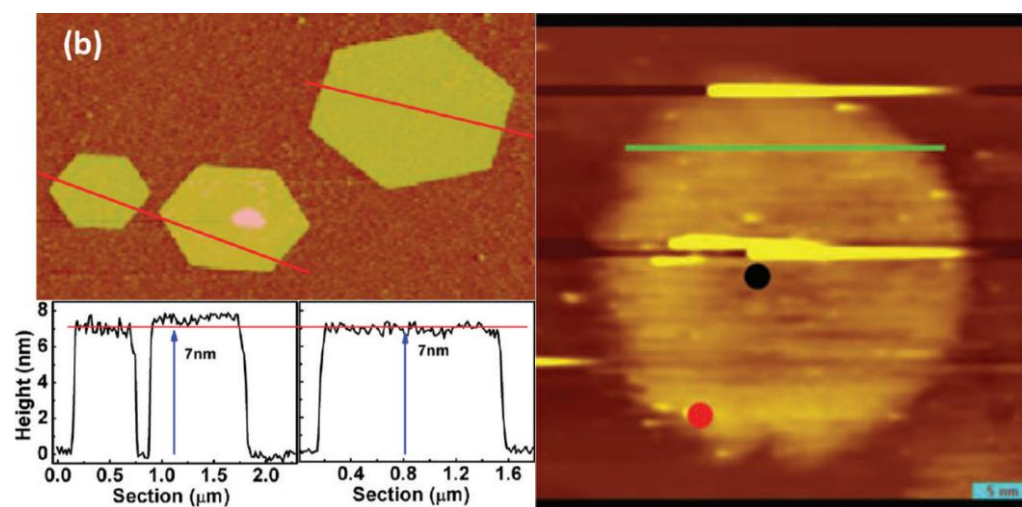
Figure 2.19: *Topographic images of Bi₂Se₃ NPLs obtained with AFM (left) [55] & STM (right) [87]*

2.3.2.4 Surfactant characterization

Proton Nuclear Magnetic Resonance spectroscopy (¹H-NMR) is a characterization technique which distinguishes protons by their magnetic resonance frequency. This frequency is strongly dependent on its chemical environment, and thus different hydrogen groups can be distinguished in a single molecule. As such, each molecule has a distinct resonance frequency pattern which can be identified (as long as hydrogen is present). This is especially effective for small organic molecules or polymers with repeating patterns and as such can be utilized to characterize organic surfactants present on NCs. However, we have not found any examples in literature that employ this technique in characterizing ligands on a Bi₂Se₃ or Bi₂Te₃ NPL surface. Therefore, an example of ¹H-NMR of PVP on another NC system is given in Figure 2.20.
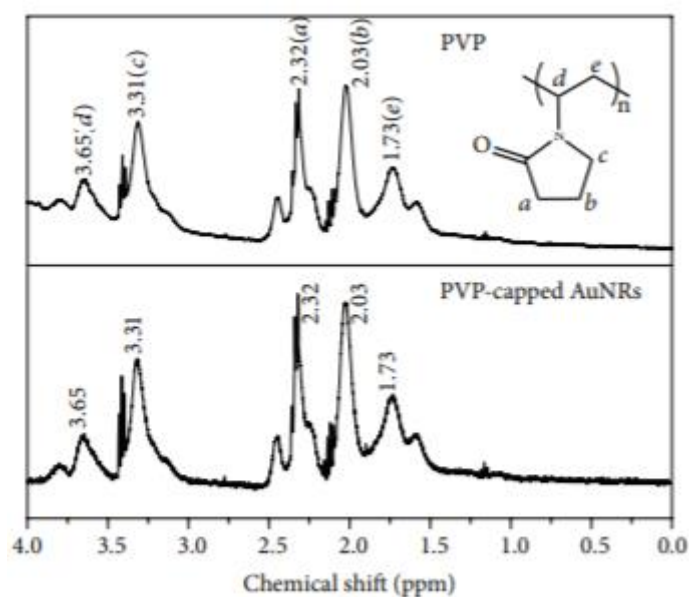
Figure 2.20: *¹H-NMR spectrum of PVP characterized on gold nanorods [88]*

Lastly, Fourier-Transform Infrared Spectroscopy (FTIR) is another characterization technique which can be used to identify ligands on NCs. It is works on the same basis as other light absorption methods such as UV-VIS, however it can acquire data more quickly and over a broader spectral range. This is because rather than obtaining data by measuring absorption of a monochromatic light source, it instead uses a multi-frequency light source of which the absorption data can be reverse engineered using a Fourier transform. This absorption spectrum gives information on the characteristic vibrations present in the organic surfactants present on the NC, which can be used to identify them. A representative FTIR image is shown in Figure 2.21.
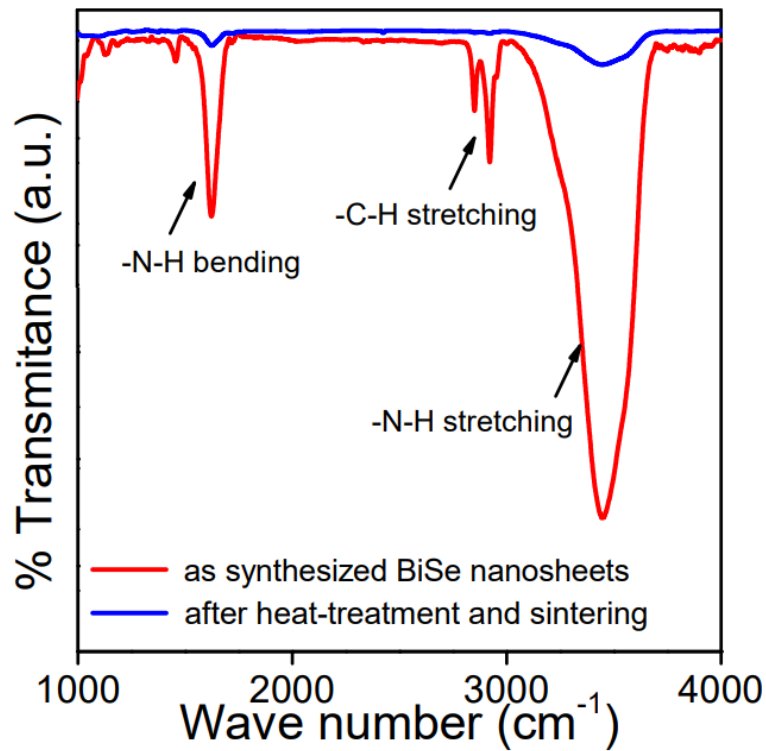
Figure 2.21: *A FTIR spectrum of Bi$_2$Se$_3$ Nanosheets before and after heat treatment [11].*

Chapter 3.

Experimental methods

This chapter will present the steps that were performed to obtain the results discussed in the succeeding sections including the synthesis, ligand treatment and characterization of Bi_2Se_3 & Bi_2Te_3 NPLs.

3.1 Chemicals

Table 3.1: A full list of chemical substances used in the synthesis of Bi_2Se_3 & Bi_2Te_3 NPLs and its ligand treatment procedures.

Chemical Substance	Chemical Formula	Abbreviation	Purity
Bismuth Nitrate Pentahydrate	$Bi(NO_3)_3.5H_2O$	BiNO	99.99%
Bismuth (III) Oxide	Bi_2O_3	Bi2O3	99.8%
Bismuth (III) Acetate	$Bi(CH_3O_2)_3$	Bi-Ac	99.99%
Sodium Selenite	Na_2SeO_3	SSe	99%
Selenium powder	Se	Se	99.99%
Tellurium Oxide	TeO_2	TeO2	99%
Polyvinylpyrrolidone	$(C_6H_9NO)_n$	PVP	?
Ethylene Glycol (anhydrous)	$HOCH_2CH_2OH$	EG	99.8%
Ethanol (anhydrous)	CH_3CH_2OH	EtOH	99.5%
Sodium Hydroxide	NaOH	NaOH	97.0%
1-Octadecene	$CH_3(CH_2)_{15}CH=CH_2$	ODE	90%
Acetone (anhydrous)	CH_3COCH_3	ACE	99.5%
Acetonitrile (anhydrous)	CH_3CN	ACN	99.5%
Hexane	$CH_3(CH_2)_4CH_3$	HEX	95%
Acetic Acid	CH_3COOH	AA	99%
Oleic Acid	$CH_3(CH_2)_7CH=CH(CH_2)_7COOH$	OA	99%
Oleyl Amine	$CH_3(CH_2)_7CH=CH(CH_2)_7CH_2NH_2$	OLAM	70%
Toluene (anhydrous)	$C_6H_5CH_3$	TOL	99.8%
Isopropyl Alcohol	$(CH_3)_2CHOH$	IPA	98%
Potassium Hydroxide	KOH	KOH	85%
Sodium Amide	$NaNH_2$	NaNH2	95%
Sodium Sulfide	Na_2S	Na2S	90%
Sodium Hydrosulfide	NaHS	NaHS	90%
1-dodecanethiol	$CH_3(CH_2)_{11}SH$	DDT	98%
Sodium Borohydride	$NaBH_4$	NaBH4	99%
Chloroform	$CHCl_3$	CHCl3	99%
Chloroform (deuterated)	$CDCl_3$	CDCl3	99.8%
Tributylamine	$[CH_3(CH_2)_3]_3N$	TBA	99%
Thiophenol	C_6H_5SH	TP	99%
Hydrazine Hydrate	$N_2H_4.H_2O$	N2H4	98%
Potassium bromide	KBr	KBr	99%
Ferrocene	$Fe(C_5H_5)_2$	FER	98%

3.2 Synthesis of Bi₂Se₃ & Bi₂Te₃ NPLs

The attempted synthesis procedures of Bi_2Se_3 NPLs are based on the work published by Zhang *et al.* (2011) [54] & Wei et al. (2013) [14], although several variations on the procedure are performed in an effort to improve the protocol. These are further described in the chapter 4.1.1 & 4.1.2. Finally a modified procedure which combines features of both protocols is designed and optimized, as described in 4.1.3.

3.2.1 Polyol Reflux

The following chapter describes a typical Bi_2Se_3 NPL synthesis using the polyol reflux protocol based on [54]. A schematic overview is given in Figure 3.1. The process is equivalent for Bi_2Te_3 upon exchanging 50 mg SSe with 100 mg of TeO_2 and the addition of 300 mg of NaOH to the initial reaction solution.

Figure 3.1: Schematic overview of the polyol reflux synthesis for obtaining Bi₂Se₃/Bi₂Te₃ NPLs.

50 mg of SSe, 100 mg of BiNO and 220 mg of PVP are dissolved in 10 mL of EG in a 50 mL round-bottom flask, attached to a vigreuxcolumn and heated to 190°C under atmospheric conditions which induces a gradual colour change to transparent yellow (100°C), cloudy yellow (150°C) and cloudy orange (190°C). Once the solution reaches 190°C the temperature is maintained for 120 minutes. Over the course of 15 minutes at 190°C the solution gradually turns black. After 120 minutes, the heating source is removed and the reaction is quenched by cooling the mixture rapidly with a water bath to RT.

The black product is then transferred to a scintillation vial and washed by adding 10 mL of IPA followed by centrifugation for 10 minutes at 3000 RPM (all times and speeds are equivalent for any future centrifugation steps mentioned). A dark black supernatant on top of black precipitate is obtained. The supernatant is discarded and the washing steps are repeated once more before redispersing the precipitate in 10 mL of IPA. All products are stored at room temperature under atmospheric conditions.

3.2.2 Hot Injection by Wei et al.

The following chapter describes a typical Bi_2Se_3 NPL synthesis using the hot injection protocol based on [14]. A schematic overview is given in Figure 3.2. No Bi_2Te_3 NPLs syntheses were attempted using this method as a basis.
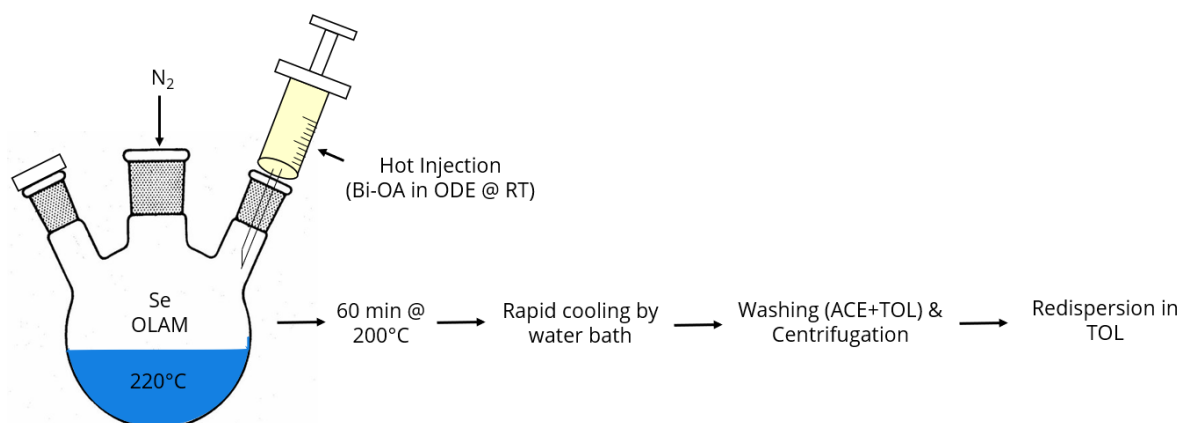
Figure 3.2: Schematic overview of the hot injection synthesis for obtaining Bi_2Se_3 NPLs.

The Bi precursor (Bi-OA) was prepared by adding 650 mg of Bi-Ac to 3.2 mL OA & 25 mL ODE in a 50 mL round-bottom flask under N_2 atmosphere. The solution was heated to 120°C for 60 minutes and subsequently heated to 160°C for 60 minutes, to form a yellow transparent solution which was then cooled to room temperature.

50 mg of Se and 6.6 mL of OLAM were added to a 50 mL round-bottom flask under N_2 atmosphere. The solution was heated to 120°C for 60 minutes and subsequently heated to 190°C until a yellow transparent solution is formed. The Se solution was then heated to 220°C before injecting 3 mL of the Bi precursor inducing a immediate colour change to black, after which the temperature is decreased to 200°C and maintained for 60 minutes. Subsequently the heating source is removed and the reaction is quenched by cooling the mixture with a water bath to RT.

The black product is then transferred to a scintillation vial under N_2 atmosphere in a glovebox and washed by adding 5 mL of TOL (solvent) and 5 mL of ACE (anti-solvent) followed by centrifugation. A dark black supernatant on top of black precipitate is obtained. The supernatant is poured in a different scintillation vile and stored separately. The washing steps are repeated once more before redispersing the precipitate in 10 mL of TOL. All products are stored under N_2 conditions for stability.

3.2.3 Modified Polyol Hot Injection

The following chapter describes a typical Bi_2Se_3 NPL synthesis using the modified polyol hot injection protocol. A schematic overview is given in Figure 3.3. The process is equivalent for Bi_2Te_3 upon exchanging SSe with 100 mg of TeO_2 and the addition of 300 mg of NaOH to the initial reaction solution.
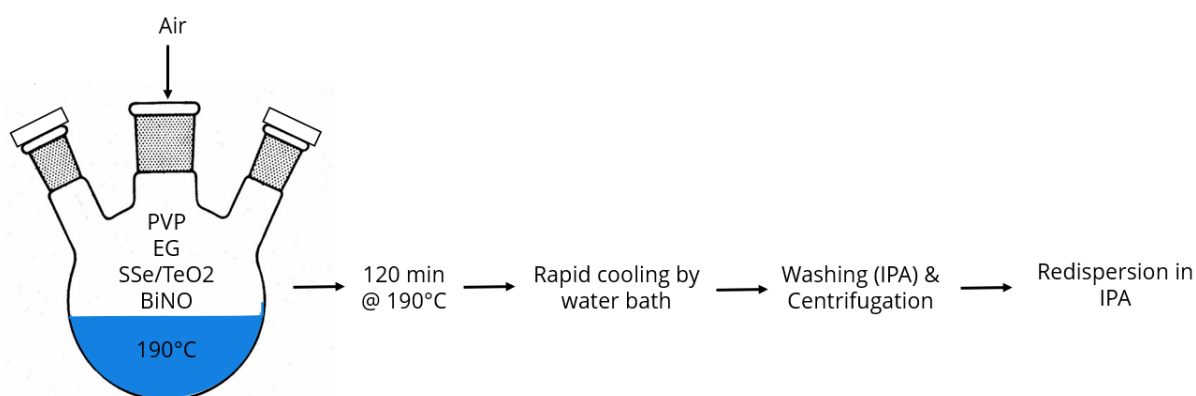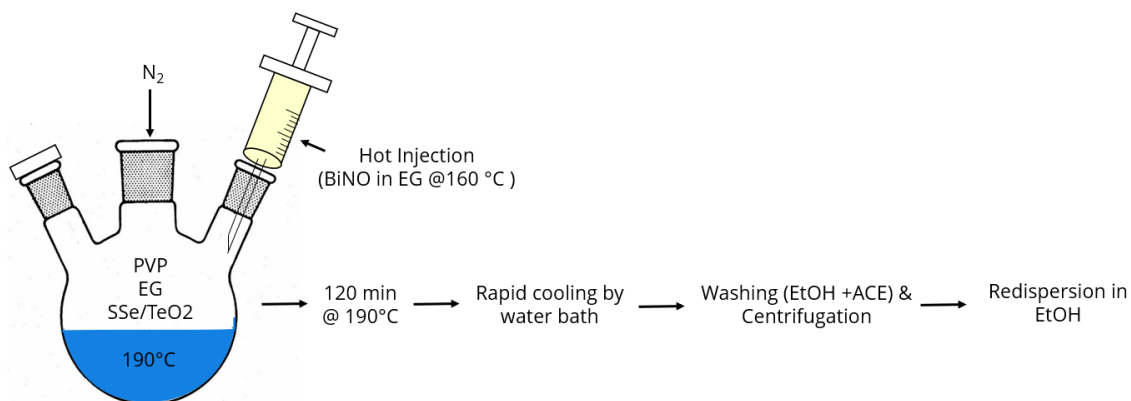

Figure 3.3: Schematic overview of the modified polyol hot injection synthesis for obtaining Bi_2Se_3/Bi_2Te_3 NPLs.

The Bi precursor was prepared by dissolving 100 mg of BiNO in 0.5 mL of degassed EG under N_2 atmosphere (in a glovebox). The solution was heated while stirring to 160°C indicated by gas formation and a colour change from colourless to turbid white prior to injection in the reaction mixture.

50 mg of SSe and 220 mg of PVP were dissolved in 9,5 mL of EG in a 50 mL round-bottom flask and are degassed under vacuum in a schlenkline at 70°C while stirring for 15 minutes until no more gas formation in the form of bubbles are observed. The Se solution is then heated to 190°C under N_2, which induces a gradual colour change to yellow (120°C), orange (130°C) and finally black (135°C). Once the solution reaches 190°C the preheated Bi precursor is injected, the temperature is maintained for 120 minutes. Subsequently the heating source is removed and the reaction is quenched by cooling the mixture with a water bath to RT.

The black product is then transferred to a scintillation vial under N_2 atmosphere in a glovebox and washed by adding 10 mL of EtOH (solvent) and 10 mL of ACE (anti-solvent) followed by centrifugation. A dark black supernatant on top of black precipitate is obtained. The supernatant is poured in a different scintillation vile and stored separately. The washing steps are repeated once more before redispersing the precipitate in 20 mL of EtOH. All products are stored under N_2 conditions for stability.

3.3 Ligand Treatment of Bi_2Se_3 NPLs

To prevent NPL aggregation, which occurs naturally in solution, the as-synthesized NPLs were treated with various ligand exchange or stripping agents. These were based on several different papers on PVP removal from a diverse range of nanoparticle systems (NaBH$_4$/TBA [94], N_2H_4 [25], thiols [95], OLAM [96]), although the general procedure was similar. A schematic representation of this process is shown in Figure 3.4.
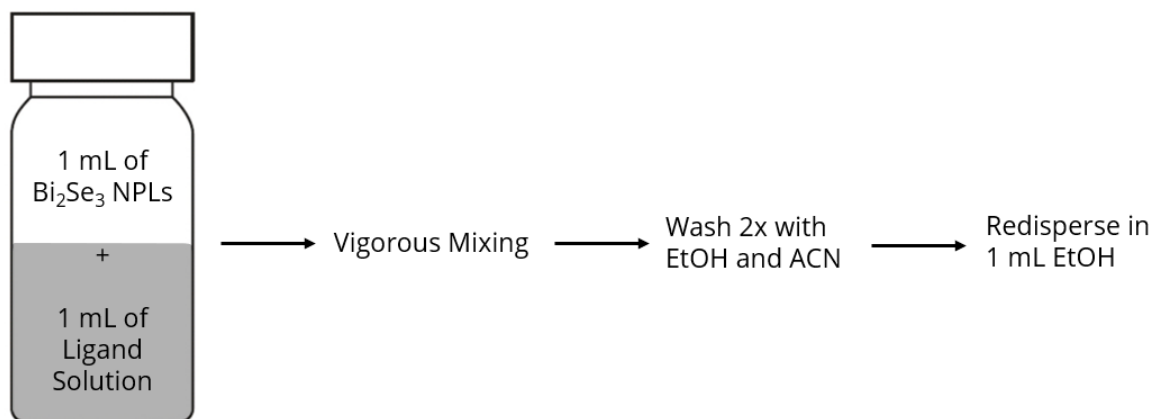
Figure 3.4: Schematic overview of Bi$_2$Se$_3$ NPL Ligand Treatment

1 mL of ligand solution (DDT, NaBH$_4$, CHCl$_3$, TBA, TP, N$_2$H$_4$ or OLAM) is added to 1 mL of product and shaken vigorously. The mixture was then centrifuged to precipitate the NPLs and separate them from PVP. The supernatant was removed and the NPLs were redispersed in 1 mL of EtOH with the help of a sonication, after which the ligand treatment was repeated once more. The treated dispersion was then washed to dispose of unbound ligands by adding 1 mL of EtOH (solvent) and 5 mL of ACN (anti-solvent) followed by centrifugation. The washing steps were repeated once more before redispersing the precipitate in 1 mL of EtOH by sonication.

3.4 Characterization of Bi$_2$Se$_3$ & Bi$_2$Te$_3$ NPLs

An assortment of methodologies was utilized to characterize the NPLs to allow for a broad range of features to be examined including: morphology, crystallography, presence and identification of ligands and electronic properties. For this purpose, characterization was performed by: Transmission Electron Microscopy (TEM), High-Angle Annular Dark-Field Scanning Transmission Electron Microscopy (HAADF-STEM), Energy Dispersive X-ray spectroscopy (EDX), Electron Diffraction (ED), X-Ray Diffraction analysis (XRD), Atomic Force Microscopy (AFM), Scanning Tunnelling Microscopy (STM), Ultraviolet-visible spectroscopy (UV-Vis), Fourier-Transform Infrared Spectroscopy (FTIR) and Nuclear Magnetic Resonance spectroscopy (NMR).

3.4.1 HAADF-S(TEM), ED & EDX

Standard electron microscopy samples were prepared by drop-casting 10 μL of diluted stock solution on a 200 mesh Cu(100) grid. For high resolution measurements a holey carbon or formvar grid was used instead and sample grids were cleaned after drop-casting by suspending them above heated acetone and letting it condensate on the grids to wash of organic contamination. Sometimes a plasma cleaning procedure of 15 seconds was implemented to further clean the samples. TEM was performed on either a FEI Tecnai 20 or a TALOS L120C, the latter of which also allowed for ED data to be recorded. HAADF-STEM images were acquired on a FEI TALOS F200X or Thermo Scientific Spectra 300 (acceleration voltage = 200 kV), which additionally enabled the use of spatially resolved EDX.

3.4.2 XRD

X-ray diffractograms with a range of 10 to 65° were recorded on a Philips PW 1729 X-ray generator (V = 40 kV and A = 20 mA) with a Cu K$_a$ source and wavelength of 1.5418 Å. Sample preparation was carried out by either a drop-casting or dry powder procedure. In the drop-casting procedure a few drops of undiluted sample were deposited on a custom Si(100) sample plate, which were left to

evaporate before the procedure was repeated 3 more times. The dry powder procedure was carried out by drying a whole sample stock solution at 100°C for 2 hours before transferring to a standard powder XRD sample plate. Obtained diffractograms were overlayed with high quality reference data from the Inorganic Crystal Structure Database (ICSD) (collection code: 165226).

3.4.3 SPM

AFM measurements were carried out on a JPK Nanowizard 2 operating in intermittent-contact mode in ambient atmosphere using Bruker OTESPA-R3 or µmesh CSC37/NoAl tips. Sample preparation was achieved by either drop-casting or spin-coating (2500 rpm for 2 minutes) 4 drops (≈20 µL) of diluted stock solution (0-20x diluted) onto a freshly cleaved mica surface. During spin-coating the described procedure was repeated for each droplet to limit the aggregation of NPLs on the surface.

STM experiments were conducted on a ScientaOmicron POLAR SPM under ultra-high vacuum (10^{-10} bar) and ultra-low temperature (4.5 K) conditions. NPLs were identified by scanning over a surface in constant-current feedback mode using an ultrasharp tungsten tip prepared on copper. Sample preparation was achieved by either drop-casting or spin-coating (1500 rpm for 2 minutes) 1 droplet of diluted stock solution (0-10x) on either a Phasis epitaxially grown Au(111) 200 nm thin film on mica or a Highly Ordered Pyrolytic Graphite (HOPG) substrate which was freshly cleaved using adhesive tape.

3.4.4 Absorption Spectroscopy

UV-Vis absorption spectroscopy was performed by a PerkinElmer Lambda 950 UV/VIS/NIR spectrophotometer, with a measured range of 300 - 2000 nm and step size of 1 nm. Samples were prepared by diluting samples in a quartz cuvette of 1 cm path length and a solvent (EtOH) reference spectrum was internally subtracted from all sample spectra.

FTIR spectra were recorded on a Vertex 70 FTIR Spectrometer in a range of 400-8000 cm^{-1}. Samples were prepared by mixing 2 mg of PVP or 1 mL of undiluted sample with 200 mg of pre-dehydrated KBr in a mortar and pestle. These powders were then converted into clear pellets by a Specac & Anadis pellet press. A pure KBr reference spectrum was internally subtracted from all performed measurements.

3.4.5 ^{1}H-NMR

Samples for H-NMR spectroscopy were prepared by drying undiluted NPL stock solution (either 0.6 or 0.9 mL) in a vacuum chamber until no more solvent was observed and were redispersed in 0.6 mL of $CDCl_3$ by sonicating for 10 minutes. Some samples also included 10 µL of a 0.05 M ferrocene reference solution to possibly obtain quantified concentrations of ligands. Additional ligands (2.5-5 mg of PVP) were also added to some samples to check if PVP could be measured in small concentrations in the presence of NPLs. H-NMR measurements were performed using an Agilent MRF400 equipped with a OneNMR probe and Optima Tune system. Spectra were recorded according to the following parameters: 400 MHz, CDCl3, 25C." with a rest time of 25-1 seconds depending on the stability of the sample.

Chapter 4.

Results and Discussion

In this chapter firstly the results concerning the formation of Bi_2Se_3 & Bi_2Te_3 NPLs will be discussed. Several published synthesis methods were investigated as the initial procedures could not be adequately reproduced. Some variations in the procedures are investigated until a successful method is realized. The second part of the chapter shifts its focus to study the surfactants present on the NPLs and the possibility of exchanging and/or removing them for better STM performance.

4.1 Variation and optimization of Bi_2Se_3 & Bi_2Te_3 NPL synthesis

As discussed in Theory section 2.3.1, Bi_2Se_3 & Bi_2Te_3 NPLs have been readily produced using various similar synthesis procedures. However, no publications were found which discussed the process of preparing NPLs that meet the requirements for STM measurements such as size control, level of aggregation & surfactant removal in detail. Two articles [97,93] were found which successfully imaged Bi_2Se_3 NPLs using a synthesis procedure very similar to the generally established polyol reflux method [25]. Yet the process of preparing for and transferring the NPLs to the STM is limited to a single sentence, which lend itself more as a guideline than an exact protocol. The necessary chemicals to replicate the aforementioned synthesis were also not promptly available. Therefore, a similar procedure was chosen as a starting point.

4.1.1 Bi_2Se_3 & Bi_2Te_3 NPL synthesis by Polyol reflux

Initially an attempt was made to reproduce a broadly employed polyol reflux synthesis [54] to obtain homogeneous flat Bi_2Se_3 NPLs. A similar procedure is also available for Bi_2Te_3 NPLs [55]. The ability to tune the lateral dimensions of the NPLs to some extent is needed, as the ones published are generally too large ($\approx$ 1μm diameter) for practical measurements in the STM. Also, horizontally settled individual NPLs are required for proper imaging so aggregation should be minimized.

Figure 4.0a shows a TEM image of the initial reproduction of [54]. Aggregates of large rectangular microstructures dominate the population, which are vastly dissimilar to the desired 2D nanostructures. It is unclear what exactly is to blame for the failed synthesis as the published description of the synthesis procedure is quite concise. Therefore, it lacks several possibly relevant parameters such as atmospheric conditions (air vs inert), heating rate, cooling method and washing procedure specifics (centrifugation rate/duration & solvent quantity). It was theorized that the heating rate and reaction environment would have the most significant influence on the resulting morphology because these directly affect the nucleation rate and growth speed which could explain the incredibly large particle size and where therefore investigated first.

The result of increasing the heating rate from 30 min to 15 min is shown in Figure 4.0b. However, a good representation of the sample could not be shown in 1 image as a broad range of different structures were observed throughout the measurements, although most of these did not display plate-like morphology. The figure does show a small population of aggregated platelets with some hexagonal features, although they are overshadowed by the divergent microscale structures which would make characterization using atomic probe techniques unfeasible. Nevertheless, it certainly represents a step in the right direction in comparison to initial results and as such the increased heating rate was kept during future syntheses.
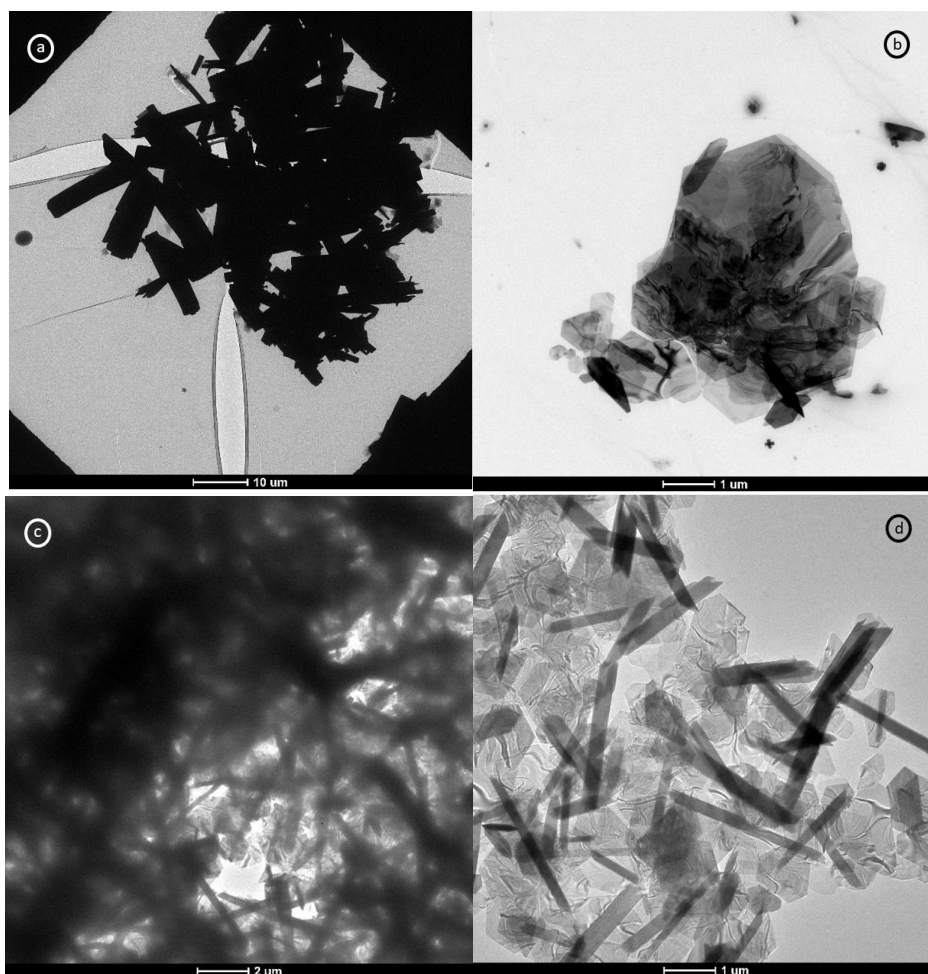
Figure 4.0: *Representative TEM images of Bi$_2$Se$_3$ structures obtained by [55] with varied parameters a) 30-minute heating time, b) 15-minute heating time, c) N$_2$ environment instead of Air, d) Sample c) after size selective precipitation.*

Changing the reaction environment from air to N$_2$ further enhances the quality and yield of platelets, presumably because nanocrystals are often sensitive to air and moisture [73]. However, a Size Selective Precipitation (SSP) procedure was needed to extract the smaller nanostructures present in the sample (Figure 4.0c,d). Two distinct populations of similar dimensions are observed: plate-like and rod-like nanostructures, of which the latter display a higher contrast signifying increased thickness and/or higher electron density due to the presence of heavy elements. One explanation for the existence of the elongated structures was the possibility of nanoplatelets folding up on themselves to form nanotubes which could possibly be unrolled to again form 2D structures. Another theory is that the increased contrast of the rods could arise from a higher Bi concentration.

To verify their chemical composition the two populations were analysed using EDX, which resulted in a near stoichiometric distribution of Bi (64%) & Se (36%) in the platelets, while the rods contained a different distribution of elements consisting of Bi (70%) and Se (30%). Furthermore, during the measurement the rods were observed to melt under the high intensity electron beam which on top of their decreased stability when compared to the NPLs revealed an amorphous ordering instead of long-range crystallographic facets. Thus, it was concluded that the rods were likely not nanotubes but some other form of amorphous nanostructure of which the further study had no immediate merit. The goal then became to modify the synthesis procedure of [54] to prevent the formation of rods.

31
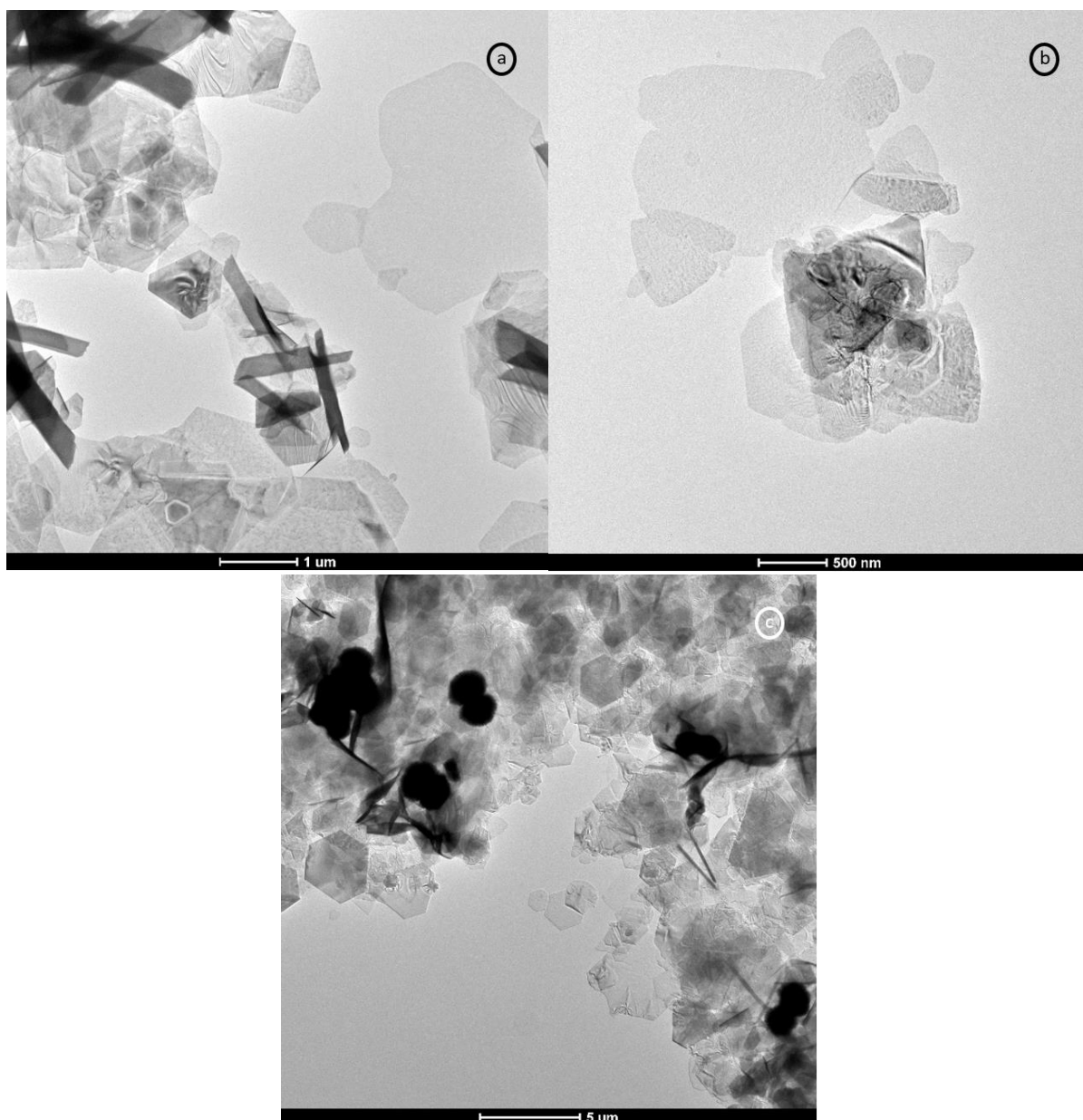
Figure 4.1: *Representative TEM images of Bi$_2$Se$_3$ NPLs obtained by [54] with varied Bi and Se concentrations. a) 50% reduction of Se, b) 50% reduction of Bi, c) 50% reduction of Se & Bi.*

The initial parameter that was varied was the (relative) concentration of Bi and Se compounds present in the reaction solution. It was hypothesized that a non-stoichiometric proportion of bismuth and selenium ions released during the synthesis in combination with an abundance of nitrogen and oxygen ions which originate from the precursor complexes could be the cause for rod formation. The effects of a 50% decrease in concentration of Bi, Se and both Bi & Se are shown in Figure 4.1. One does need to consider the subsequent decrease in supersaturation which is required for the NPLs to form in the first place.

Lowering the quantity of Se does not exclude rod formation although their number is significantly reduced. This could be explained by the fact that the Se precursor used in the reaction contains no nitrogen and relatively less oxygen in comparison to the Bi precursor and thus does not deplete the rod building blocks as much. Reducing the Bi concentration does appear to prevent rod formation although it negatively affects the hexagonal nature of the NPLs that is indicative of high crystallinity,

as well as seemingly introducing some roughness on the surface and along its edges that could negatively impact the performance of the surface/edge states.

When the concentration of both Bi & Se is reduced to keep a stoichiometric concentration, the rod population vanishes equivalently to the reduced Bi synthesis. Curiously, a new population of dumbbell-like nanostructures with high contrast also emerges. The elemental composition of these complexes is unknown although a high Bi ratio can be predicted due to their vast observed contrast. The NPLs do seem to better preserve their hexagonal character but a more significant aggregation is observed as well. All in all, despite the successful obstruction of rods in some samples, new complications such as decreased quality of NPLs seem to arise with all attempted variations in precursor concentrations and thus this parameter was not further investigated.

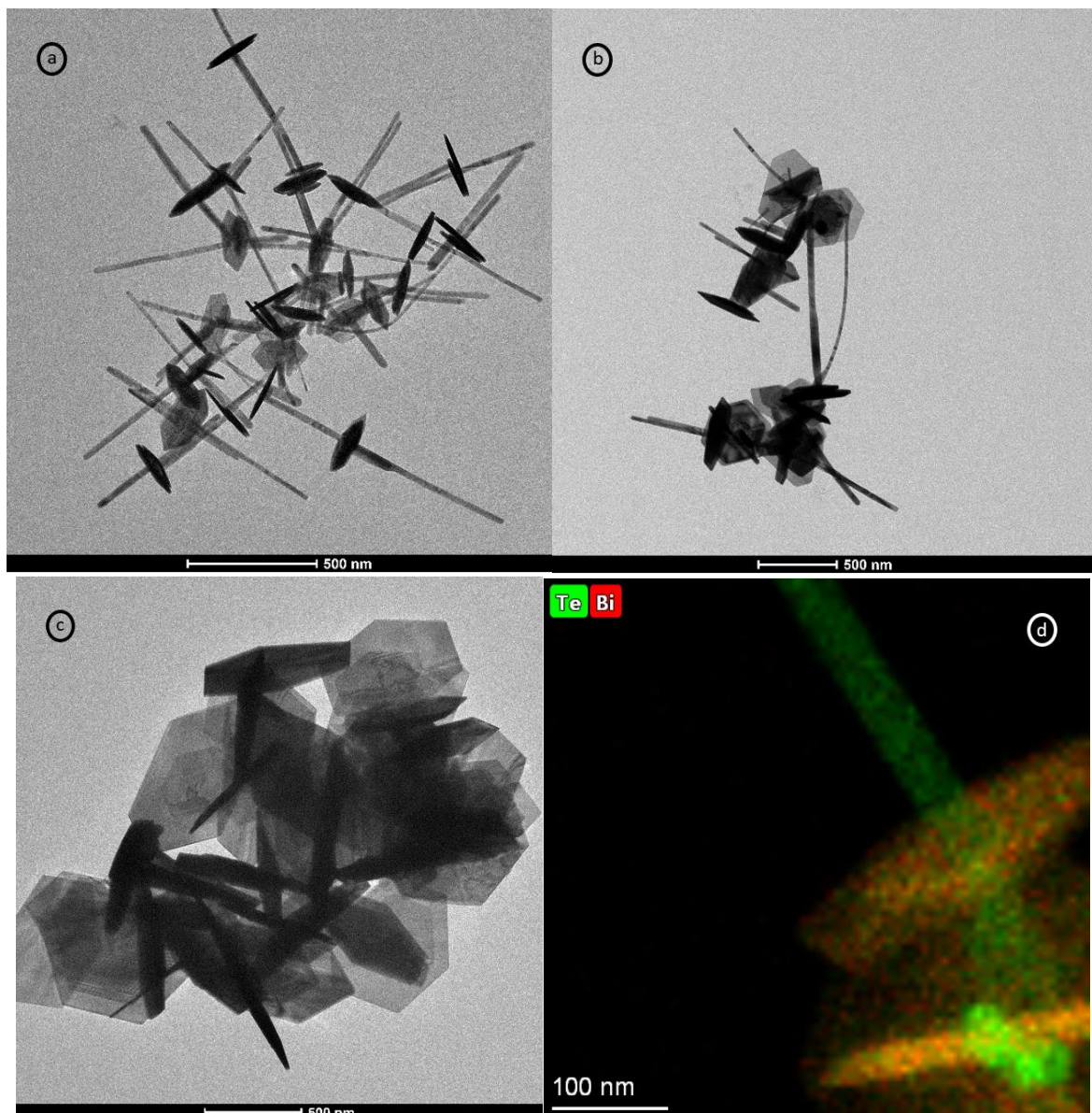***Figure 4.2:*** *a,b,c) Representative TEM images of Bi$_2$Te$_3$ NPLs obtained by [55] after 0, 20 & 120 minutes of reaction time respectively, d) An EDX elemental distribution map of NPLs attached to a nanowires. Green dots represent Te signal & Red dots represent Bi signal.*

To verify if the challenge of reproducing the synthesis specifically had to do with Bi_2Se_3 NPLs, an attempt was made to produce Bi_2Te_3 NPLs according to [55]. Figure 4.2a-c show representative TEM images of the synthesis at different points in time (0, 20 & 120 min). The first observation is that large NPLs (500-1000nm) have been formed, however they are attached to nanowires. These wires seem to disappear over time and are no longer observed at 120 min, leaving behind heavily aggregated clusters of NPLs. The nanowires are theorized to consist of Te, as these have been priorly reported to form during Bi_2Te_3 NPL synthesis [55]. This is verified by EDX mapping, as shown in Figure 4.2d, where one can clearly see a mixed Bi (red) & Te (green) signal in the NPLs while only a Te signal is present in the wires. The high level of aggregation is attributed to these wires as they appear to form clusters easily and thus drive the NPLs to flocculate even after the wires have dematerialized. Although the synthesis of Bi_2Te_3 was slightly more successful than its Bi_2Se_3 counterpart, it was still inferior to previously published results.

4.1.2 Bi_2Se_3 NPL synthesis by hot injection of Wei et al.

As the polyol reflux procedure seemed more arduous to reproduce than initially expected, an attempt was made to broaden the horizon of possible approaches. As discussed in Theory section 2.2.1, another commonly employed technique to obtain nanostructures from a colloidal synthesis method is hot injection. However, this method is rarely encountered when creating Bi_2Se_3 NPLs, possibly due to the success of the polyol procedure. One publication by Wei 2013 et al. [14] showed promising results using a facile hot injection synthesis with readily available chemicals, as they claimed to be capable of controlling the NPL thickness which would be very valuable for eventual characterization of their topological features. Some problems with the protocol remain, as aggregation and morphological irregularities become more prevalent at decreasing NPL thickness.
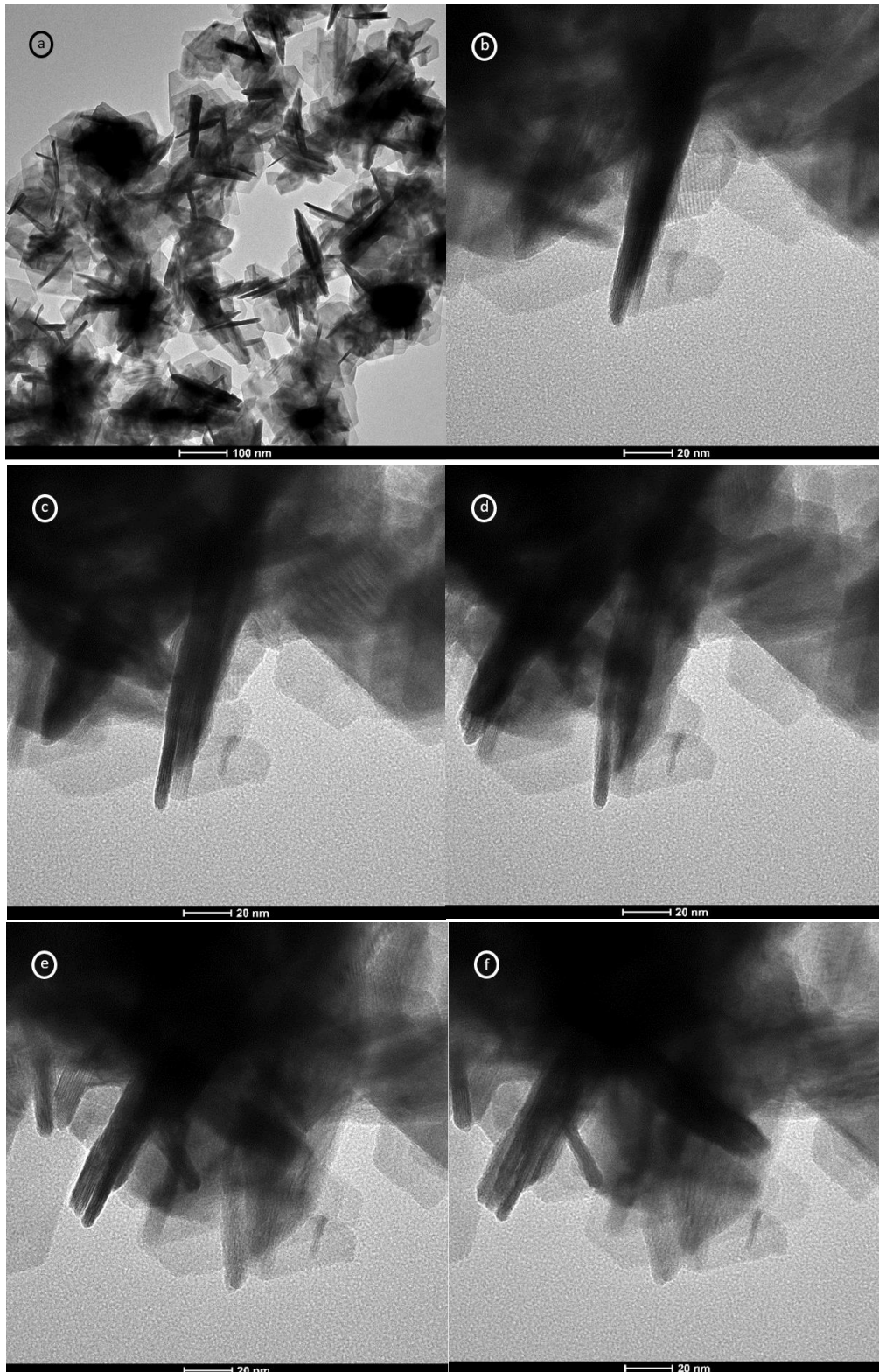
Figure 4.3: *a) Representative TEM image of Bi$_2$Se$_3$ NPLs obtained by [14], b-f) Successive zoomed in TEM images of sample a tilted at 0, 5, 10, 15 & 20° respectively.*

Figure 4.3a shows a representative TEM image of the reproduction of Wei 2013 et al. NPLs with a diameter around 100 nm appear to be successfully formed, although they are highly aggregated. Initially the nature of the dark elongated shapes was undetermined as they could be either more rod-like nanostructures, or vertically stacked NPLs. EDX measurements revealed a 2:3 ratio of Bi & Se

corresponding to Bi_2Se_3 in both populations which alluded to the stacking theory. To confirm this, a series of tilted TEM measurements were performed, shown in Figure 4.3b-f. A clear transition from a side view to a skewed NPL can be observed in this series of images which verifies that only NPLs are present in the images. This allows for a rough estimate to be made on the thickness of the NPLs using TEM images (5-10 nm), while normally SPM techniques would be required.

Although the dimensions of the formed NPLs are in the proper range, the level of aggregation is still significantly too high for STM characterization as horizontally settled individual NPLs are required for proper imaging. Clustering also hinders the ability to accurately judge the quality of the NPLs with respect to a uniform size and shape distribution. Therefore, a way to either prevent flocculation or separate the NPLs formation is needed. As the cause for the aggregation is not exactly known and could depend on a variety of factors, several approaches were investigated to hinder the formation of NPL clusters. A possibility that has not been mentioned thus far is that the clusters are not merely held together by forces between the individual NPLs and their surfactants but have fused together to form a cohesive nanostructure, in which case their separation might prove a strenuous endeavour.

Similarly, to a previous reduction of Bi & Se concentration in the polyol reflux method, a decrease of 50% was chosen. The resulting NPLs as shown in Figure 4.3a do not indicate a lower level of aggregation. On the contrary, one could argue that the NPLs display higher levels of aggregation as fewer NPLs can be clearly distinguished from the observed agglomeration, however this is difficult to conclude just from TEM analysis.

Performing the reaction for a shorter duration by taking aliquots at regular intervals would ideally provide information about the NPL growth kinetics, as well as the possibility of obtaining NPLs before they had the time to fuse together. Figure 4.3b,c present the results obtained by reducing the reaction time from 60 to 30 seconds & 10 minutes respectively. The NPLs are seen to form quickly as right after Bi injection they are already observed in the TEM image, albeit exhibiting smaller vertical/lateral dimensions (around 3-8 & 50 nm respectively) and a less consistent morphology. This indicates NPLs exhibit a rapid spontaneous formation while slowly growing into a defined shape afterwards, which is in accordance with classical nucleation theory. After continuing the reaction for 10 minutes the NPLs have grown to their full size but their hexagonal shape is still less pronounced when compared to the 60-minute synthesis. The NPLs are already clustered after 30 seconds of reaction time, suggesting that the flocculation is either a rapid process with similar kinetic rate as the nucleation step or that it happens in succession of the synthesis during cooling or washing steps.

In an effort to prevent clusters from forming right after nucleation has occurred, PVP was added to the reaction solution as a surfactant for it has been shown to stabilize the initially formed nuclei which also directs morphology of the NPLs towards more anisotropic and hexagonal shape [41]. However, no significant improvement can be observed in the obtained NPLs shown in Figure 4.3d with respect to the level of clustering and the uniformity in shape. The NPLs do exhibit a narrower thickness profile similar to the 30 second sample discussed before, which is expected from the promotion of anisotropic growth.
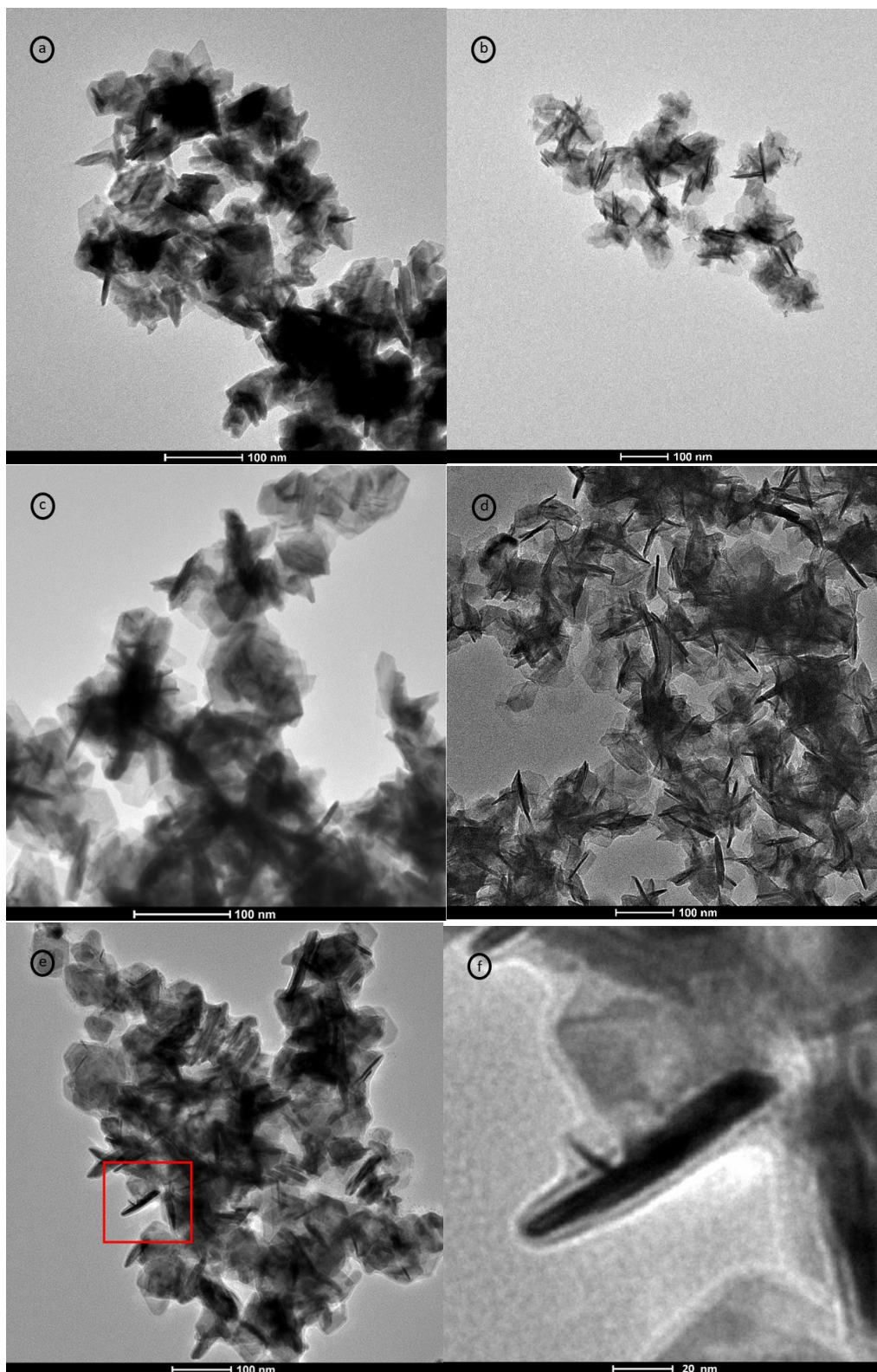
Figure 4.3: Representative TEM images of Bi_2Se_3 NPLs obtained by [14] while varying reaction parameters. a) A 50% reduction of Se & Bi, b) 30-second reaction time, c) 10-minute reaction time, d) Added PVP to reaction solvent, e) Added OLAM & OA after washing, f) Enhanced image of the red rectangle in e).

The final approach was to separate the NPLs post-synthesis either by introducing additional ligands into the sample after washing or by performing a ligand exchange procedure. The idea is that flocculation might occur due to an inability of the existing ligands to fully stabilize the NPLs in solution, either due to excessive removal of ligands from the NPL surface after washing or by entanglement of the extended ligand carbon chains. A 5% volume addition of ligands (OLAM, OA or both) was added. The best performing sample based on observed dispersibility (OLAM+OA) was then imaged using TEM (Figure 4.3e,f). It is immediately apparent from the image that no improvement in the fragmentation of clusters was achieved. One interesting detail is that a low intensity layer which formed around the NPLs can be seen in the enhanced TEM image. This is assumed to be a layer of accumulated ligands that indicates adhesion to NPL surface was successful but did not conclude in cluster separation.

The performed ligand exchange is based on Nag 2011 et al [13] which employs small charged inorganic ligands that provide electrostatic stabilization instead of more bulky traditional organic ligands with polar and non-polar components. Due to their decreased size and high electrostatic repulsion, clustering due to the aggregation of ligands becomes unlikely. However, it is unclear if the charged ions reported in the publication could properly exchange the ligands present on the NPL surface since, as far as we known, no such attempts on the Bi_2Se_3 system have been priorly investigated. Sadly, no proper results from the exchange procedure can be presented as the NPLs would not transfer to a polar medium therefore concluding the charged ions were unable to fully replace the existing ligands on the NPL surface. It might be constructive to retry this protocol using a new batch of chemicals, as the ones used were of dubious quality due to their age.

As none of the attempted strategies seem to have improved the number of free NPLs present in the solution, some of which even appeared counterproductive, it was not deemed a fruitful endeavour to further the investigation with this synthesis.

4.1.3 Bi_2Se_3 & Bi_2Te_3 NPL synthesis by a modified Polyol hot injection protocol

As the hot injection procedure did appear to yield NPLs with a decreased size in comparison to the polyol reflux method, which was attributed to a narrower nucleation window, an attempt was made to combine the best of both worlds by converting the polyol reflux from a heating-up into a hot injection protocol. The transformation of the procedure was simple in practice (See experimental methods 3.2.2 for details), as the only initial difference was the removal of the Bi precursor and a small amount of solvent from the reaction medium. This dissolved & preheated precursor was subsequently injected in the reaction medium once it reached 190°C. Despite the relatively minor change in methodology, the resulting NPLs are of significantly higher quality and were extensively analysed with (HAADF-S)TEM, ED, EDX, AFM, XRD & UV-vis spectroscopy.
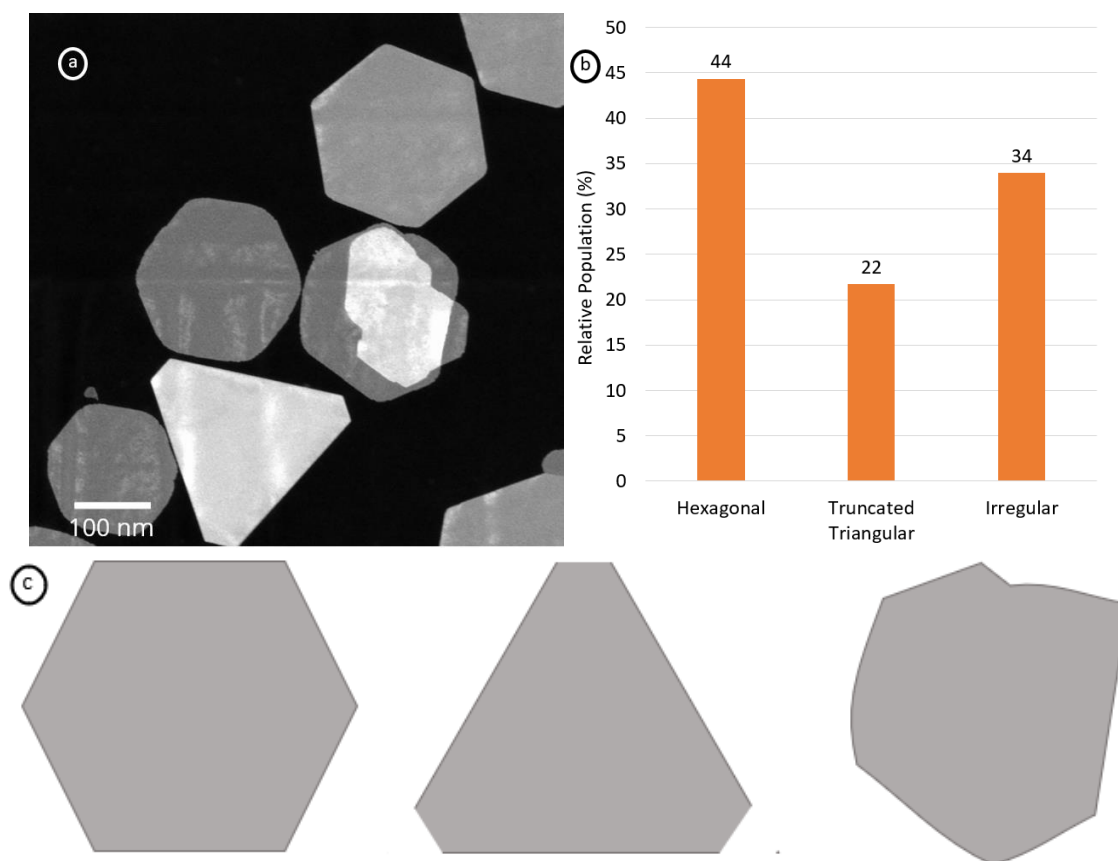
Figure 4.4: *a) Representative HAADF-STEM image of Bi$_2$Se$_3$ NPLs obtained by a modified polyol hot injection synthesis, b) A graph showing the relative population distribution of NPLs observed in sample a), c) A graphic representation of the characterization between the 3 NPL populations that are distinguished in b).*

From studying (HAADF-S)TEM images (such as Figure 4.4a) it is apparent that the synthesized NPLs are relatively homogeneous in thickness within the platelet due to their uniform intensity, although a significant absolute thickness distribution exists between NPLs, which is investigated further using AFM. A general judgement on the lateral size is more complex as several different morphologies are encountered, but features are generally in the size range of 100-300 nm with significant size distribution between NPLs and samples due to unidentified reasons. Three main NPLs shapes can be distinguished (Hexagonal, Truncated Triangular & Irregular), of which a schematic representation is shown in Figure 4.4c. Here, irregular is defined as a catch all category where NPLs that do not fit in the other categories are placed. It is relevant to point out that the boundary between morphologies is not absolute and that human judgement was used to differentiate between them.

A relative population distribution shown in Figure 4.4b obtained by examining around 2000 NPLs highlights that all shapes occupy a significant portion of the population with Hexagonal prevailing at 44%, followed by Irregular at 34% and finally Truncated Triangular at 22%. This ratio is also relatively constant between samples. The original goal was to obtain NPLs of the hexagonal variety and thus it is beneficial that they are the most common population. However, all 3 shapes could be of interest for future STM experiments to investigate the effects of morphology on the localized surface and edge states and therefore no large effort is made to obtain a more homogeneous shape distribution.
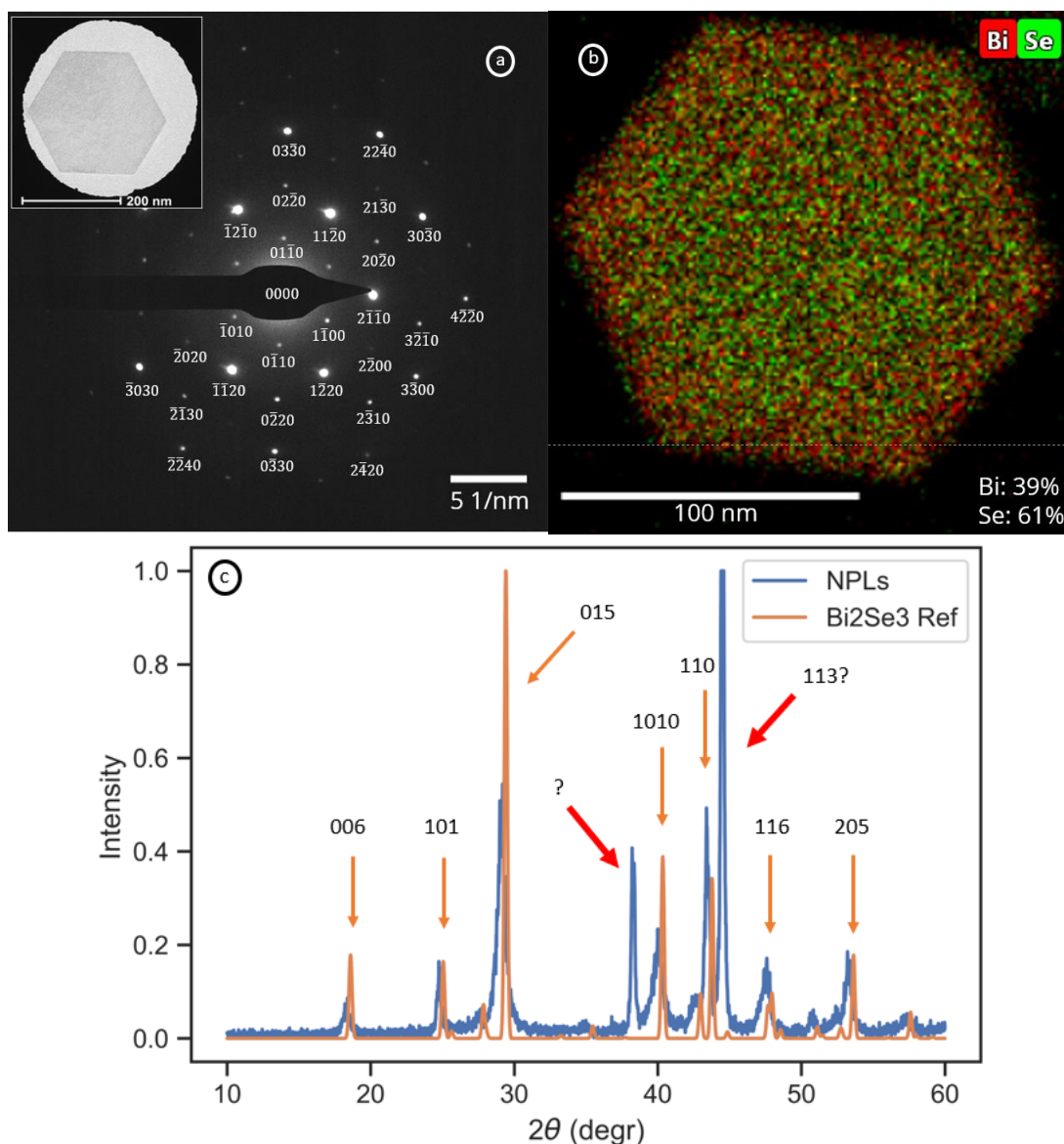
Figure 4.5: *a) A representative ED diffractogram of a Bi₂Se₃ NPL with identified Miller-Bravais indices using CrystTbox [99], b) A representative EDX elemental distribution map of a Bi₂Se₃ NPL with shown Bi and Se ratios. Green dots represent Se signal & Red dots represent Bi signal, c) Blue: A representative powder XRD spectrum of dried Bi₂Se₃ NPLs. Orange: A reference XRD spectrum of Bi₂Se₃ from the ICSD [101]. Identified reflections are marked with orange arrows and their corresponding reflection, while unidentified reflections are marked with red arrows.*

To determine the crystallographic quality and identify any local irregularities within the crystal structure of the NPLs, ED spectra such as the one in Figure 4.5a were recorded and analysed using CrysTBox [99]. The resulting diffraction pattern represents a highly ordered six-fold [0001] symmetry which is in accordance with literature [24]. However, a constant deviation (≈15%) from theoretical values is observed in the absolute spot positions leading to a decreased d-spacing (0.285nm). It was suspected that a calibration error factor might be involved, thus a known diffraction pattern on AuPb was cross referenced to theoretical values which resulted in a error of ≈ 7%. Thus when corrected for calibration, this halves the observed deviation but does not fully account for all of it. The residual shift could be related to some form of lattice train imposed by the confined nature of the nanostructure, although this seems unlikely due to relatively large lateral size of the NPL. A high

concentration of defects or dopants could also explain the variance in crystal lattice parameters. To verify this, the sample was investigated by XRD, EDX mapping & high resolution HAADF-STEM.

Initially a drop casting procedure was used for XRD measurements as less sample was needed and no damage to the NPLs would occur during preparation, but this yielded unsatisfactory signal to distinguish most peaks. Thus a drying procedure (100°C for 4 hours) was implemented to enhance the signal. The normalized powder XRD diffraction pattern of dried NPLs is shown in Figure 4.5c. The first feature that stands out is that the peak positions in the diffractogram are in relatively good agreement with the reference values except for a slight shift to lower angles, which would indicate a small increase in crystallographic d-spacing. This is contradictory to the slightly reduced d-spacing obtained from ED. However, as the peak shift is only minor this could be attributed to an experimental error. It is also vital to keep in mind that XRD only gives information on the average over the whole sample, thus local differences between NPLs cannot be considered.

Another distinction between the 2 diffraction patterns is their relative peak intensities, which is a commonly encountered feature when studying nanostructures using XRD [85]. These often originate from an orientational preference of the nanocrystals when deposited on a surface, such that some reflections are enhanced while others are diminished. Lastly, a curious observation is the existence of 2 peaks that do not appear as such in the reference spectrum at 39 and 45 degrees. The latter of which could match a miniscule peak from the reference (113 reflection), although such a significant difference in peak intensity would be unlikely even when a preferred orientation is considered. Initially the peaks were thought to originate from either a reflection of the sample holder (Si) or a different crystalline material present in the sample, however no reference patterns of Si or any of the possible other crystalline products (Bi, Se, Bi_2O_3, SeO_2 or Bi_xSe_y) match with the observed reflections. It is possible that some residual sample from a previous measurement was present and is to blame for the unassigned reflections. To verify this the measurement would need to be repeated. Overall, the XRD data provides further evidence that Bi_2Se_3 of good crystalline quality was indeed synthesized, but contradict the decrease in crystal lattice parameters observed in ED.

EDX was performed on the NPLs to further investigate their elemental composition and any irregularities therein that may elucidate the observations made by ED and XRD. EDX can be a useful tool in determining ratio's between known elements present in the structure, although the exact percentages provided are not always accurate as some elements cannot be fully distinguished due to overlapping characteristic x-ray energies and thus some impurities can go unnoticed. EDX mapping can provide a good overview on the main trends in elemental distribution throughout nanostructures. Figure 4.5b shows such an element map of a NPL with a near stoichiometric ratio of $Bi_{1.95}Se_{3.05}$. Curiously literature suggests that Se vacancies are the most common defect in the Bi_2Se_3 system [103] from which a slightly lower than stoichiometric Se concentration is expected, while we observe a slightly higher concentration. The reason for this is unknown, as any major discrepancies in the crystal lattice should be observed in the ED diffractogram.
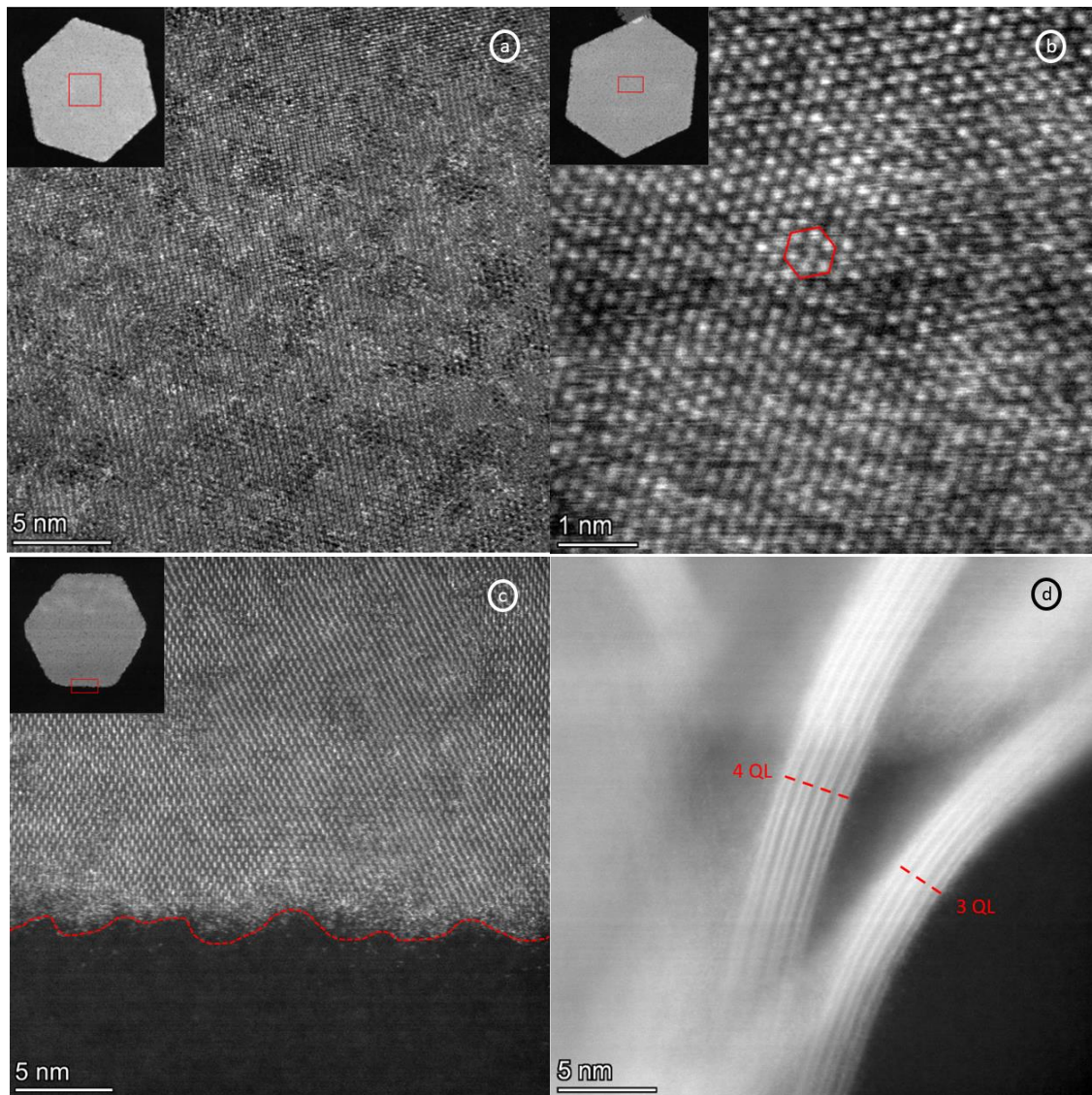
Figure 4.6: *Representative high-resolution HAADF-STEM images of Bi$_2$Se$_3$ NPLs. The highlighted red areas in the top left overview images signify the area of the NPL under observation. a) An overview of the crystallographic structure of an NPL from the top, b) An enhanced image of the local crystallographic order of the NPL. The hexagonal lattice symmetry is highlighted in red, c) An image of the edge of an NPL which is traced in red for clarity, d) An overview of the crystallographic structure of an NPL from the side. Individually distinguished QLs are marked in red.*

The high resolution HAADF-STEM measurements yielded several noteworthy observations which are represented in Figures 4.6a-d. Firstly, the NPL surface seems to consist of areas which display high crystallinity that are patched together (Figure 4.6a). This is in agreement with an epitaxial growth model. Within these regions a hexagonal lattice symmetry along the [110] zone axis with an atom spacing of 0.22 nm is observed as shown in Figure 4.6b [24]. Although the NPLs seem to have sharp borders from a distance, closer inspection highlights significant inhomogeneities (1-2 nm ≈ 5-10 atoms) at the edge of an NPL (Figure 4.6c). This could also be a consequence of the oriented attachment mechanism as new nuclei are assumed to adsorb on the extremities in the lateral direction. It would be interesting to investigate the effect of these rough features on the topological edge states, although it would be preferential to obtain NPLs with a more distinct boundary for comparison. Within vertically oriented NPLs, individual QLs with an expected thickness of ≈ 1 nm can

be distinguished (Figure 4.6d). NPLs with a height of 3 & 4 QLs were encountered, although only a few of these NPLs were observed so no statistically relevant judgement on their height distribution can be made this way. Fortunately, another technique is readily available for this purpose.
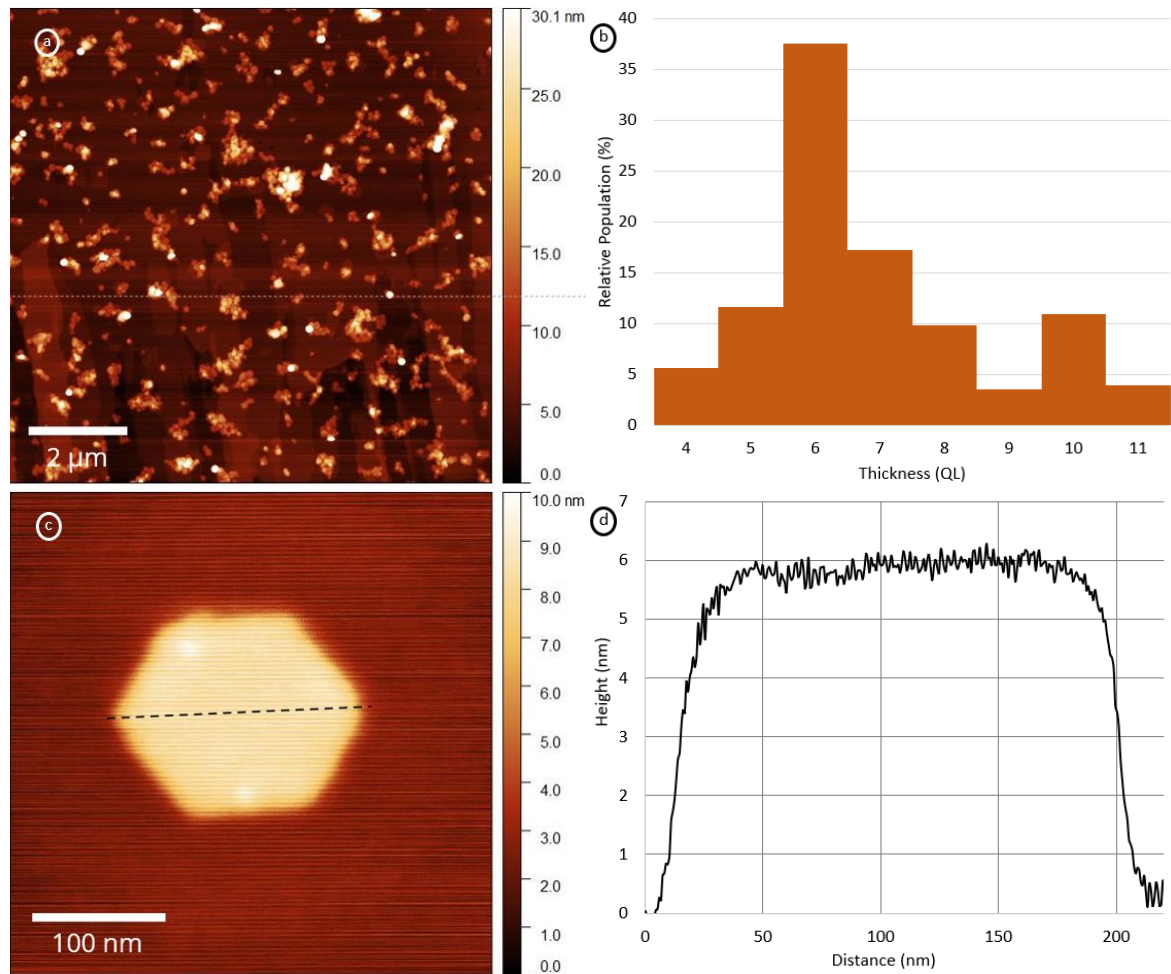
Figure 4.7: *a) A representative AFM topographic overview (10x10μm) of clustered and free Bi$_2$Se$_3$ NPLs analysed with Gwyddion [100], b) A graph showing the height population distribution of NPLs (N=2000), c) A representative AFM topographic image (350x350nm) of a single NPL, d) A graph of the height profile scan of the dashed black line in c).*

AFM experiments were performed to quantifiably investigate the thickness of the NPLs. This is important as the topological surface states have been shown to be strongly dependent on the amount of QL's present in the vertical direction [7]. Figure 4.7a shows an overview topographic image of NPLs distributed over the surface, either as single NPLs or aggregated in small clusters. These so-called "free NPLs" are favourable as they allow for more facile and accurate height data acquisition in comparison to clusters which have many overlapping NPLs that can be troublesome to correctly interpret.

As the sample preparation process of AFM is similar to STM, some effort was made to optimize the drop casting procedure as described in the experimental methods. Here the quantity of free NPLs per area and the number & height of clusters were the principal metrics to judge the quality of the procedure. Unfortunately, the process exhibits a low reproducibility probably due to the high possibility of human error in drop-casting and samples with little to no free NPLs can be regularly encountered. This is especially disadvantageous for STM where sample insertion and investigation

are a laborious endeavour. Thus far no method has been established which constantly produces satisfactory results and it might be worthwhile to further look into a solution for this problem. It was also verified that the NPLs could withstand deformation under STM annealing conditions by heating samples ex-situ to 150°C before AFM measurement.

When a sample of acceptable quality is produced, topographic NPL characterization is a feasible process. Figure 4.7b provides a graphic representation made by Gwyddion [23] of a typical NPL thickness population and their relative abundances based on 570 individual height profiles. The height range is between 4 and 11 QL which is similar to priorly published results [1,5] with 6 nm as the dominant species. As Bi_2Se_3 has a QL unit cell with a vertical size of around 1 nm, NPLs can be distinguished in size categories per QL as no thicknesses in between are encountered. Curiously, two different population probability curves can be distinguished as a majority of the NPLs are statistically distributed around 6 nm but a minor second population can be observed with a local maximum of 10 nm. Fortunately, a distribution in thickness is not an inherent problem in this study as it opens the possibility to investigate the influence of thickness on the edge/surface states using only a single sample. However, it does make obtaining statistically relevant results on NPLs with a similar height more labour intensive as the STM has a significantly lower search area. It would be beneficial to obtain NPLs with a thickness of 1-3 QLs to be able to investigate the full NPL height range from 1-11 QLs.

Besides the height difference between NPLs, AFM can also be used to investigate the height fluctuations within NPLs. Figures 4.7c,d represent a high magnification topograph of a typical free NPL and its height profile. It shows a mostly homogeneously flat surface, with the fluctuations of the line profile staying within the range of 1 QL. Some irregularities on the surface can occasionally be observed, as is the case in this image with 2 protruding spots of around 1 nm in height. It is unknown if these deformities are present in solution or if they form during sample preparation, although similar features are observed in EM images. As a majority of free NPLs display homogeneous surfaces, this is not deemed a significant issue.
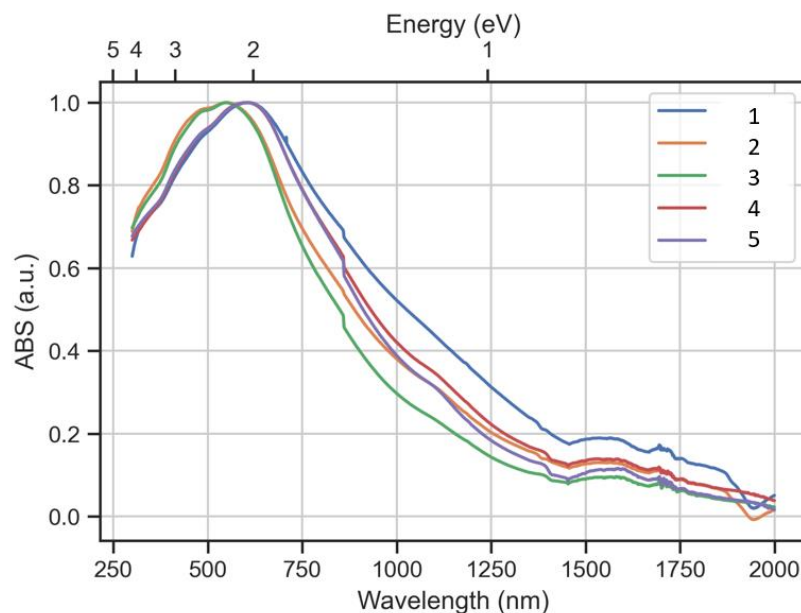
Figure 4.8: *Normalized representative UV-VIS spectra of 5 equivalently synthesized NPL samples from 300-2000nm.*

Finally, UV-VIS was used as another method to assess the uniformity between samples as NPLs with similar morphology will have equivalent absorption features. Figure 4.8 shows the absorption spectrum of 5 samples with analogous synthesis procedures, however some differences between them exist. Curiously, the samples can be split in two distinct groups according to their maximum absorption peak position at 550 & 600 nm respectively which suggest that the NPLs tend to two populations. However, this is not observed in the size distributions observed in TEM and AFM, so it is unclear what quality defines these two populations in UV-VIS. Overall, both TEM & UV-VIS results suggest the reproducibility of the synthesis is low. This is not wholly unexpected, as it is an often-encountered challenge of colloidal synthesis, but it does show that more careful control over reaction parameters is needed during synthesis which will be discussed in the next subchapter.
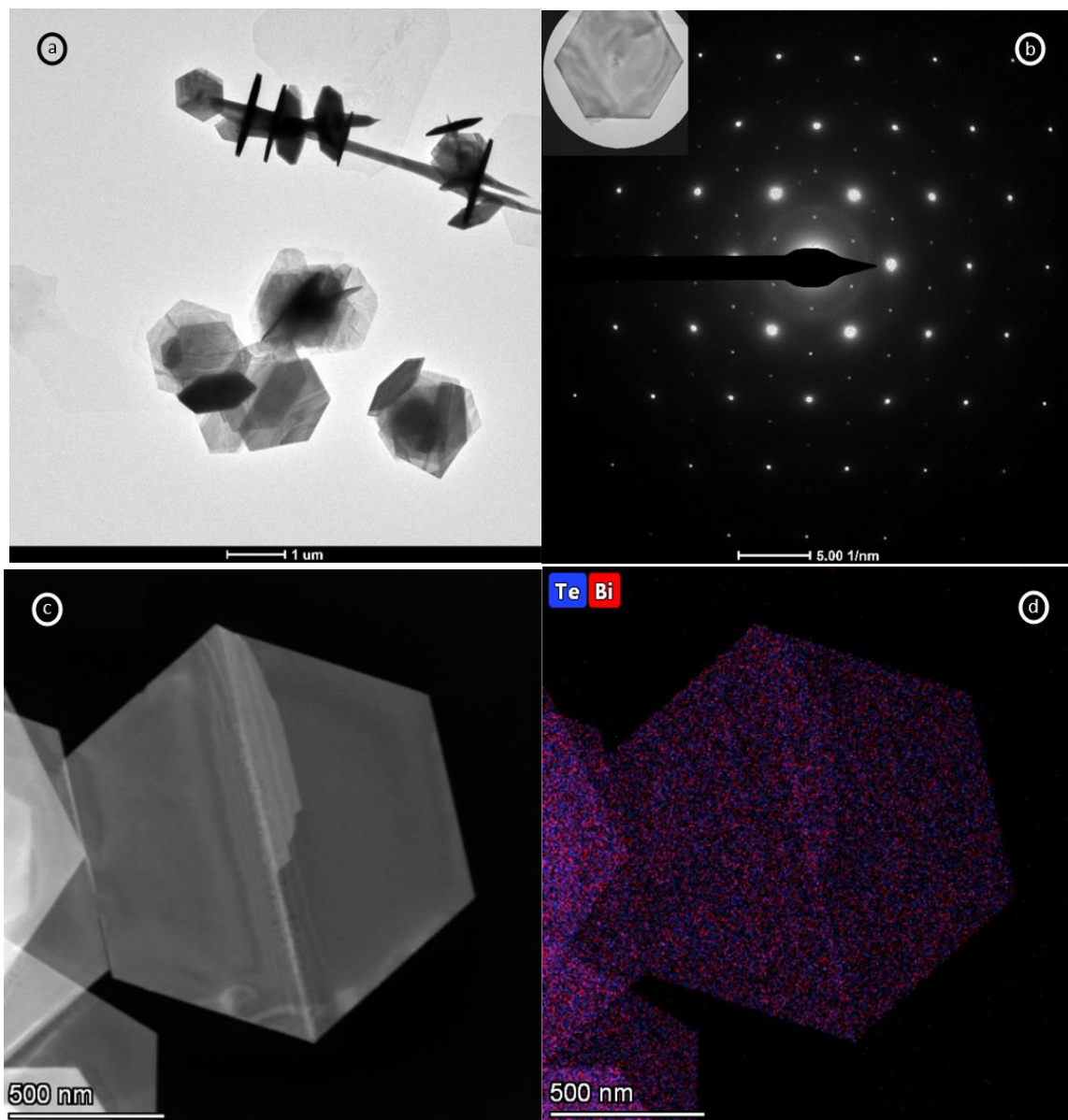
Figure 4.9: Representative results of Bi$_2$Te$_3$ NPLs obtained by polyol hot injection synthesis. a) A TEM image of NPLs clustered and attached to Te wires, b) An ED diffractogram, c) A HAADF-STEM image, d) An EDX map of c). Blue dots represent Te signal & Red dots represent Bi signal.

Due to the success of the polyol hot injection procedure in acquiring high quality Bi$_2$Se$_3$ NPLs, a similar procedure was carried out for Bi$_2$Te$_3$. The EM results are shown in Figure 4.9a,c. Similar to the

polyol reflux synthesis, a mix of NPLs attached to Te wires and clusters of large NPLs (500-1000nm) are obtained. However, unlike the previous Bi_2Te_3 sample some free NPLs are present as well which improves the quality of the sample with respect to their characterizability. NPLs do appear less regularly defined in shape as inhomogeneities in the form of wrinkles or high contrast lines are observed in most NPLs, as shown in Figure 4.9c. AFM analysis provides a significantly increased thickness in comparison to Bi_2Se_3 NPLs of around 20 nm, with considerable irregularities of 5-10 nm in height throughout NPLs.

To verify the crystalline quality and homogeneous distribution of elements in spite of these defects, NPLs were analysed using ED and EDX mapping as shown in Figure 4.9b,d. The diffractogram displays a hexagonal lattice symmetry similar to Bi_2Se_3 NPLs as shown in Figure 4.5a. However, at low 1/nm values rings are observed in addition to the expected diffraction spots indicating a low level of polycrystallinity at long distances which could be caused by the observed inhomogeneities. The EDX map confirms a stoichiometric distribution of elements throughout the NPL with an increased intensity at locations of high contrast, however the dispersal of atoms seems to retain stoichiometric ratios in these areas although this is difficult to conclude with certainty as the EDX resolution is not sufficient in these measurements. All in all, Bi_2Te_3 NPLs were successfully synthesized although they display a drop in quality in comparison to obtained Bi_2Se_3 NPLs with respect to crystalline structure and well defined morphology. Therefore, it was concluded that it was more worthwhile to focus on optimizing the Bi_2Se_3 NPL synthesis while keeping the possibility open to revisit Bi_2Te_3 NPLs in future research.

4.1.3.1 Variations in Bi_2Se_3 polyol hot injection procedure

The purpose of varying the parameters of this procedure is threefold. Firstly, as mentioned a more reproducible synthesis is desired and knowing which variables will strongly affect the resulting NPLs is key to achieve this. Secondly, greater control over the lateral and vertical size distribution while maintaining or improving NPL qualities such as hexagonal crystalline symmetry and well-defined edges/surfaces would be beneficial for future study of their topological characteristics as these are thought to depend highly on these features. Lastly, an improved washing procedure is preferred as a significant quantity of product is lost in the supernatant during each cycle, which limits the final concentration of the sample and the amount of washing steps that can be performed. A limited amount of clustering is still observed as well, which suggests the quality of the solvent could be improved. Unfortunately, it is not possible to rigorously investigate the whole parameter space, so some educated guesses were made on which variables would be interesting and feasible to examine.
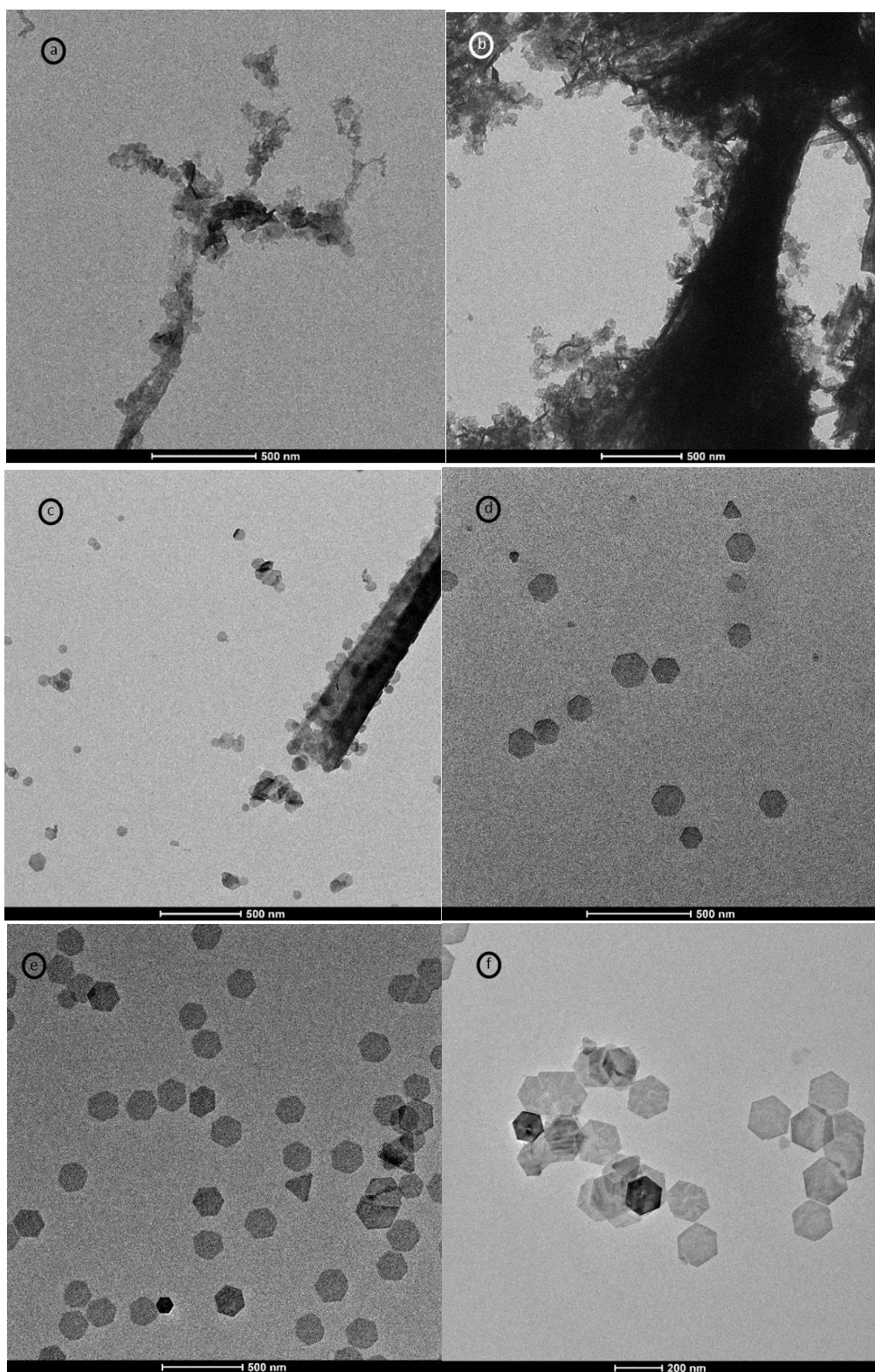
Figure 4.10: *a-f) Representative TEM images of Bi$_2$Se$_3$ NPLs obtained by polyol hot injection procedure after 0, 1, 2, 3, 10, 120 minutes of reaction time respectively.*

The first parameter variation to be considered was a reduction in reaction time, as it would leave the NPLs with less time to grow and therefore could reduce their lateral and vertical size. The time scale that was investigated focussed on the start of the synthesis right after hot injection, as an immediate colour change was observed. Figure 4.10a-f shows TEM images that highlight representative

47

snapshots of the significant moments during synthesis (0, 1, 2, 3, 10 & 120 min). It is important to note that to obtain these images, several washing steps needed to be performed which could have removed crucial information on structures present in solution. However, to rule out this possibility *in situ* studies would need to be performed which was not feasible for this project.

In the first 3 minutes after injection several interesting features are observed. Initially, only amorphous agglomerations are present but within 1 minute large, elongated dendrite-like structures have been formed. Alongside these the first signs of crude NPLs are visible. After 2 minutes these large dendrites appear to have shrunk to smaller rectangular structures and some smaller but fully shaped NPLs seem to stick to their sides, with some free NPLs also present. Curiously, 3 minutes following the injection all larger structures have disappeared and only NPLs are left, which display a broad lateral size distribution with some NPLs already displaying full-grown size. To our knowledge such large scale structures have not yet been reported for any Bi_2Se_3 NPL growth model and thus their composition and role in the formation of NPLs is currently unknown. It is possible these formations supply the elemental building blocks from which the NPLs are eventually formed, which would explain their disappearance over time. However, the reason behind their initial formation remains undetermined and requests further investigation.

Height characterization of 1–3-minute samples by AFM yields a similar distribution of QLs to previously reported results in 4.1.3, suggesting that vertical growth occurs rapidly after nucleation and quickly establishes a stable size while lateral growth into fully formed NPLs happens more slowly. Unfortunately, this indicates that thinner NPLs cannot be feasibly obtained this way. However, significantly reduced lateral sizes (≈50 nm) are definitely possible. Between 3 and 10 minutes the NPLs appear to mature slowly while narrowing the lateral size distribution. After 10 minutes NPLs are fully grown, and no clear distinction is observed with a 120-minute reaction time by AFM, UV-VIS, EDX & ED. The possibility of such a reduction in reaction time with equivalent results significantly improves the practicality of the synthesis as it allows for more expedient further variation in parameters. Therefore, a reaction time of 10 minutes was assumed for future experiments.

Figure 4.11: *Representative TEM images of Bi$_2$Se$_3$ NPLs obtained by polyol hot injection procedure at varying reaction temperatures. a,b) 165°C, c) 180°C, d) 200°C*

The second parameter under investigation is the reaction temperature (hereby denoted as T$_{react}$) as it has a considerable influence on the available energy of the individual reactants and therefore the thermodynamics and kinetics of nanocrystal formation. It is difficult to predict what influence a given change in T$_{react}$ will have so empirical study is often the most straightforward. Figure 4.11a-d show representative TEM images of syntheses performed at 165, 180 and 200°C. A strong trend of increased lateral dimensions at decreased T$_{react}$ is observed as typically sized NPLs (100-300 nm) are present at 200°C, while NPLs formed at 180°C display sizes of 600-800 nm. At 165°C the encountered structures cannot be labelled as NPLs both due to their micrometer scale dimensions and amorphous morphology. Curiously, some structures still contain hexagonal features while others have become more rectangular in nature. Raising the T$_{react}$ above 200 ^{o}C is not straightforward, as the boiling point of the solvent is reached. All in all, NPLs with a significantly increased lateral size can be obtained from a relatively minor change in T$_{react}$ and thus it is a parameter that needs to be carefully considered during future experiments.
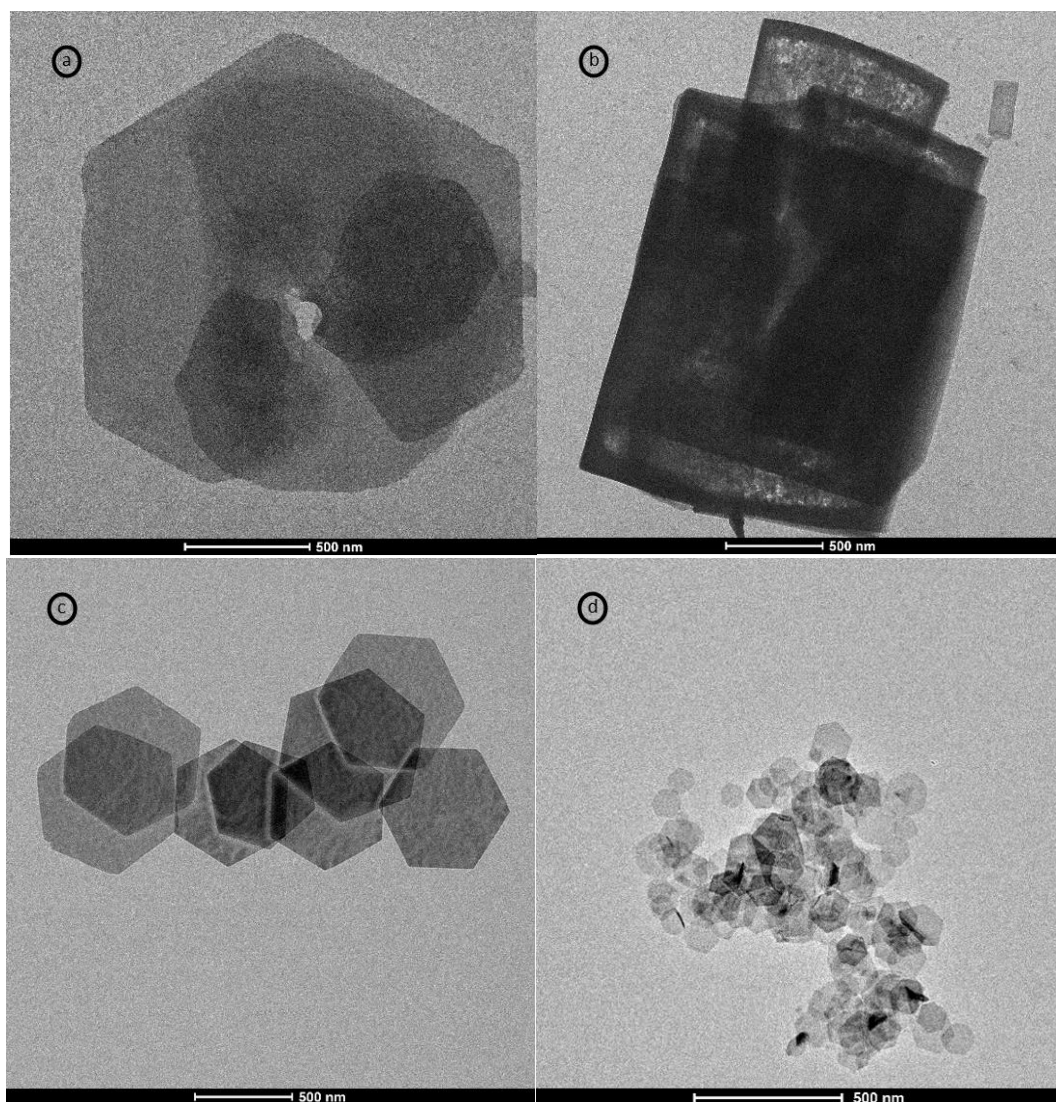
49
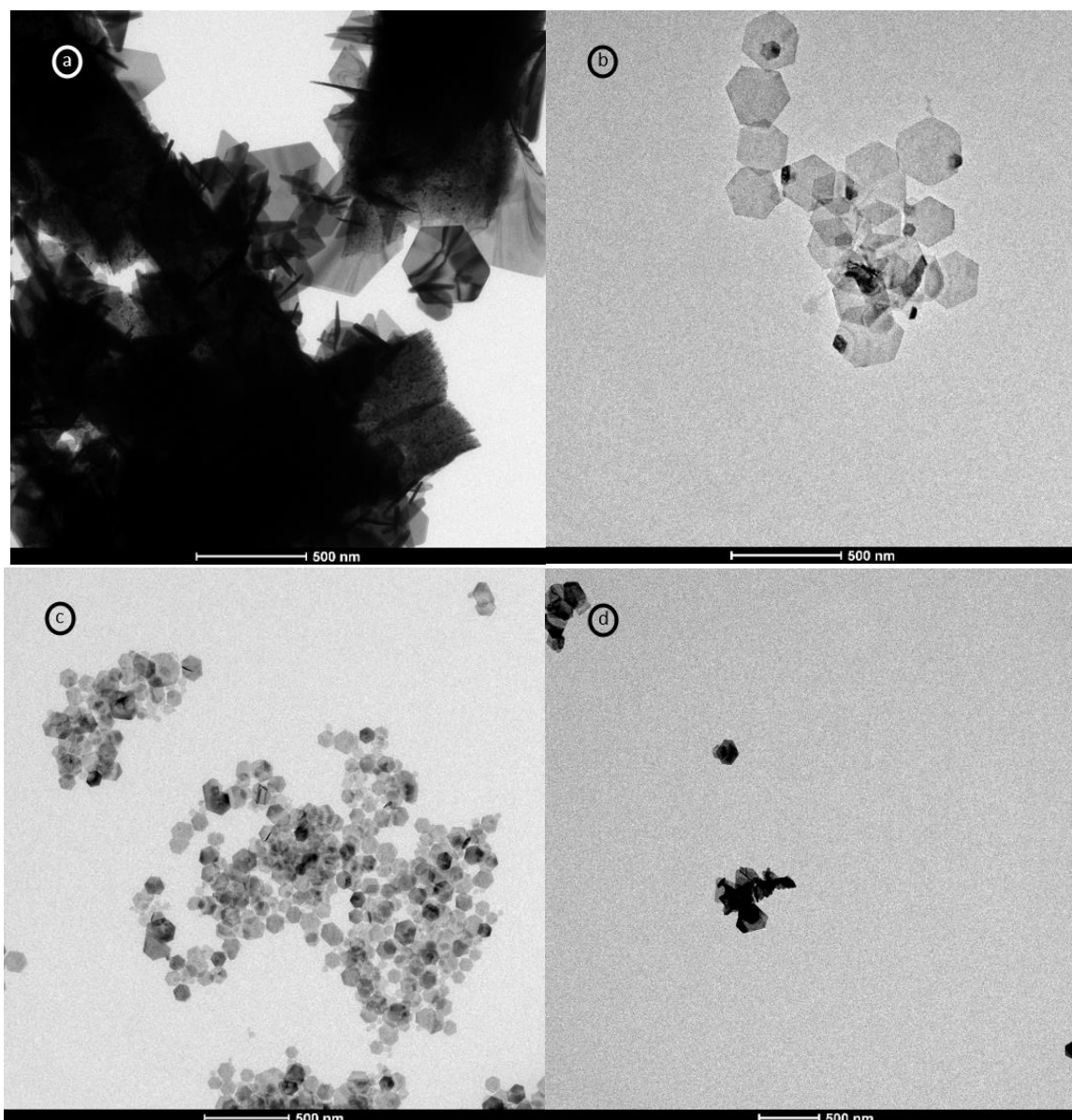
Figure 4.12: *Representative TEM images of Bi$_2$Se$_3$ NPLs obtained by polyol hot injection procedure at varying injection temperature conditions. a) <150°C, b) 150°C, c) 160°C, d) Reheated to 160°C.*

As the reaction temperature had been shown to have a crucial impact on the formed NPLs, it was decided to study the effects of the temperature of the injection solution (hereby denoted as T$_{inject}$) as well. Previously, T$_{inject}$ was not carefully monitored as a visual colour change of the Bi-precursor solution from transparent to milky white was used as a temperature indication. This change was later determined to occur between 155-160°C and is linked to the thermal degradation of BiNO. Figures 4.12a-c show representative TEM images of NPLs obtained with an T$_{inject}$ of <150, 150 & 160°C. The T$_{inject}$ of Figure 4.12a is not exactly known as no thermometer was used during this synthesis, but a T$_{inject}$ smaller than 150°C is assumed as no colour change was observed. A temperature dependence trend similar to T$_{react}$ is observed, as the NPLs seem to grow in lateral size with decreased T$_{inject}$. Likewise, large irregular structures are observed at significantly reduced T$_{inject}$. However, in this case clear NPLs can still be distinguished thus the large structures likely consist partially of vast NPL clusters. At 150°C some NPLs contain a minor area of increased contrast which usually appear at their edge. These are thought to be remnants of smaller NPLs that have epitaxially

attached to the larger structures, as a significant population of NPLs with similar size (70-90 nm) to the inhomogeneous spots are also observed. This suggests a larger window of nucleation yielding a broad size distribution which makes sense as at lower T_{inject} the precursor would be dispensed slower in solution by thermal degradation. These miniature NPLs would be interesting to investigate further as thinner NPLs could possibly be observed. Unfortunately, due to time constraints thorough examination by AFM was not possible.

The possibility of using a large batch of preheated Bi-precursor solution for multiple subsequent syntheses was also considered, as it could ensure a more consistent injection solution and would make the protocol more efficient. However, the method yielded NPLs of lesser quality due to increased flocculation and less defined shape as is shown in Figure 4.12d and was therefore not further utilized.
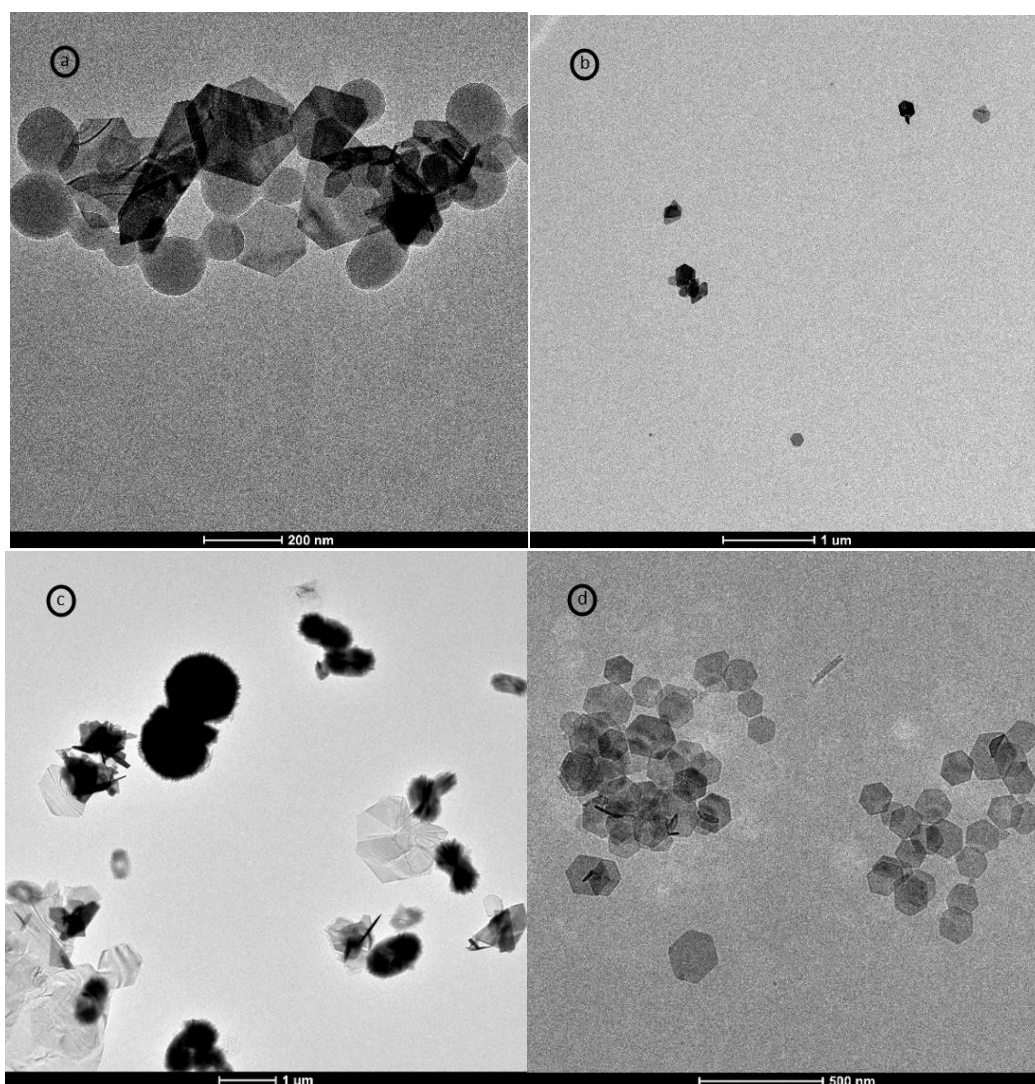
Figure 4.13: *Representative TEM images of Bi$_2$Se$_3$ NPLs obtained by polyol hot injection procedure by varying washing procedures. a) DMF as solvent, b) 1-butanol as solvent, c) Hexane as anti-solvent, d) ACN as anti-solvent.*

Variations in the washing procedure focussed on seeking superior solvents to improve dispersibility and anti-solvents to obtain a more complete yield, as the supernatant still contained a considerable concentration of NPLs. This could also be a reason for the absence of thinner NPLs in the samples, as

they could be left in the supernatant due to their increase dispersibility. It has been shown that N-methyl-2-pyrrolidone (NMP) is a competent solvent for 2D Bi_2Se_3 nanocrystals even capable of liquid exfoliation [29]. Alas this chemical was unavailable in the timeframe of this project. However, it has been shown that N-N-dimethylformamide (DMF) and 1-butanol can act as sufficient replacements due to comparable Hildebrand and dispersive Hansen solubility parameters [79]. Meanwhile, hexane is occasionally used as a precipitation agent in Bi_2Se_3 NPL synthesis [41], as is acetonitrile (ACN) [98].

The representative TEM results of samples with varied solvents are shown in Figure 4.13a,b. NPLs showed a reduced dispersibility in 1-butanol, while spherical non-crystalline structures were observed to aggregate with NPLs in the DMF sample. Consequently, both investigated solvents were deemed inferior to EtOH. Results from anti-solvent variation are shown in Figure 4.13c,d. The usage of hexane as anti-solvent led to the formation of highly aggregated NPLs in the form of nanoflowers and dumbbells. This, together with the DMF sample, shows how significant an effect the washing procedure has on the final sample. With ACN a transparent supernatant was obtained which resulted in an improved yield. As no qualitative distinction could be made between the samples washed with EtOH and ACN using the techniques described in 4.1.3, the new washing procedure with ACN was deemed superior and adopted for future syntheses. Unfortunately, low reproducibility is still an issue that plagues the procedure, and more study is needed to resolve it.

4.1.4 Summary and Outlook.

The focus of this chapter was to optimize a synthesis protocol that could obtain high quality Bi_2Se_3 NPLs which are suitable for STM studies as well as tuning the parameters of the procedure to control the lateral and vertical dimensions of the acquired NPLs. After attempts to reproduce several syntheses found in literature were unsuccessful, a slightly modified protocol was developed which finally yielded NPLs of satisfactory quality as determined by HRHAADF-S(TEM), ED, EDX, AFM, XRD, UV-VIS. The process of preparing the NPLs for proper STM characterization is discussed in the following chapter.

Subsequently, the effects of several important parameters were investigated which concluded in an improved procedure with increased efficiency due to decreased reaction time and greater total yield due to a refined washing procedure. Furthermore, NPL lateral size control was demonstrated by variations in reaction and injection temperature. Unfortunately, we were unable to regulate NPL thickness in a similar way as vertical growth was observed to occur rapidly after injection. It would be worthwhile to further investigate this behaviour to discover a method to obtain these thinner NPLs, possibly by addition of a surfactant which can effectively supress vertical growth. However, the major challenge concerning the procedure is its low reproducibility as syntheses still display a relatively large variation in lateral size (100-300 nm) and level of aggregation as observed in TEM, AFM & UV-VIS. The reason for this is unclear but it is thought that inadequate control over reaction parameters which strongly affect these characteristics such as reaction and injection temperature are to blame. Alternatively, it could also be caused by a variable which has not yet been thoroughly investigated. Heating rate, injection rate and injection volume are a few examples of such parameters.

There are some unknowns presented in this chapter which could be worthwhile to study further as well as the possibility of conducting additional research using the knowledge gained in this chapter as a basis. In addition to the previously mentioned parameters that could elicit further study, it would also be interesting to examine the effects of varying multiple parameters simultaneously. For

example, by taking aliquots of samples at varying reaction and injection temperatures the growth mechanism of NPLs could be examined in more detail. It could also be worthwhile to investigate the distinction between NPLs of different morphologies such as truncated triagonal in more detail to see if any differences between their crystal structure could be observed using ED and XRD. Furthermore, valuable information could be gained by examining the roughness of the edge observed in HRHAADF-STEM at varying reaction parameters to verify if a more defined NPL boundary can be obtained this way. Bi_2Te_3 NPL synthesis optimization could be considered a fruitful endeavour as well, especially now that direct comparisons can be made to the Bi_2Se_3 system. Finally, it would be interesting to explore the possibility of using the NPLs as a basis for designing heterostructured NPLs either by constructing layered core-crown structures or by doping with various elements to create new materials with unknown properties.

4.2 Ligand treatment of NPLs for STM preparation

As Bi_2Se_3 NPLs of adequate quality can be readily produced by the developed polyol hot injection procedure, a first attempt was made to transfer them into the STM to perform high resolution topographic measurements. The results of these initial ventures are displayed in Figure 4.14a,b where 4.14a shows a representative overview image and 4.14b shows an enhanced image of what is presumed a NPL.
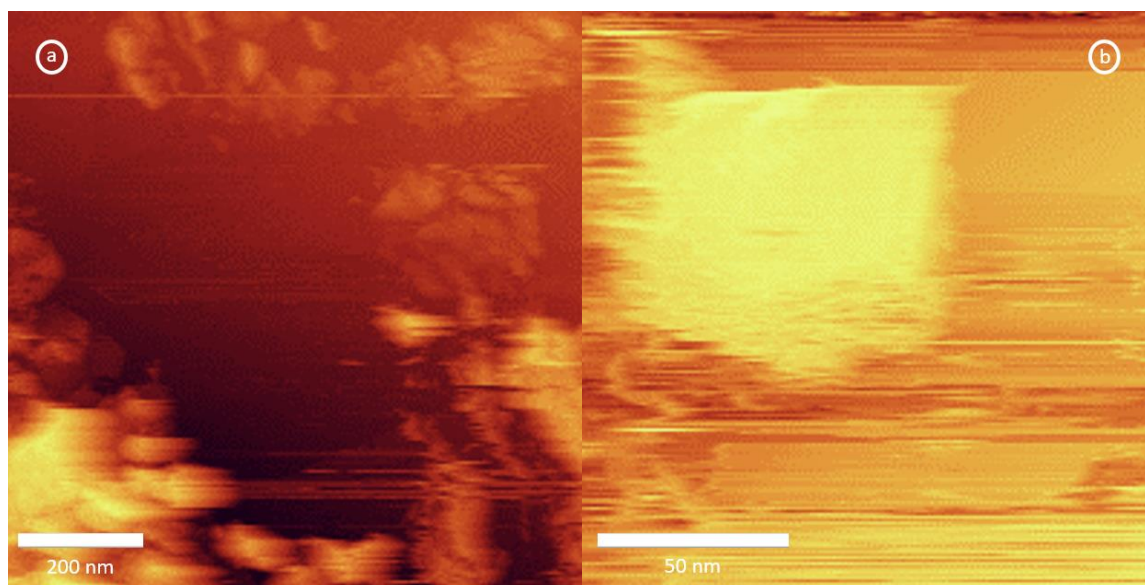

Figure 4.14: *Representative STM topographic images of Bi_2Se_3 NPLs before ligand treatment procedures were performed. a) An 1x1µm overview image, b) An 150x150nm image of a presumed NPL.*

It is immediately apparent that these images are of inadequate quality to perform high resolution STM experiments on NPLs. In comparison to AFM images shown in chapter 4.1.3 a significant increase in noise originating from tip instability is observed, both when scanning the background and on presumed NPLs, which causes a blurry topograph with a resolution unfit to properly characterize NPLs. This is assumed to be caused by a substantial concentration of organic contamination present on the HOPG surface and the NPLs, which is a common problem when transferring colloidally produced nanocrystals to a SPM system as organic ligands are generally necessary for stabilization of nanostructures in solution. An STM is particularly sensitive to organic contaminants as these large compounds can easily stick to the probe tip and significantly alter the tunnelling current by which the STM operates due to large differences in conductivity and changes in the tunnelling distance.

The sizable presence of organic material would also explain the large amorphous structures observed in the images, which are assumed to be aggregations of ligands that were either present in solution during drop-casting or on the NPL surface. Normally these would be removed during the annealing procedure performed in high vacuum. Therefore, the first attempt to improve the surface quality was an extended annealing step at higher temperatures (150°C). However, this did not significantly decrease the organic contamination encountered during measurements. This is probably due to the presence of an unusually large surfactant (PVP) which could be difficult to remove from the surface by evaporation due to its large size. Hence, attempts were made to modify the synthesis protocol to obtain NPLs without the usage of PVP or to remove PVP from the NPL surface and/or colloidal solution prior to STM insertion via a ligand treatment (LT) procedure.

Figure 4.15: *Representative TEM images of Bi$_2$Se$_3$ NPLs obtained by polyol hot injection procedure at varying surfactant concentrations. a) No PVP, b) OLAM instead of PVP.*

2 different strategies were employed in an effort to synthesize PVP-free NPLs. Surfactant-free synthesis of low quality Bi$_2$Se$_3$ nanoflakes by polyol reflux has been previously achieved simply by not adding PVP in the first place [24]. It is possible that our modified polyol hot injection method would yield NPLs of superior quality. Another idea was to switch PVP with OLAM, as it was previously used as a surfactant for Bi$_2$Se$_3$ in the synthesis by Wei et al. The TEM results from these 2 attempts are shown in Figure 4.15. Surfactant-free synthesis (4.15a) was successful in obtain some NPLs with trigonal symmetry, however various irregular nanostructures are clustered around them. This does exhibit a significant improvement from previously published results of surfactant-free Bi$_2$Se$_3$ NPLs. Unfortunately, they are not of adequate quality for our immediate goals, but future research could be worthwhile. OLAM synthesis (4.15b) yields NPLs which display significant flocculation similar to previously discussed results in chapter 4.1.2 and is therefore not considered further.
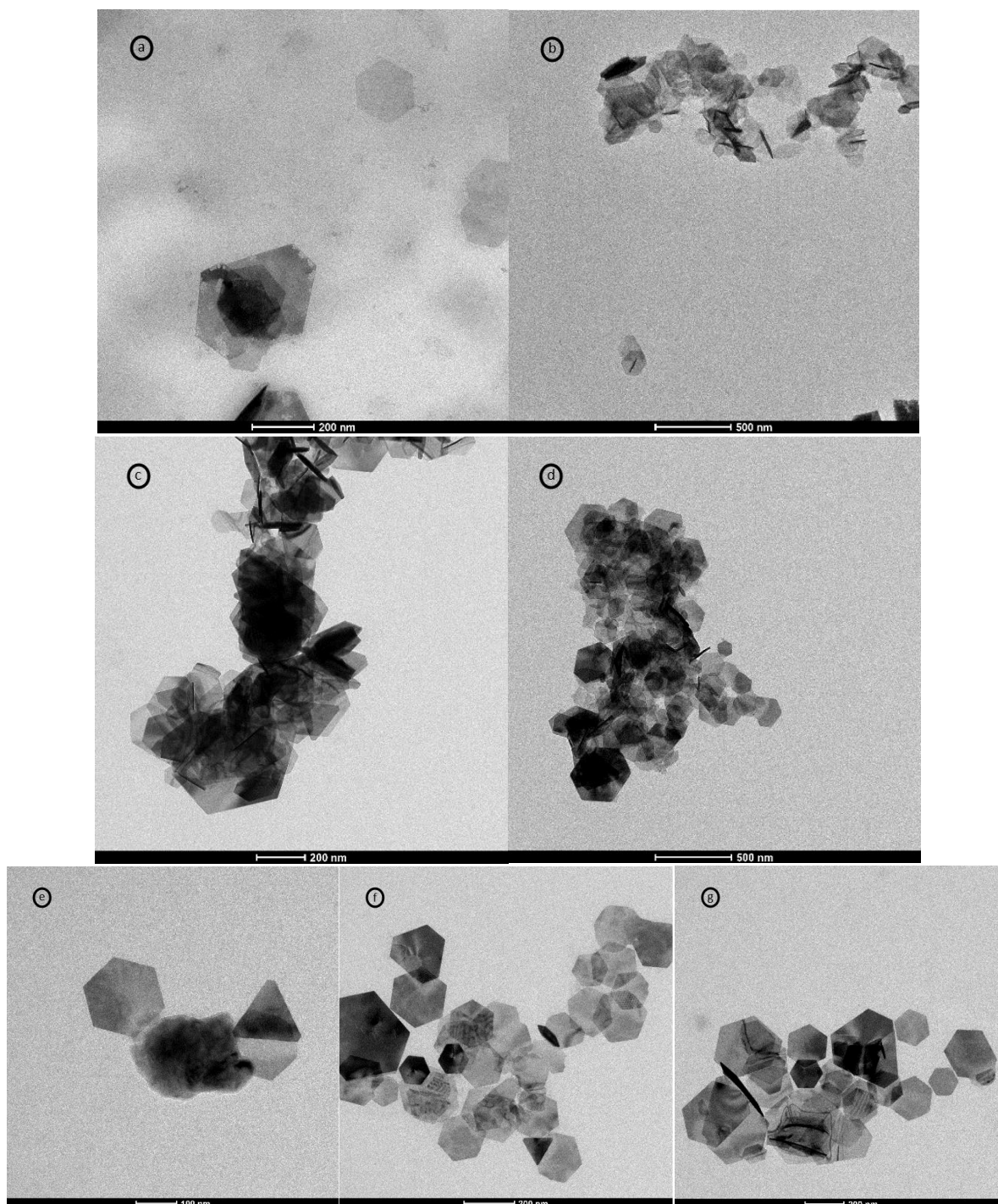
Figure 4.16: *Representative TEM images of Bi_2Se_3 NPLs obtained by ligand treatment with a) 1-dodecanthiol (DDT), b) $NaBH_4$, c) $CHCl_3$, d) Tributylamine (TBA), e) Thiophenol (TP), f) N_2H_4, g) OLAM.*

Several articles describe a successful removal of PVP from a variety of NC systems using various chemicals which act as either replacing ligands or ligand stripping agents. However, no publications were found which applied the method to Bi_2Se_3 NCs and thus it is unknown if these procedures would effectively reduce the PVP from the NPL surface. Therefore, a broad range of possible ligands/stripping agents are investigated. Figure 4.16a-g shows the TEM results of the LT procedure. It is important to realize that this technique cannot be used to characterize the type of ligands present on the NPL surface, but it can signify a significant increase in organic contamination in solution. For instance, in Figure 4.16a large variations in background contrast which change upon

observation with the electron beam suggest that pronounced quantities of DDT are present. No such effects are observed in other LT samples.

It is equally valuable to verify the quality of NPLs and their level of aggregation after LT to assure STM characterization is still feasible. Figures 4.16b-d show a notable rise in observed flocculation while Figures 4.16a,e display a degradation of NPL quality, and thus these methods are deemed insufficient for further investigation. Figures 4.16f,g seem to retain NPL shape and only show a slight increase in cluster formation while maintaining the presence of free NPLs. Therefore, LT with N_2H_4 and OLAM are considered most promising and are studied in more detail. Further TEM & AFM analysis yields results similar to the ones described in section 4.1.3, suggesting the NPL thickness and morphology were unaffected by LT. However, it is still unclear if PVP was successfully removed/exchanged.

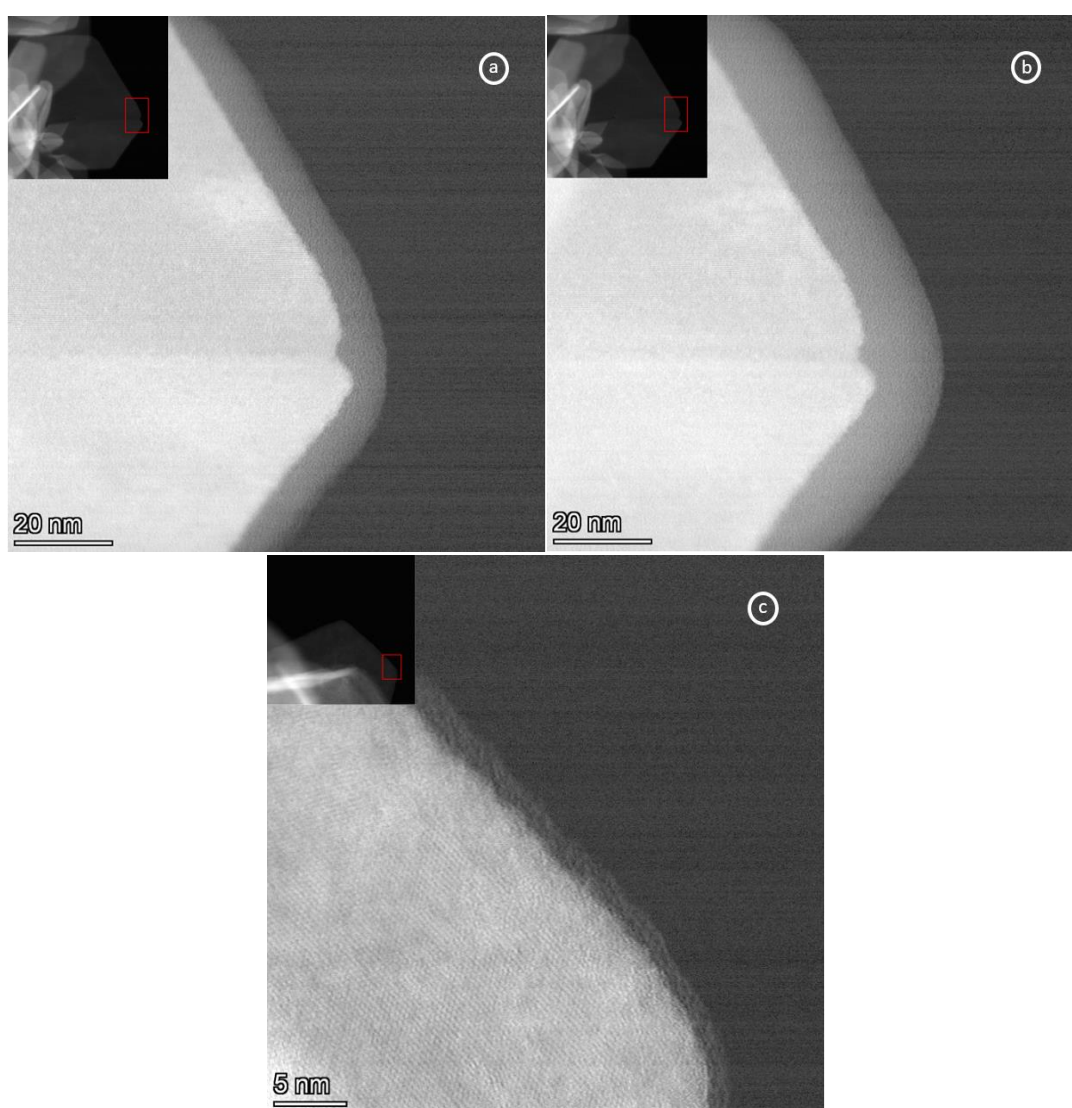### 4.2.1 Bi$_2$Se$_3$ NPL Ligand Characterization

Figure 4.17: *Representative high-resolution HAADF-STEM images of Bi$_2$Se$_3$ NPLs. The highlighted red areas in the top left overview images signify the area of the NPL under observation. a,b) Before ligand treatment. Images were taken a few seconds apart, c) After ligand treatment (OLAM) and plasma cleaning for 15 seconds.*

As previously mentioned, EM can be used to directly observe the presence of organic contaminants by their contrast and interaction with the electron beam. When using a microscope with enough resolution, this technique can also be used to verify the presence of organic surfactants present on the NPLs. Figure 4.17a-c show HR HAADF-STEM images of NPL edges from an untreated sample (4.17a,b) compared to a sample after LT with OLAM was performed (4.17c). It is clear that both NPLs still contain some quantity of surfactants, as a few-nm coating with low contrast is observed at their edges. This capping layer is seen growing outward (Figure 4.17b) after exposure to the high intensity electron beam for a few seconds, which is further evidence that it is not part of the NPL which seems unaffected during prolonged examination. Although the LT sample seems to have a less pronounced coating, these samples cannot be directly compared as a plasma cleaning step was performed to remove additional organic contaminants. All in all, surfactants have been observed on the edges of NPLs by HR HAADF-STEM although no conclusions on the characterization and quantity of the ligands can be made.
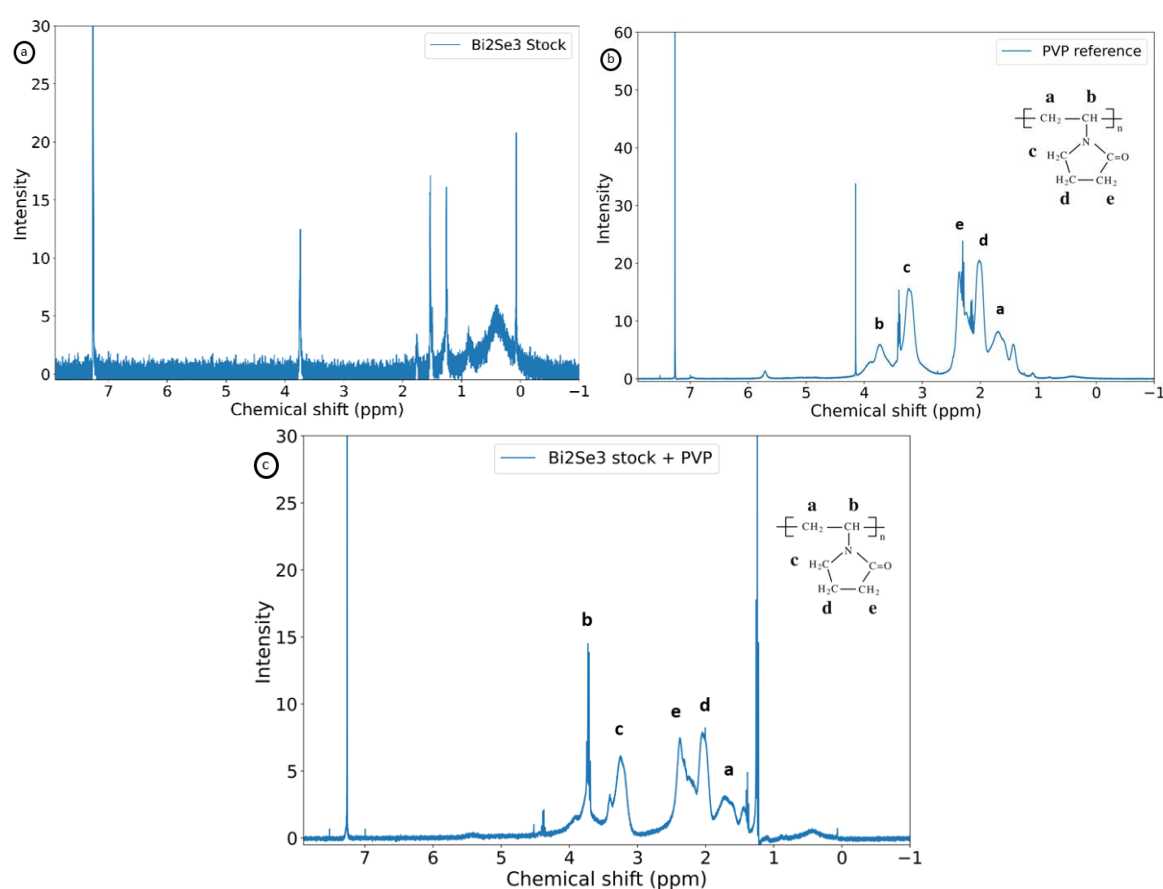
Figure 4.18: *Representative ^{1}H-NMR spectra from 8 to -1 ppm of a) Bi$_2$Se$_3$ NPLs, b) PVP, c) Bi$_2$Se$_3$ NPLs with added PVP. Identified signals are marked with corresponding letters in the PVP chemical structure.*

An attempt was made to characterize the surfactants present on the NPL surface to evaluate the success of the LT procedure by ^{1}H-NMR . The initial aim was to confirm the presence of PVP on the NPLs prior to ligand treatment. Figures 4.18a,b show measurements of a representative untreated NPL sample and a PVP reference spectrum respectively. The sharp peaks around 4 & 7 ppm present in both spectra originate from the added ferrocene as internal reference & deuterated chloroform as solvent respectively. Unfortunately, the NPL NMR spectrum suffers from a low signal to noise ratio which is probably related to a low colloidal stability of NPLs in the solvent utilized as the NPLs were

observed to quickly precipitate out of solution during measurements. A short detection time (5 seconds or less) was implemented to minimize the effect; however this did not seem to significantly improve the results.

A more substantial issue is the absence of peaks in the spectrum that correspond to the PVP reference. This could signify an absence of PVP in the sample, although this is doubtful as it is the only known surfactant present during synthesis. It is possible that some PVP is already removed by the washing procedure after synthesis, although this would not explain the significant organic contamination observed in STM measurements. More likely the concentration of PVP is below the detection limit of ^{1}H-NMR due to the aforementioned rapid precipitation of NPLs. To verify the ability to characterize PVP in the presence of Bi_2Se_3 NPLs, additional PVP (2.5 mg) was added to the sample prior to NMR measurement. The results of this are shown in Figure 4.18c and clearly depict a comparable peak pattern to the PVP reference which confirm that PVP can be accurately identified in the presence of NPLs. An improvement in colloidal stability of the NPLs was also observed, which explains the decreased level of noise and suggests PVP indeed acts as a stabilizing surfactant for Bi_2Se_3 NPLs. Unfortunately, this suggests that NMR could not be feasibly used to study the removal of PVP from Bi_2Se_3 NPLs unless a way to improve their dispersibility in chloroform was found without the addition of PVP. Nevertheless, an effort was made to study the NPLs by NMR after LT, as the observation of characteristic N_2H_4 or OLAM signals could still indicate a successful exchange. Alas, no such peaks were detected.
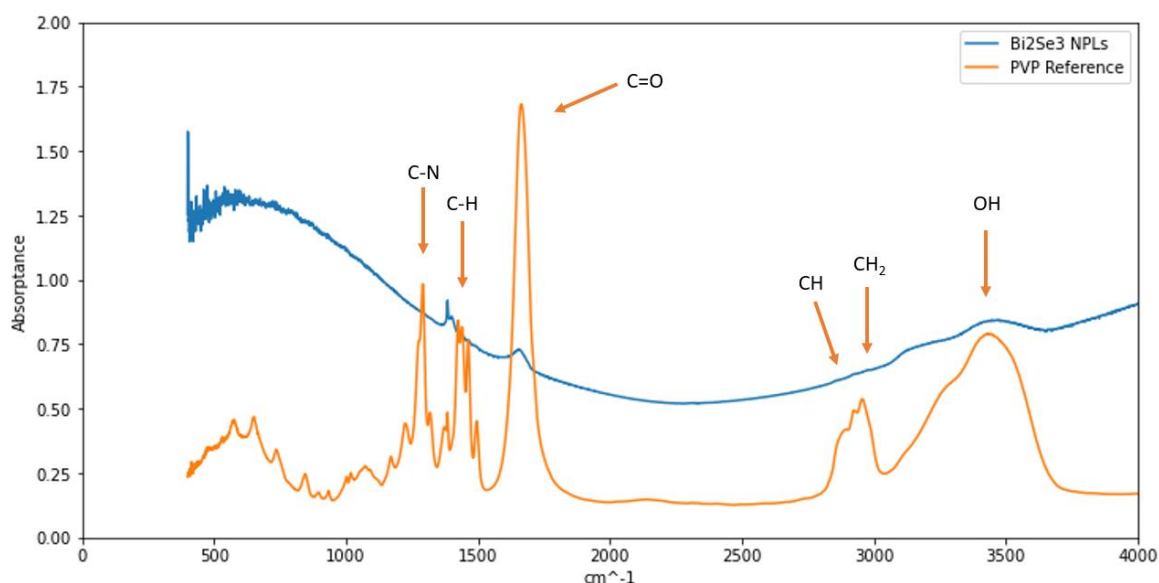
Figure 4.19: Representative FTIR absorbance spectra from 400-4000 cm^{-1}. Blue: Bi_2Se_3 NPLs, Orange: PVP. Identified vibrations are marked with orange arrows.

Another method which can be utilized to identify organic compounds at low concentrations is FTIR. This technique has the added benefit that colloidal stability is not required as samples can be studied in solid form. However, this means that pellets with a homogeneous sample distribution need to be produced to obtain satisfactory results. Figure 4.19 shows preliminary results of a representative NPL sample compared to a PVP reference. Some of the identifiable vibrations from the PVP reference have been labelled. Several of these peaks can also be observed in the NPL spectrum, albeit with considerably reduced intensity. It is debatable if these features are pronounced enough to justify characterization of PVP but it does seem promising to continue this endeavour possibly

with a higher concentration or an improved FTIR sample preparation method. However, due to time constraints this was not possible to achieve during this project.

4.2.2 NPL characterization by STM
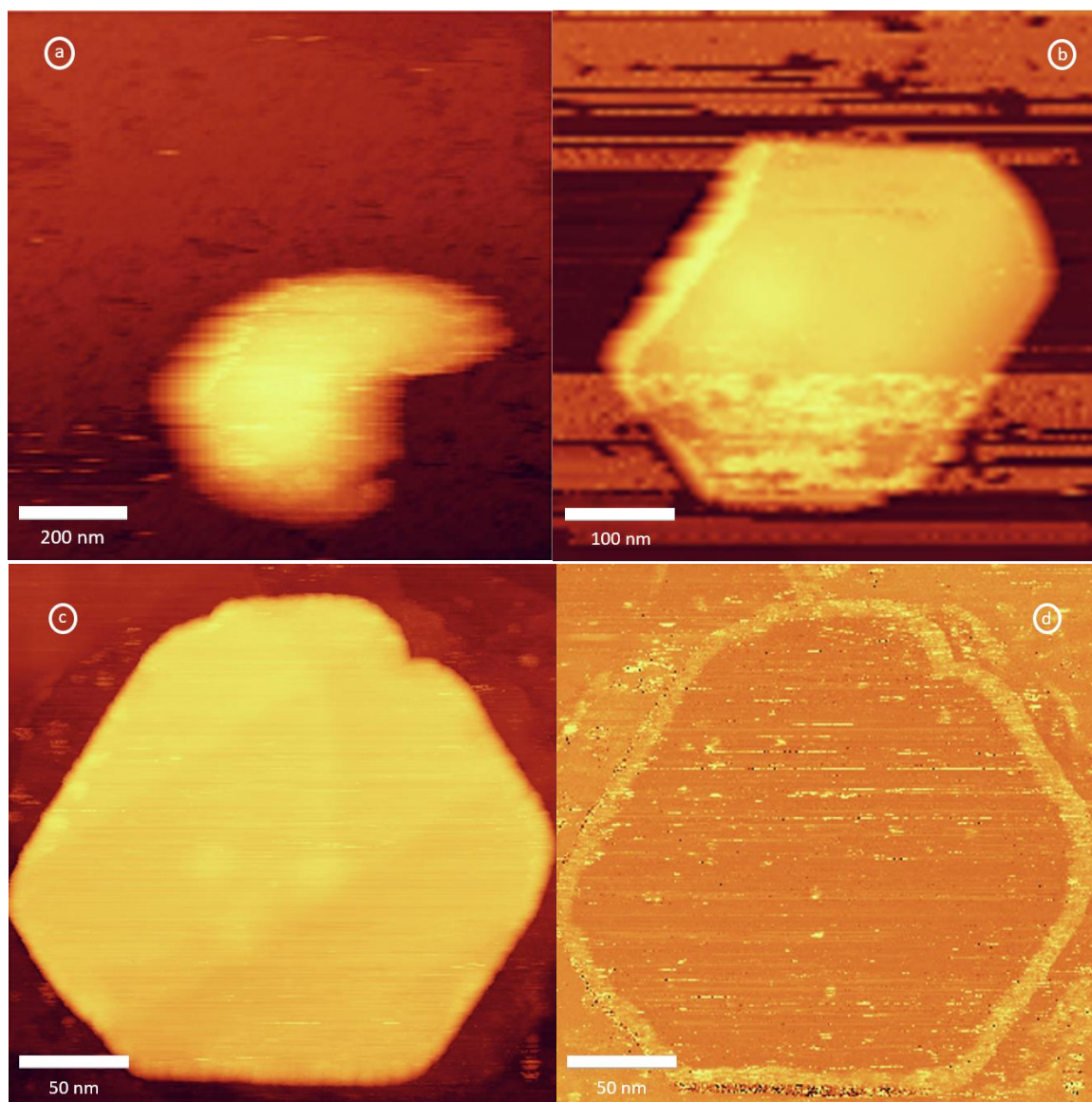
Figure 4.20: *Representative STM images of Bi$_2$Se$_3$ NPLs after ligand treatment procedures were performed. a) A distorted topographic image (1x1µm) of a NPL after N$_2$H$_4$ treatment, b) A topographic image (500x500nm) of a NPL after OLAM treatment, c) A topographic image (250x250nm) of a NPL after washing with ACN & N$_2$H$_4$ treatment, d) local conductivity map of c).*

Even though it is unclear if PVP removal/exchange was successful, it was decided to further investigate the samples with STM. Figures 4.20a-c show representative topographic images of LT samples before and after employing the improved washing procedure described in 4.1.3.1. When compared to initial STM results, it is clear that all procedures display superior NPL characterizability arising from an improved tip stability on both NPLs and background. This suggests that ligand treatment was successful to some extent, although identification of the exact effect by surfactant characterization techniques has thus far remained fruitless. Both N$_2$H$_4$ (4.20a) and OLAM (4.20b) treated samples display free NPLs and allow for clear distinction between NPLs and background.

However, the total coverage of free NPLs over the surface is quite low and tip instability still hinders the acquisition of high-resolution images. Fortunately, the extended washing procedure with ACN seems to further decrease organic contamination, which allows for high-resolution topographs such as Figure 4.20c to be obtained. This level of stability has also shown to be sufficient for advanced local conductivity mapping as observed in Figure 4.20d, which seems to display aw conductive edge state. However, further discussion of this result is complex and would require a more in-depth knowledge of topological band theory which is beyond the scope of this project and is thus left for future researchers to discuss.

4.2.3 Summary and Outlook

The focus of this chapter was to prepare the previously obtained Bi_2Se_3 NPLs for feasible STM studies by the removal or exchange of PVP from the NPL surface either by further modification of the reaction protocol or successive ligand treatment (LT) procedures, as initial measurements indicated an excessive level of organic contamination present in the sample which made high-resolution STM experiments unfeasible. The quality of NPLs after synthesis modification or LT was verified by TEM, which concluded that LT with OLAM and N_2H_4 were the only viable candidates for significant improvement of stability in STM conditions. An attempt was made to verify the presence, quantity and type of surfactants present in solution and on the NPL surface by HRHAADF-STEM, NMR & FTIR. Unfortunately, we were unable to identify anything more than the fact that some form of organic surfactant was still present on the NPLs after LT, although FTIR still held some promise of further improvement. Nevertheless, the procedure did show to significantly improve the characterizability of the NPLs by STM as successive measurements yielded stable high-resolution topographic images and even a conductivity map which showed the first signs of a predicted topological edge state.

This chapter merely touched upon the broad range of experiments that can be performed on these NPLs, both in the aspects of STM and ligand characterization. First off, now that the NPLs can be successfully characterized in the STM future experiments can undertake the challenge of investigating the exact behaviour of topological edge and surface states, for example in the presence of a magnetic field. To help accelerate this endeavour an improved coverage of NPLs over the surface would be beneficial. This means further examination and optimization of STM sample preparation from solution could be performed, as this is still done by a simple drop-casting procedure. Further characterization of NPL surfactants could also prove critical in understanding and improving ligand treatment. To this end, refining the previously utilized methods such as FTIR or branching out to other techniques is necessary. Surface-Enhanced Raman Spectroscopy (SERS) is one such technique which has previously shown to be successful in identifying ligands on nanostructures and even distinguish between bound and unbound states [102]. Finally, it would be very interesting to observe the differences in topological characteristics between Bi_2Se_3 and Bi_2Te_3 NPLs. Therefore, it would be worthwhile to investigate if this optimized could be used to successfully insert and examine previously produced Bi_2Te_3 NPLs in the STM. Although some prior improvements in synthesis protocol would be needed, as described in 4.1.3.

Chapter 5.

Conclusion

The first part of this thesis aimed to obtain and optimize a Bi_2Se_3 & Bi_2Te_3 NPL synthesis procedure for the eventual investigation of their topological characteristics in STM. As the reproduction of previously reported protocols was more arduous than initially expected, a modified process needed to be developed. This was achieved by combining features of two established procedures, which finally allowed for the feasible acquisition of high quality Bi_2Se_3 NPLs with respect to their crystallinity, morphology, and level of flocculation as confirmed by HAADF-STEM, ED, XRD, EDX & AFM analysis. The modified procedure can straightforwardly be adapted to produce Bi_2Te_3 NPLs as well, although their quality was confirmed to be somewhat reduced in comparison to the Bi_2Se_3 NPLs. Variation of several principal synthesis parameters allowed us to control lateral dimensions to a certain degree without decreasing NPL quality and provided novel insight into NPL growth dynamics.

The second part of this thesis focussed more on the identification and modification of the surfactants present on the NPLs, which was a necessary endeavour to improve STM characterizability. A ligand treatment protocol was successfully employed to this end as stable high-resolution topographic images were eventually obtained with which further research can be performed. However, proper characterization of ligand identity and concentration by ^{1}H-NMR and FTIR has thus far proven ineffective. As such a more thorough investigation is needed to confirm the success of the removal and/or exchange of surfactants from the NPLs.

Acknowledgements

Bibliography

1. Celso de Mello Donegá. Nanoparticles: workhorses of nanoscience. Springer,
2. Daniel Vanmaekelbergh, Solids and Surfaces lecture notes
3. Zhang, S. (2015, July 28). *Topological insulators - Scholarpedia*. http://www.scholarpedia.org/article/Topological_insulators
4. Zhu, Zhiyong, Yingchun Cheng, and Udo Schwingenschlögl. "Band inversion mechanism in topological insulators: A guideline for materials design." Physical Review B 85.23 (2012): 235401.
5. Roushan, P., Seo, J., Parker, C. V., Hor, Y. S., Hsieh, D., Qian, D., ... & Yazdani, A. (2009). Topological surface states protected from backscattering by chiral spin texture. Nature, 460(7259), 1106-1109.
6. Moore, J. E. (2010). The birth of topological insulators. Nature, 464(7286), 194-198.
7. Zhang, Y., He, K., Chang, C. Z., Song, C. L., Wang, L. L., Chen, X., ... & Xue, Q. K. (2010). Crossover of the three-dimensional topological insulator Bi2Se3 to the two-dimensional limit. Nature Physics, 6(8), 584-588.
8. Xia, Y., Qian, D., Hsieh, D., Wray, L., Pal, A., Lin, H., ... & Hasan, M. Z. (2009). Observation of a large-gap topological-insulator class with a single Dirac cone on the surface. Nature physics, 5(6), 398-402.
9. Zhang, H., Liu, C. X., Qi, X. L., Dai, X., Fang, Z., & Zhang, S. C. (2009). Topological insulators in Bi2Se3, Bi2Te3 and Sb2Te3 with a single Dirac cone on the surface. Nature physics, 5(6), 438-442.
10. Nasilowski, M., Mahler, B., Lhuillier, E., Ithurria, S., & Dubertret, B. (2016). Two-dimensional colloidal nanocrystals. Chemical reviews, 116(18), 10934-10982.
11. Samanta, M., & Biswas, K. (2020). 2D Nanosheets of Topological Quantum Materials from Homologous (Bi2) m (Bi2Se3) n Heterostructures: Synthesis and Ultralow Thermal Conductivity. Chemistry of Materials, 32(20), 8819-8826.
12. Bauer, C., Veremchuk, I., Kunze, C., Benad, A., Dzhagan, V. M., Haubold, D., ... & Eychmüller, A. (2021). Heterostructured Bismuth Telluride Selenide Nanosheets for Enhanced Thermoelectric Performance. Small Science, 1(1), 2000021.
13. Nag, A., Kovalenko, M. V., Lee, J. S., Liu, W., Spokoyny, B., & Talapin, D. V. (2011). Metal-free inorganic ligands for colloidal nanocrystals: S2–, HS–, Se2–, HSe–, Te2–, HTe–, TeS32–, OH–, and NH2–as surface ligands. Journal of the American Chemical Society, 133(27), 10612-10620
14. Wei, T., Zhang, Y., Dong, W., Huang, C., Sun, Y., Chen, X., & Dai, N. (2013). A solution synthetic route toward Bi2 S e3 layered nanostructures with tunable thickness via weakening precursor reactivity. physica status solidi (a), 210(9), 1909-1913.
15. Min, Y., Moon, G. D., Kim, B. S., Lim, B., Kim, J. S., Kang, C. Y., & Jeong, U. (2012). Quick, controlled synthesis of ultrathin Bi2Se3 nanodiscs and nanosheets. Journal of the American Chemical Society, 134(6), 2872-2875.
16. Zhang, K. F., Yang, F., Song, Y. R., Liu, C., Qian, D., Gao, C. L., & Jia, J. F. (2015). Strongly compressed Bi (111) bilayer films on Bi2Se3 studied by scanning tunneling microscopy. Applied Physics Letters, 107(12), 121601.
17. Wikimedia Commons. (September 26, 2015). *Band Gap Comparison* [Online]. Available: https://upload.wikimedia.org/wikipedia/commons/thumb/0/0b/Band_gap_comparison.svg/2000px-Band_gap_comparison.svg.png
18. Wikipedia, Mug and Torus gif,

https://en.wikipedia.org/wiki/File:Mug_and_Torus_morph.gif

19. *What is band inversion and how to recognize it in band structure?* (2020, May 19). Matter Modeling Stack Exchange. https://mattermodeling.stackexchange.com/questions/909/what-is-band-inversion-and-how-to-recognize-it-in-band-structure

20. Hakl, M. (2017). Infrared magneto-spectroscopy of relativistic-like electrons in three-dimensional solids (Doctoral dissertation, Université Grenoble Alpes (ComUE)).

21. Steane, A. (1998). Quantum computing. Reports on Progress in Physics, 61(2), 117.

22. Sriraam, N (2020). Biomedical and Clinical engineering for healthcare advancement. IGI Global

23. Jiang, Y., Hao, M., Jiang, L., Liu, F., & Liu, Y. (2016). Shape and stoichiometry control of bismuth selenide nanocrystals in colloidal synthesis. RSC advances, 6(53), 47840-47843.

24. Min, Y., Roh, J. W., Yang, H., Park, M., Kim, S. I., Hwang, S., ... & Jeong, U. (2013). Surfactant-free scalable synthesis of Bi2Te3 and Bi2Se3 nanoflakes and enhanced thermoelectric properties of their nanocomposites. Advanced Materials, 25(10), 1425-1429.

25. Min, Y., Park, G., Kim, B., Giri, A., Zeng, J., Roh, J. W., ... & Jeong, U. (2015). Synthesis of multishell nanoplates by consecutive epitaxial growth of Bi2Se3 and Bi2Te3 nanoplates and enhanced thermoelectric properties. ACS nano, 9(7), 6843-6853.

26. Lin, Z., Chen, Y., Yin, A., He, Q., Huang, X., Xu, Y., ... & Duan, X. (2014). Solution processable colloidal nanoplates as building blocks for high-performance electronic thin films on flexible substrates. Nano letters, 14(11), 6547-6553.

27. Jiang, Y., Zhu, Y. J., & Cheng, G. F. (2006). Synthesis of Bi2Se3 nanosheets by microwave heating using an ionic liquid. Crystal growth & design, 6(9), 2174-2176.

28. Razzaque, S., Khan, M. D., Aamir, M., Sohail, M., Bhoyate, S., Gupta, R. K., ... & Revaprasadu, N. (2021). Selective Synthesis of Bismuth or Bismuth Selenide Nanosheets from a Metal Organic Precursor: Investigation of their Catalytic Performance for Water Splitting. Inorganic Chemistry, 60(3), 1449-1461.

29. Sun, L., Lin, Z., Peng, J., Weng, J., Huang, Y., & Luo, Z. (2014). Preparation of few-layer bismuth selenide by liquid-phase-exfoliation and its optical absorption properties. Scientific reports, 4(1), 1-9.

30. Ali, Z., Cao, C., Li, J., Wang, Y., Cao, T., Tanveer, M., ... & Butt, F. K. (2013). Effect of synthesis technique on electrochemical performance of bismuth selenide. Journal of power sources, 229, 216-222.

31. Soni, A., Yanyuan, Z., Ligen, Y., Aik, M. K. K., Dresselhaus, M. S., & Xiong, Q. (2012). Enhanced thermoelectric properties of solution grown Bi2Te3–x Se x nanoplatelet composites. Nano letters, 12(3), 1203-1209.

32. Xu, H., Chen, G., Jin, R., Chen, D., Wang, Y., Pei, J., ... & Qiu, Z. (2014). Microwave-assisted synthesis of Bi 2 Se 3 ultrathin nanosheets and its electrical conductivities. CrystEngComm, 16(19), 3965-3970.

33. Cui, H., Liu, H., Li, X., Wang, J., Han, F., Zhang, X., & Boughton, R. I. (2004). Synthesis of Bi2Se3 thermoelectric nanosheets and nanotubes through hydrothermal co-reduction method. Journal of Solid State Chemistry, 177(11), 4001-4006.

34. Lee, P. C., Wei, P. C., & Chen, Y. Y. (2021). Thermoelectric Characteristics of A Single-Crystalline Topological Insulator Bi2Se3 Nanowire. Nanomaterials, 11(3), 819.

35. Bauer, C., Lesyuk, R., Khoshkhoo, M. S., Klinke, C., Lesnyak, V., & Eychmüller, A. (2021). Surface Defines the Properties: Colloidal Bi2Se3 Nanosheets with High Electrical Conductivity. The Journal of Physical Chemistry C.

36. Huang, Y., Wang, K., Guo, T., Li, J., Wu, X., & Zhang, G. (2020). Construction of 2D/2D Bi2Se3/g-C3N4 nanocomposite with High interfacial charge separation and photo-heat conversion efficiency for selective photocatalytic CO2 reduction. Applied Catalysis B: Environmental, 277, 119232.

37. Chae, J., Hong, S. B., Kim, D., Kim, D. K., Kim, J., Jeong, K., ... & Cho, M. H. (2021). Enhancement of photoresponse in Bi2Se3/graphene heterostructures by effective electron–hole separation through internal band bending. Applied Surface Science, 554, 149623.

38. Pradhan, M., Chakraborty, R., Rudra, S., Koley, S., Maji, P. K., Nayak, A. K., ... & Nandi, U. (2021). Intercalation pseudocapacitance in Bi2Se3– MnO2 nanotube composite for high electrochemical energy storage. Electrochimica Acta, 367, 137531.

39. Kong, D., Koski, K. J., Cha, J. J., Hong, S. S., & Cui, Y. (2013). Ambipolar field effect in Sb-doped Bi2Se3 nanoplates by solvothermal synthesis. Nano letters, 13(2), 632-636.

40. Kong, D., Dang, W., Cha, J. J., Li, H., Meister, S., Peng, H., ... & Cui, Y. (2010). Few-layer nanoplates of Bi2Se3 and Bi2Te3 with highly tunable chemical potential. Nano letters, 10(6), 2245-2250.

41. Li, D., Fang, M., Jiang, C., Lin, H., Luo, C., Qi, R., ... & Peng, H. (2018). Size-controlled synthesis of hierarchical bismuth selenide nanoflowers and their photocatalytic performance in the presence of H 2 O 2. Journal of nanoparticle research, 20(9), 1-10

42. Sharma, D., Kumar, Y., Kumar, P., Nagpal, V., Patnaik, S., & Awana, V. P. S. (2021). High field magneto-transport of mixed topological insulators Bi2Se3-xTex (x= 0, 1, 2 & 3). Solid State Communications, 323, 114097

43. Kim, H. S., Hwang, T. H., Kim, N. H., Hou, Y., Yu, D., Sim, H. S., & Doh, Y. J. (2020). Adjustable quantum interference oscillations in Sb-doped Bi2Se3 topological insulator nanoribbons. ACS nano, 14(10), 14118-14125.

44. Riney, L., Bunker, C., Bac, S. K., Wang, J., Battaglia, D., Park, Y. C., ... & Assaf, B. A. (2021). Introduction of Sr into Bi2Se3 thin films by molecular beam epitaxy. Journal of Applied Physics, 129(8), 085107.

45. Peng, H., Lai, K., Kong, D., Meister, S., Chen, Y., Qi, X. L., ... & Cui, Y. (2010). Aharonov–Bohm interference in topological insulator nanoribbons. Nature materials, 9(3), 225-229.

46. Ren, Y., Li, Y., & Liu, X. (2021). Investigation on band alignment of Bi2Se3–PbSe heterojunction. Applied Physics Letters, 118(16), 162101.

47. Nasilowski, M., Mahler, B., Lhuillier, E., Ithurria, S., & Dubertret, B. (2016). Two-dimensional colloidal nanocrystals. Chemical reviews, 116(18), 10934-10982.

48. Zhang, N., Zheng, F., Huang, B., Ji, Y., Shao, Q., Li, Y., ... & Huang, X. (2020). Exploring Bi2Te3 Nanoplates as Versatile Catalysts for Electrochemical Reduction of Small Molecules. Advanced Materials, 32(22), 1906477.

49. Nethravathi, C., Dattatreya Manganahalli, A., & Rajamathi, M. (2019). Bi2Te3–MoS2 Layered Nanoscale Heterostructures for Electron Transfer Catalysis. ACS Applied Nano Materials, 2(4), 2005-2012.

50. Sun, Z., Liufu, S., Chen, X., & Chen, L. (2010). Controllable synthesis and electrochemical hydrogen storage properties of Bi2Se3 architectural structures. Chemical communications, 46(18), 3101-3103.

51. Nakayama, K., Kimizuka, H., Tanaka, Y., Sato, T., Souma, S., Takahashi, T., ... & Ando, Y. (2015). Observation of two-dimensional bulk electronic states in the superconducting topological insulator heterostructure Cu x (PbSe) 5 (Bi 2 Se 3) 6: Implications for unconventional superconductivity. Physical Review B, 92(10), 100508.

52. Li, B., Cheng, Y., Zheng, R., Wu, X., Qi, F., Wu, Y., ... & Li, X. (2020). Improving the photothermal therapy efficacy and preventing the surface oxidation of bismuth nanoparticles through the formation of a bismuth@ bismuth selenide heterostructure. Journal of Materials Chemistry B, 8(38), 8803-8808

53. Green, Avery James, and Alain Diebold. "Characterization and Control of the Surface of the Topological Insulator Bi2Se3." (2017).

54. Zhang, J., Peng, Z., Soni, A., Zhao, Y., Xiong, Y., Peng, B., ... & Xiong, Q. (2011). Raman spectroscopy of few-quintuple layer topological insulator Bi2Se3 nanoplatelets. Nano letters, 11(6), 2407-2414.

55. Zhang, G., Wang, W., Lu, X., & Li, X. (2009). Solvothermal synthesis of V− VI binary and ternary hexagonal platelets: the oriented attachment mechanism. Crystal Growth and Design, 9(1), 145-150.

56. Wei, T., Zhang, Y., Dong, W., Huang, C., Sun, Y., Chen, X., & Dai, N. (2013). A solution synthetic route toward Bi2 S e3 layered nanostructures with tunable thickness via weakening precursor reactivity. physica status solidi (a), 210(9), 1909-1913.

57. Lu, W., Ding, Y., Chen, Y., Wang, Z. L., & Fang, J. (2005). Bismuth telluride hexagonal nanoplatelets and their two-step epitaxial growth. Journal of the American Chemical Society, 127(28), 10112-10116.

58. Zhang, K. F., Yang, F., Song, Y. R., Liu, C., Qian, D., Gao, C. L., & Jia, J. F. (2015). Strongly compressed Bi (111) bilayer films on Bi2Se3 studied by scanning tunneling microscopy. Applied Physics Letters, 107(12), 121601.

59. Zhu, H., Zhou, W., & Yarmoff, J. A. (2018). The growth of bismuth on Bi2Se3 and the stability of the first bilayer. Thin Solid Films, 660, 343-352.

60. Miao, L., Wang, Z. F., Ming, W., Yao, M. Y., Wang, M., Yang, F., ... & Jia, J. F. (2013). Quasiparticle dynamics in reshaped helical Dirac cone of topological insulators. Proceedings of the National Academy of Sciences, 110(8), 2758-2762.

61. Eich, A., Michiardi, M., Bihlmayer, G., Zhu, X. G., Mi, J. L., Iversen, B. B., ... & Wiebe, J. (2014). Intra-and interband electron scattering in a hybrid topological insulator: Bismuth bilayer on Bi 2 Se 3. Physical Review B, 90(15), 155414.

62. Sabater, C., Gosálbez-Martínez, D., Fernández-Rossier, J., Rodrigo, J. G., Untiedt, C., & Palacios, J. J. (2013). Topologically protected quantum transport in locally exfoliated bismuth at room temperature. Physical review letters, 110(17), 176802.

63. Liu, X., & Hersam, M. C. (2018). Interface characterization and control of 2D materials and heterostructures. Advanced Materials, 30(39), 1801586.

64. Min, Y., Im, E., Hwang, G. T., Kim, J. W., Ahn, C. W., Choi, J. J., ... & Moon, G. D. (2019). Heterostructures in two-dimensional colloidal metal chalcogenides: Synthetic fundamentals and applications. Nano Research, 12(8), 1750-1769.

65. Sugimoto, Tadao. "The theory of the nucleation of monodisperse particles in open systems and its application to AgBr systems." Journal of colloid and interface science 150.1 (1992): 208-225.

66. Besson, Claire, Eric E. Finney, and Richard G. Finke. "A mechanism for transition-metal nanoparticle self-assembly." Journal of the American Chemical Society 127.22 (2005): 8179-8184.

67. de Mello Donegá, Celso. "Synthesis and properties of colloidal heteronanocrystals." Chemical Society Reviews 40.3 (2011): 1512-1546.

68. Philipse, Albert. "Lecture Notes Colloidal Dispersions" 2021

69. Zhang, Qiao, Shu-Juan Liu, and Shu-Hong Yu. "Recent advances in oriented attachment growth and synthesis of functional materials: concept, evidence, mechanism, and future." Journal of Materials Chemistry 19.2 (2009): 191-207.

70. Klokkenburg, M., Houtepen, A., Koole, R., De Folter, J.W., Erné, B.H., Van Faasen, E., Vanmaekelbergh, D.: Dipolar structures in colloidal dispersions of PbSe and CdSe quantum dots. Nano Lett. 7, 2931–2936 (2007)

71. Kwon, Soon Gu, and Taeghwan Hyeon. "Formation mechanisms of uniform nanocrystals via hot-injection and heat-up methods." Small 7.19 (2011): 2685-2702.

72. Chen, Ruhui, Quynh N. Nguyen, and Younan Xia. "Oriented Attachment: A Unique Mechanism for the Colloidal Synthesis of Metal Nanostructures." ChemNanoMat 8.3 (2022): e202100474.

73. Akkerman, Quinten "Lead Halide Perovskite Nanocrystals: A New Age of Semiconductive Nanocrystals" PhD Thesis, Genova University, 2018

74. Tom, A. E., Thomas, A., & Ison, V. V. (2020). Novel post-synthesis purification strategies and the ligand exchange processes in simplifying the fabrication of PbS quantum dot solar cells. RSC Advances, 10(51), 30707-30715.

75. Talapin, D. V., Lee, J. S., Kovalenko, M. V., & Shevchenko, E. V. (2010). Prospects of colloidal nanocrystals for electronic and optoelectronic applications. Chemical reviews, 110(1), 389-458.

76. Buchenau, Sören, et al. "Scalable polyol synthesis for few quintuple layer thin and ultra high aspect ratio Bi2Se3 structures." Solid State Communications 281 (2018): 49-52.

77. Das, Soumendra Kumar, and Prahallad Padhan. "Surface-Induced Enhanced Band Gap in the (0001) Surface of Bi2Se3 Nanocrystals: Impacts on the Topological Effect." ACS Applied Nano Materials 3.1 (2019): 274-282.

78. Wang, Fakun K., Sijie J. Yang, and Tianyou Y. Zhai. "2D Bi2Se3 materials for optoelectronics." Iscience 24.11 (2021): 103291.

79. Schiettecatte, P., Rousaki, A., Vandenabeele, P., Geiregat, P., & Hens, Z. (2020). Liquid-Phase Exfoliation of Rhenium Disulfide by Solubility Parameter Matching. Langmuir, 36(51), 15493-15500.

80. Inkson, B. J. (2016). Scanning electron microscopy (SEM) and transmission electron microscopy (TEM) for materials characterization. In Materials characterization using nondestructive evaluation (NDE) methods (pp. 17-43). Woodhead Publishing.

81. Tadjine, A., & Delerue, C. (2017). Topological protection of electronic states against disorder probed by their magnetic moment. Physical Review B, 95(23), 235426.

82. Kane, C. L. (2013). Topological Band Theory and the $\mathbb{Z}2$ Invariant. In Contemporary Concepts of Condensed Matter Science (Vol. 6, pp. 3-34). Elsevier.

83. Tom, A. E., Thomas, A., & Ison, V. V. (2020). Novel post-synthesis purification strategies and the ligand exchange processes in simplifying the fabrication of PbS quantum dot solar cells. RSC Advances, 10(51), 30707-30715.

84. Electron Diffraction. (n.d.). Cyberphysics. Retrieved June 1, 2021, from https://www.cyberphysics.co.uk/topics/atomic/electron_diffraction.htm

85. Holder, C. F., & Schaak, R. E. (2019). Tutorial on powder X-ray diffraction for characterizing nanoscale materials.

86. Nanakoudis, A. (2019, November 28). EDX Analysis with SEM: How Does it Work? Accelerating Microscopy. https://www.thermofisher.com/blog/microscopy/edx-analysis-with-sem-how-does-it-work/

87. Bhunia, H., Bar, A., Bera, A., & Pal, A. J. (2017). Simultaneous observation of surface-and edge-states of a 2D topological insulator through scanning tunneling spectroscopy and differential conductance imaging. Physical Chemistry Chemical Physics, 19(15), 9872-9878.

88. Fan, Q., Yang, H., Ge, J., Zhang, S., Liu, Z., Lei, B., ... & Gao, C. (2020). Customizable ligand exchange for tailored surface property of noble metal nanocrystals. Research, 2020.

89. ABB Review, 23-02-2021, Quantum computing: the hype and hopes. https://new.abb.com/news/detail/74736/quantum-computing-the-hype-and-hopes

90. He, M., Sun, H., & He, Q. L. (2019). Topological insulator: Spintronics and quantum computations. Frontiers of Physics, 14(4), 1-16.

91. Cho, S., Kim, D., Syers, P., Butch, N. P., Paglione, J., & Fuhrer, M. S. (2012). Topological insulator quantum dot with tunable barriers. Nano letters, 12(1), 469-472.

92. Xu, S., Zhao, W. B., Hong, J. M., Zhu, J. J., & Chen, H. Y. (2005). Photochemical synthesis of Bi2Se3 nanosphere and nanorods. Materials Letters, 59(2-3), 319-321.

93. Bhunia, H., Bar, A., Bera, A., & Pal, A. J. (2017). Simultaneous observation of surface-and edge-states of a 2D topological insulator through scanning tunneling spectroscopy and differential conductance imaging. Physical Chemistry Chemical Physics, 19(15), 9872-9878.

94. Luo, Muhua, et al. "Facile removal of polyvinylpyrrolidone (PVP) adsorbates from Pt alloy nanoparticles." Journal of Materials Chemistry A 3.6 (2015): 2770-2775.

95. Moran, Christine H., et al. "Replacement of poly (vinyl pyrrolidone) by thiols: a systematic study of Ag nanocube functionalization by surface-enhanced Raman scattering." The Journal of Physical Chemistry C 115.44 (2011): 21852-21857.

96. Maiti, Pradipta Sankar, et al. "Oriented attachment of 2D nanosheets: the case of few-layer Bi2Se3." Chemistry of Materials 33.18 (2021): 7558-7565.

97. Khatun, Salma, Hrishikesh Bhunia, and Amlan J. Pal. "Bi 2 Se 3 topological insulator at the 2D-limit: role of halide-doping on Dirac point." Physical Chemistry Chemical Physics 20.26 (2018): 17934-17941.

98. Comor, M. I., Dramicanin, M. D., Rakocevic, Z., Zec, S., & Nedeljkovic, J. M. (1998). Preparation of Bi2Se3 quantum dots by dissolution of crystalline powder in acetonitrile. Journal of materials science letters, 17(1401), 1401-1402.

99. Klinger, M., & Jäger, A. (2015). Crystallographic Tool Box (CrysTBox): automated tools for transmission electron microscopists and crystallographers. Journal of applied crystallography, 48(6), 2012-2018.

100. Nečas, D., & Klapetek, P. (2012). Gwyddion: an open-source software for SPM data analysis. Open Physics, 10(1), 181-188.

101. Rühl, S. (2015). Inorganic crystal structure database (ICSD). A Focus on Crystallography, 6.

102. Cure, J., Coppel, Y., Dammak, T., Fazzini, P. F., Mlayah, A., Chaudret, B., & Fau, P. (2015). Monitoring the coordination of amine ligands on silver nanoparticles using NMR and SERS. Langmuir, 31(4), 1362-1367.

103. Yan, B., Zhang, D., & Felser, C. (2013). Topological surface states of Bi2Se3 coexisting with Se vacancies. physica status solidi (RRL)–Rapid Research Letters, 7(1-2), 148-150.

Appendix A.

List of Samples

Table A1: Bi_2Se_3 Synthesis Overview

Sample Name	Method	Varied parameters	Characterization	Results
TW02	Reflux[1]	None	TEM, XRD	Large rectangular structures
TW03	Reflux[1]	Higher T (Unknown) & Aliquots taken	TEM, XRD	Several types of poorly defined nanostructures
TW04	Reflux[1]	Bi_2O_3 instead of BiNO	TEM, XRD	Wrinkled, non-hexagonal NPLs
TW05	Reflux[1]	Aliquots	TEM, XRD	Several types of poorly defined nanostructures
TW06	Reflux[1]	Bi_2O_3 & Aliquots taken	TEM, XRD	Messy hexagonal NPLs
TW10	Hot injection[2]	TOP-Se & Bi-OA	TEM, XRD	Connected round blobs of Bi_2O_3
TW11	Hot injection[2]	Less TOP-Se	TEM	Connected round blobs of Bi_2O_3
TW12	Hot injection[2]	less reaction time (1 min)	TEM, XRD	Connected polygons of Bi_2O_3
TW13	Hot injection[2]	Less Bi-OA	TEM	Connected polygons of Bi_2O_3
TW14	Reflux[1]	N_2 environment	TEM, XRD, ED, EDX	Hexagonal Microplateles (MPLs) as well as rod shaped particles
TW16	Hot injection[2]	Se-OLAM & Bi-OA	TEM	Heavily clustered, smaller NPLs (100 nm)
TW18	Hot injection[2]	Less Se-OLAM & Less Bi-OA	TEM	Heavily clustered, smaller NPLs (100 nm)
TW19	Hot injection[2]	Added PVP	TEM	Heavily clustered, smaller NPLs (100 nm)
TW20	Hot injection[2]	Aliquots	TEM	Heavily clustered, smaller NPLs (100 nm)
TW21	Hot injection[2]	Added NaOH	TEM	Heavily clustered amorphous clumps
TW22	Ligand Exchange[3]	TW16: KOH & $NaNH_2$	X	Unsuccessful transfer to FA so ligand exchange is assumed unsuccessful
TW23	Ligand Exchange[3]	TW16: Na_2S & NaHS	X	Unsuccessful transfer to FA so ligand exchange is assumed unsuccessful
TW24	Reflux[1]	N_2 & Less BiNO	TEM	Messy, non-hexagonal MPLs
TW25	Reflux[1]	N_2 & Less Na_2SeO_3	TEM	Hexagonal MPLs as well as rod shaped particles
TW27	Reflux[1]	N_2 & Less BiNO & Na_2SeO_3	TEM	Messy, non-hexagonal MPLs & Dumbell shaped NPs
TW28	Hot injection	2h reaction time	TEM , XRD, AFM, ED, EDX, UV-VIS	Clustered, but well defined hexagonal NPLs

TW29	Hot injection	2h reaction time & Na$_2$SeO$_3$ injected instead of BiNO	TEM	Clustered, non-hexagonal MPLs as well as amorphous structures
TW30	Hot injection	2h reaction time & Aliquots taken	TEM, AFM, ED	Nicely separated hexagonal NPLs, after 10 min not much change is observed
TW31	Hot injection	2h reaction time & Hexane as antisolvent	TEM	Very clustered hexagonal MPLs as well as other structures
TW32	Hot injection	2h reaction time & 2x upscale	XRD	Good crystalline quality
TW34	Hot injection	Repeat of TW28 for reproducibility	TEM, AFM, UV-VIS, STM	Clustered hexagonal NPLs, large size distribution
TW35	Hot injection	2h reaction time & Non-preheated injection solution	TEM	Large amorphous blobs
TW36	Hot injection	2h reaction time & Less preheated injection solution	TEM, AFM, ED, UV-VIS	Clustered hexagonal NPLs, large size distribution, good crystalline quality
TW39	Hot injection	2h reaction time & 3x upscale (for XRD)	TEM, EDX, UV-VIS	Clustered hexagonal NPLs, Bi & Se homogeneously distributed within NPLs
TW42	Hot injection	None	TEM	Small, but very clustered hexagonal NPLs
TW43	Hot injection	Quenching with EtOH instead of water bath	TEM	Low concentration, but well defined hexagonal NPLs
TW44	Hot injection	Aliquots & Quenching with EtOH	TEM, AFM, STM	Very well distributed large hexagonal NPLs, some amorphous rods observed 3-6 min
TW45	Hot injection	Aliquots & Quenching with EtOH (repeat)	TEM, AFM, ED	Well distributed smaller hexagonal NPLs, most growth observed from 1-3 minutes
TW46	Hot injection	Lower reaction temerature (165°C)	TEM	Poorly formed MPLs as well as other nanostructures
TW50	Hot injection	Acetic acid added before reaction	TEM	Amorphous structures
TW51	Hot injection	Lower reaction temerature (180°C)	TEM	Well defined large hexagonal NPLs
TW53	Hot injection	Upscale 3x with premade big batch of Bi injection solution	TEM, AFM	Large clusters of aggregated hexagonal NPLs but still many loose ones as well
TW54	Hot injection	No PVP added	TEM, AFM	Clusters of large mostly non-hexagonal NPLs

TW55	Hot injection	Big batch of Bi injection solution	TEM	Low concentration, well defined but slightly clustered hexagonal NPLs
TW55-supernatant	Washing	Washed with Acetonitrile	TEM	Higher concentration, less clustered hexagonal NPLs but more impurities present
TW56	Hot injection	None (fresh batch)	TEM, AFM, STM	Well distributed hexagonal NPLs, but large size distribution
TW57	Hot injection	Acetonitrile (ACN) as anti-solvent	TEM, AFM	Clustered hexagonal NPLs, but higher yield due to ACN
TW58	Hot injection	Olam as ligand instead of PVP	TEM, AFM	Large blobs of aggregated NPLs with large size distribution
TW59	Hot injection	None (fresh batch)	TEM, AFM	Low concentration of slightly clustered NPLs
TW59-OLAM	Washing	Ligand procedure OLAM	TEM, AFM	Clustered NPLs with some organic contamination present
TW59- less N2H4	Washing	Ligand procedure N2H4	TEM, AFM	Less clustered NPLs with some free NPLs present
TW59 – more N2H4	Washing	Ligand procedure with more N2H4	TEM	Heavily clustered with some organic contamination present
TW60-EtOH	Hot injection	ACN, fresh sample	TEM, AFM	Well distributed NPLs
TW60-Acetone	Hot injection	ACN, Acetone as solvent	TEM	Less well dispersed, slightly more clustered NPLs
TW60-EtOH -OLAM-old	Washing	Ligand procedure OLAM	TEM	Heavily contaminated NPLs
TW60-EtOH -OLAM-old -ACN	Washing	Ligand procedure OLAM	TEM	Heavily contaminated NPLs
TW60-EtOH -OLAM-new	Washing	Ligand procedure OLAM	TEM, AFM	Well distributed NPLs with some contamination
TW60-EtOH -OLAM-new -ACN	Washing	Ligand procedure OLAM + ACN	TEM, AFM, STM	Well distributed NPLs without contamination
TW60-EtOH – less N2H4	Washing	Ligand procedure N2H4	TEM, AFM, STM	Slightly clustered NPLs
TW60-EtOH more N2H4	Washing	Ligand procedure with more N2H4	TEM	Extremely clustered NPLs
TW61	Hot injection	ACN aliquots	TEM, AFM, UV-VIS	Large structures until 2 min, afterwards nicely distributed NPLs
TW62	Hot injection	ACN reproducibility	TEM, AFM, UV-VIS, FTIR	Slightly clustered NPLs
TW63	Hot injection	ACN reproducibility	TEM, AFM, UV-VIS	Slightly clustered NPLs
TW64	Hot injection	ACN reproducibility	TEM, AFM, UV-VIS, NMR	Slightly less clustered NPLs
TW65	Hot injection	ACN, aliquots, 2h reaction time	TEM, AFM	Good NPLs, not significant difference observed between aliquots
TW66	Hot injection	ACN lower T (170 °C)	TEM	Large rectangular structures (µm's)

Sample Name	Method	Varied parameters	Characterization	Results
TW67	Hot injection	ACN higher T (200 $^{\circ}$C)	TEM	Good NPLs

Table x: Bi$_2$Te$_3$ Synthesis Overview

Sample Name	Method	Varied parameters	Characterization	Results
TW33	Hot injection[4]	Hot injection instead of solvothermal	TEM	NPLs attached to Te wires
TW37	Hot injection[4]	More BiNO & NaOH	TEM, EDX	Clustered NPLs with some free ones, large size distribution
TW38	Hot injection[4]	Bi$_2$O$_3$ instead of BiNO	?	?
TW41	Hot injection[4]	More BiNO & NaOH, less reaction time	TEM	NPLs attached to Te wires
TW47	Hot injection[4]	More BiNO & NaOH, aliquots	TEM	NPLs attached to Te wires and organic contamination
TW48	Reflux[4]	2h instead of 4h	TEM	Clustered NPLs with some organic contamination
TW49	Reflux[4]	Aliquots	TEM, EDX	NPLs attached to Te wires which slowly disappear and left with clustered NPLs